Thermo magnetic effects in pyrolytic graphite
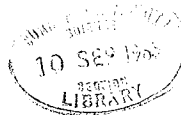
Mills, John J.

THERMOMAGNETIC EFFECTS IN PYROLYTIC GRAPHITE

by

John J. Mills

Presented in candidature for the degree of Doctor
of Philosophy of the University of Durham.

April, 1965

ACKNOWLEDGMENTS

PART II

EXPERIMENTAL

CHAPTER I

PREPARATION OF SAMPLES

CHAPTER II

APPARATUS

ABSTRACT

In this thesis some of the transport coefficients
were investigated in pyrolytic graphites of varying degrees
of perfection. The degree of perfection was assessed by
comparing the Hall Effect and magnetoresistance with single
crystal data. Of the two remaining galvanomagnetic co-
efficients the Nernst effect (the Peltier effect in a magnetic
field) was not measured and the Ettingshausen effect could
not be detected.

Of the thermomagnetic coefficients the thermal conductivity
was not measured and the Righi-Leduc effect could not be
detected. The longitudinal and transverse Nernst-Ettingshausen
effects were measured over a range of temperature and magnetic
induction.

The theory of the thermomagnetic coefficients for semi-
metals was developed and a computer used to calculate the
two latter coefficients for a range of band overlaps and
gaps and for various values of the Fermi level, and of the
ratio of the mobilities and the densities, assuming acoustic
mode lattice scattering.

The experimental results on the transverse Nernst-
Ettingshausen effect did not agree in magnitude or in its

variation with magnetic induction with the theoretical results assuming an overlap of 0.03 eV. The predicted temperature variation was found to be approximately true. An analysis of this coefficient for the case of energy independent scattering is given. This analysis gives results which agree to within 10% in magnitude with the experimental data, and in addition, gives the magnetic induction variation which was found.

The longitudinal Nernst-Ettingshausen effect was found theoretically to be very sensitive to the position of the Fermi level, the ratio of mobilities and the ratio of the densities of the carriers. The experimental results, however, exhibited an 'Umkehr' effect, indicating that the computer programme used too simple a band picture. The mean coefficient indicated that the Fermi level was near the centre of the overlap, and that the ratio of the densities of the carriers was nearly one.

An investigation of the variation of the properties of the graphite throughout the thickness of a deposit indicated that the best samples had been annealed during the growing process at just over $3000^{\circ}C$ and that there appears to be a critical temperature around $2600^{\circ}C$ for the annealing process. Since some of the properties vary by as much as an order of magnitude across the deposit, care must be taken in specifying exactly where a sample originates in the deposit.

Introduction

The purpose of this work was to measure as many
of the galvano- and thermo-magnetic coefficients as possible,
in samples of varying perfection over as wide a range of
temperature, and magnetic induction as possible, with a
view to comparison with the present theory.

In order to reduce the number of coefficients to
a more manageable number it was necessary to restrict the
direction of the magnetic induction to along the c_o axis
of the graphite lattice and to measure the coefficients at
right angles to this. This reduced the three dimensional
anisotropic phenomenological tensors to two dimensions
by restricting the motion of the carriers to the basal
planes which are isotropic. This also simplifies the theory.

The coefficients were measured in one cryostat
designed to allow all the coefficients to be measured at
temperatures ranging from $70^{\circ}K$ to $350^{\circ}K$ up to a maximum
value of magnetic induction of $1.0 \ W/m^2$. The cryostat was
designed to allow all the measurements to be made without
disturbing the sample.

Two of the galvanomagnetic coefficients were measured
to assess crystalline perfection by comparison with previous
work and to give information on the carrier densities and
mobilities. Of the two remaining coefficients the Nernst
coefficient* was not measured.

* See Table III, page 27 for definitions.

Of the thermomagnetic coefficients the thermal conductivity was not measured since it was to be measured by another member of the group.

Although all the measurements were to be made under adiabatic conditions the isothermal coefficients could be calculated from the Heurlinger relations.

To further simplify a still complex theory it was necessary to assume that the relaxation times were of the form $\tau_0 \ (E/kT)^{-1/2}$, the energy of the carriers was quadratic in k, the wave vector, and that the interaction between the carriers was negligible. These assumptions will be seen to be reasonable. Even with these simplifications a computer had to be used to calculate the coefficients over the range of magnetic induction considered. A further complication was that the thermal conductivity could not be predicted theoretically since it depended strongly on the crystalline perfection and coefficients involving this parameter could not be computed. Thus only the longitudinal and transverse Nernst-Ettingshausen coefficients could be computed.

PART I

THEORETICAL

CHAPTER I

Band Structure of Graphite

1.1.1. Short Review of the Present State of the Field

'Today, graphite is one of the best known, if not best understood, single crystals.' This comment which was made by Haering and Mrozowski (1960) in their recent review article on graphite, is used to introduce a material which is of immense technological importance. Almost every major industry uses it in some form or other. It is justifiable in view of the amount of experimental and theoretical work being published.

Most of the experimental work has been on the polycrystalline form of this material, but the following effects have all been measured in single crystals of varying purity:-

The susceptibility and the de Haas - van Alphen effect (Shoenberg 1952), the galvanomagnetic effects (Dutta 1953, Kinchin 1953, Primak and Fuchs 1954, Soule 1958 a) the de Haas Schubnikov effect (Soule 1958 b, Soule and McClure 1959), cyclotron resonance (Galt, Yager and Dail 1956), the g factor (Wagoner 1960) and the thermal conductivity (Smith and Rasor 1956). Some work on the galvanomagnetic effects in the polycrystalline form called pyrolytic graphite has been reported (Blackman, Ubbelohde and Saunders 1961, Klein

1961, 1962, 1963).

Wallace (1947) proposed the first simple model of the band structure of graphite, based on the tight binding approximation. This was used by McClure (1956, 1957) to explain the susceptibility and the de Haas - van Alphen effect, and by Lax and Zeiger (1957) to explain the cyclotron resonance, both with moderate success. Coulson (1947), Coulson and Taylor (1952), Lomer (1955) and Corbato (1956) elaborated on Wallace's model but were unable to give a clear picture of the details, which in graphite are very important. Group theory was then employed (Carter 1953, Johnston 1955, 1956) and Slonczewski 1955). Slonczewski and Weiss (1958) made the most complete study of the problem and laid the foundation for a minimum parameter model, the parameters to be determined from experiment.

Some discussion then arose as to the exact value of one of the parameters (McClure 1956, Haering and Wallace 1957, McClure 1960). In view of recent experimental results on the Schubnikov - de Haas effect (Soule, McClure and Smith 1964) it would appear that McClure's interpretation is correct (McClure 1958, 1959, 1962, 1963). The development of this model will be outlined in more detail in the following section.

1.1.2. Crystalline Structure

Since the band structure of any solid is dependent

on its crystalline structure, no attempt to discuss a band theory can do without a description of the lattice structure.

Graphite has a hexagonal crystal lattice. It was one of the first crystalline structures to be examined by x-rays (Ewald 1914, Debye and Scherrer 1917, Hull 1917, Bernal 1924, Hassel and Mark 1924, Mauguin 1926, Trezbiatowski 1936) in order of increasing precision. These all indicate that the atoms in the layers are arranged in parallel layers, in the layers forming extended hexagonal networks which may be thought of as the limit of the hydrocarbon 'ring'. The theoretical calculations assume the Bernal (1924) structure. In this the layers are arranged as in Fig. 1. i.e. in a sequence abababa, with the b layers corresponding to the a layers rotated through 180° about the c_o axis.

X-ray diffraction studies of natural graphite have indicated the existence of a rhombohedral modification with the layer sequence abcabc... in which the third layer bears the same relation to the second as the second to the first. However it has been shown that the Bernal structure is the more stable, and on heating the rhombohedral type to around $2000^{\circ}K$, it is converted into the normal hexagonal graphite.

The unit cell of the hexagonal structure is shown in Fig. 1. and contains four atoms of different types A, B, A', B'. The A type atoms have nearest neighbours on

FIGURE 1
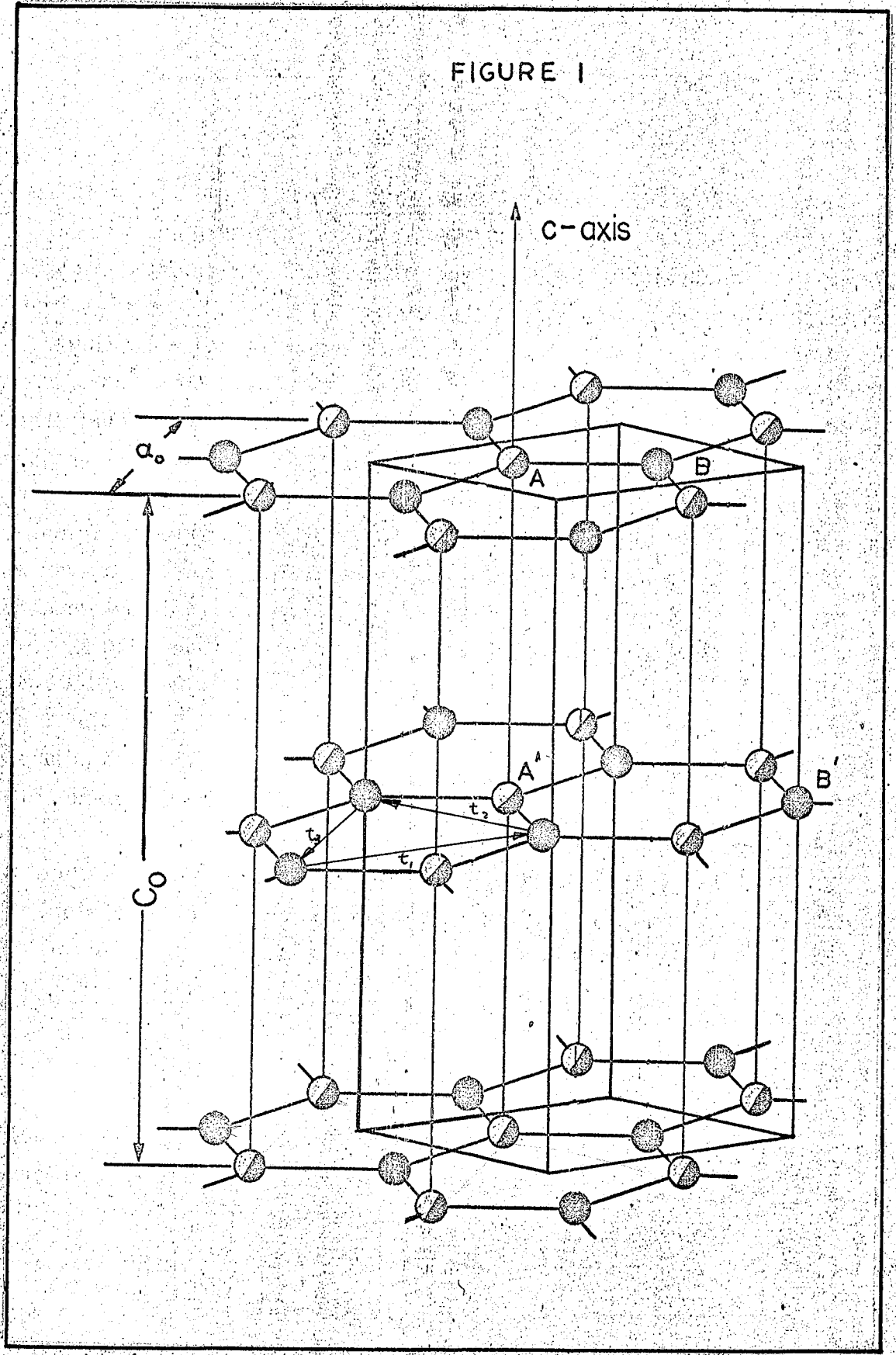
adjacent planes while the B type atoms have not.

The in plane interatomic distance is 1.42 $\overset{o}{A}$, and
the c-axis spacing of the planes is 3.37 $\overset{o}{A}$. However it is
more convenient in the following chapters to use the distances
a_o and c_o which are 2.46 A and 6.74 A respectively, as these
are used in calculating the Brillouin zones. The primitive
lattice translation vectors are t_1, t_2, t_3 and t_4, where
$t_3 = -(t_1 + t_2)$ and t_4 is parallel to the c-axis having a
magnitude of c_o (= 6.74 A).

Since the distance between the layers is large the
bonding between the layers must be weak, probably van der
Vaals type, (Nozieres 1958) and it is obvious that the best
way of approaching the problem of calculating the band
structure is to calculate the band structure of a single
layer of graphite.

1.1.3. Two-dimensional Model of Graphite

The unit cell of a single layer is shown in Fig. 2.(a)
with the Brillouin zone in Fig. 2.(b). The dotted lines in
Fig. 2.(b) shows an alternative zone used by many authors.
It is more convenient since it contains within it the points
H,H', which, as will be seen later, are important.

The carbon atom has the electronic configuration
$1s^2 2s^2 2p^2$, with the 1s electrons part of the 'ion core'.
The remaining four are the valence electrons.

FIGURE 2

a

UNIT CELL OF SINGLE LAYER

b

BRILLOUIN ZONE
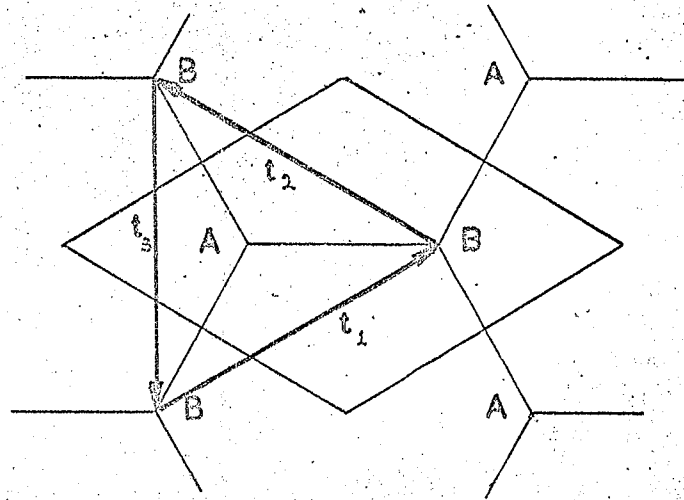
ALTERNATIVE BRILLOUIN ZONE
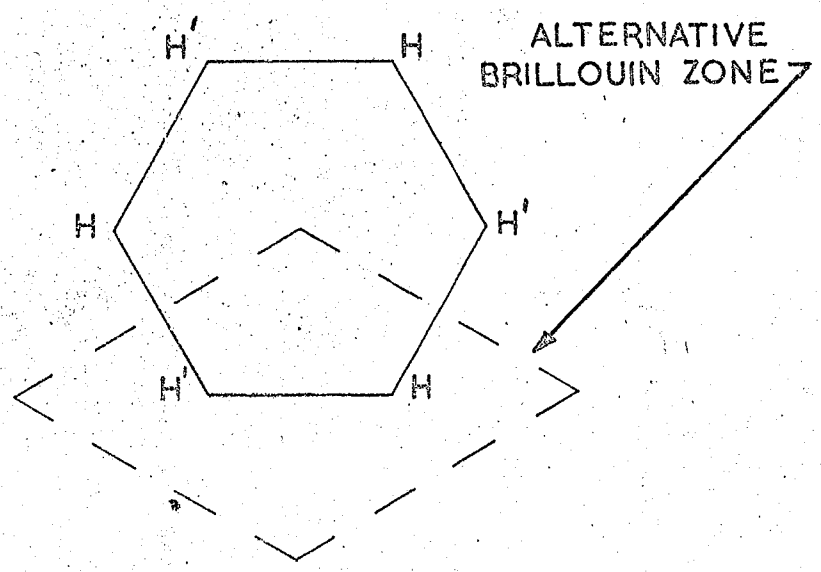
In graphite, three of these electrons form symmetrical and localised σ type bonds in the plane. Their wave functions are linear combinations of the trigonally hybridized orbitals of the isolated atom. The fourth, whose wave functions in the isolated atom is a $2p_z$ orbital, forms antisymmetrical, delocalised π type bonds at right angles to the planes. Since this classification into σ states and π states is rigorous, the problems of solving for the σ and π bands are separate.

Thus in the unit cell, with two atoms per cell and four electrons per atom, there will be six σ bands and two π bands. Only four of these bands, however, will be occupied, since each state in the bands can accommodate two electrons.

Chemical binding theory expects the order of filling of these states to be $\sigma, \sigma, \sigma, \pi, \pi^*, \sigma^*, \sigma^*, \sigma^*$. Thus if the two π bands do not overlap, the Fermi level will lie at the top of the first π band. Wallace ignored the σ bands since he assumed that the three electrons in the σ states, forming the planar bonds would not play a part in the conduction processes. Lomer (1955) and Corbato (1956) considered these bands and estimated that they lie 1 eV above and below the π bands. Taft and Apker (1955) studied the energy distribution of photoelectrons from polycrystalline graphite and found that the density of states is relatively small

at the Fermi level but increases to a much larger value several eV away. This is in agreement with the conclusions of Lomer and Corbato. Thus the σ bands can be ignored.

All the calculations on the band structure agree on the general form of the bands, that is, that the Fermi level lies near the Brillouin zone corners where the π bands are degenerate in energy. Also in this region the energy is a linear function κ, where κ is given by $k = k_H + \kappa$, where k_H is the wave vector of the zone corner.

Using the tight binding approximation, Wallace (1947) found that

$$E = \frac{1}{2S} \left[H_{11} + H_{22} \pm \left[(H_{11} - H_{22})^2 + \left| H_{12} \right|^2 \right]^{1/2} \right]$$

1.1.

which, because of the symmetry of the two dimensional lattice becomes

$$E = \frac{H_{11}}{2S} \overset{+}{\underset{-}{}} \frac{\left| H_{12} \right|}{2S}$$

1.2.

where the H_{ij} are energy integrals of the type $H_{ij} = \int \phi_i^* H \phi_j \, d\tau$ and $S = \int \phi_2^* \phi_2 \, d\tau = \int \phi_1^* \phi_1 \, d\tau$, the ϕ_i being the wave functions, H the Hamiltonian of the system, and $d\tau$ an element of volume, the integration being over the whole zone.

On carrying out the various integrations and

manipulations of the wave functions and transferring the origin to the zone corner, one finds

$$E = E_o \pm \frac{3}{2} \gamma_o \, a_o \, \kappa + \text{terms of the order of } \kappa^2$$

<div align="right">1.3.</div>

where γ_o is the overlap integral $\int X^*(\underline{r}) \, H \, X \, (\underline{r}) \, d\tau$ as defined by Wallace, $X(\underline{r})$ being the wave function for an isolated atom. I.e. to the first order in κ, energy is a linear function of κ.

By a somewhat different method Slonczewski and Weiss (hereinafter S.W.) also obtained a similar equation.

Thus the valence and conduction bands just touch at the zone corners and at $0^\circ K$ the first zone will be completely filled, and the second zone (given by the + sign in 1.1, 1.2 and 1.3) completely empty. Therefore the Fermi level lies at $E = E_o$.

Several estimates have been made of the parameter γ_o. Wallace himself does not attempt to calculate it but quotes an early value of Coulson of 0.9 eV. This appears to be rather low in the light of later work, for Coulson and Taylor (1952) estimate it at 3.0 eV, Corbato (1956) at 3.8 eV and finally S.W. calculate it to be 2.4 eV. This latter figure is in good agreement with McClure's figure of 2.6 eV deduced from experimental data (McClure 1957 and 1962).

This parameter turns out to be one of those which gives the general form of the bands in the three dimensional

case.

1.1.4. Three Dimensional Model of Graphite

In three dimensional graphite the Brillouin zone becomes a hexagonal cylinder of height $2\pi/c_o$. However S.W. have shown that it simplifies matters considerably if the centre of the zone is chosen to be at O' and thus they use the zone shown outlined by the dotted lines in Fig. 3. Since the unit cell now contains 4 atoms the secular equation becomes a 16 x 16 determinant. To simplify this Wallace assumes as in the two dimensional case, that the σ states and the π states do not mix, thus eliminating the off-diagonal terms. Johnston (1956) investigated this mixing and found that it resulted in an overlap of the π bands, but an overlap of a somewhat different nature is also obtained in the tight binding calculations if interactions between atoms more distant than nearest neighbours is taken into account (Johnston 1955).

However, as a first approximation, Wallace's treatment gives a good indication of the structure. He expanded his calculations in two dimension to include the third, and, retaining the interactions due to nearest neighbours only, obtained the equation for π energy bands:-

$$E = H_o \pm \frac{1}{2} \gamma_1 \Gamma \pm \left[\frac{1}{4} \gamma_1^2 \Gamma^2 + \gamma_o^2 \left| S \right|^2 \right]^{1/2}$$

FIGURE 3

BRILLOUIN ZONE OF GRAPHITE
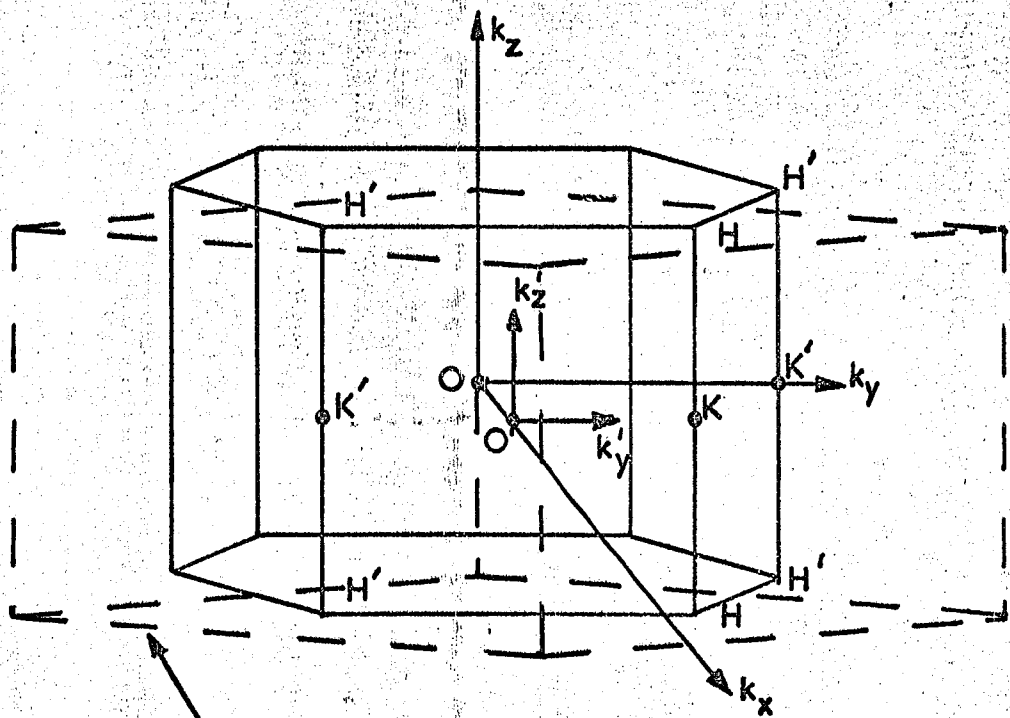
ALTERNATIVE
BRILLOUIN ZONE

where the H_o, γ_o, γ_1 are again energy integrals (sometimes called 'resonance integrals') $\sqcap = 2 \cos (k_z c_o /2)$, and $S = \sqrt{3}/2 \ \pi \ a_o \kappa a^{i\alpha}$, α being given by $\tan \alpha = k_x/k_y$.

Away from the zone corners, $|S|^2 = 3/4 \ \pi^2 a_o^2 \gamma_o^2 \kappa^2$ and the energy surfaces form hyberboloids of revolution about the E-axis in E - κ space.

At the zone corners $S = 0$ and

$$E = H_o + \gamma_1 \sqcap, \quad E_2^o = H_o - \gamma_1 \sqcap \text{ and } E_3^o, \ E_3^{o'} = H_o.$$

These are shown in Fig. 4. and the variation of E away from the corner in Fig. 5.

Thus in this approximation, the first zone is completely full at $0^o K$ and the Fermi level lies at the junction of the two degenerate bands, at H_o.

There is no variation of E_3^o with k. This results in the conduction band being degenerate everywhere along the zone edge. In addition, all four bands are degenerate at the zone corners. If E_3^o did vary with k there would be a vertical overlap of the bands, i.e. the energy of the conduction band at one particular value of k_z would be less than that of the valence band at a different value of k_z. This would also depress the Fermi level. As was shown earlier, an overlap is obtained by considering both $\sigma - \pi$ mixing and interactions from more distant neighbours. As such an overlap of the bands in this critical region could alter the

FIGURE 4
VARIATION OF ENERGY WITH k_z
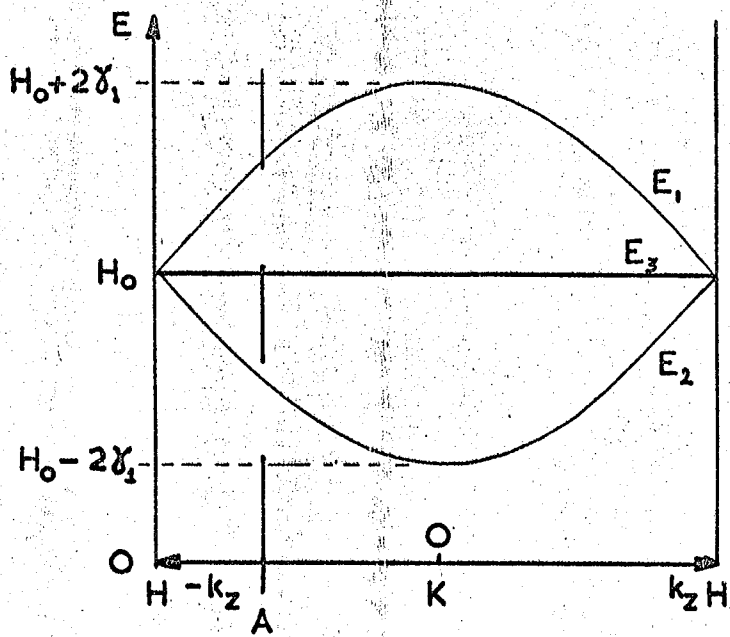
FIGURE 5
VARIATION OF ENERGY WITH K
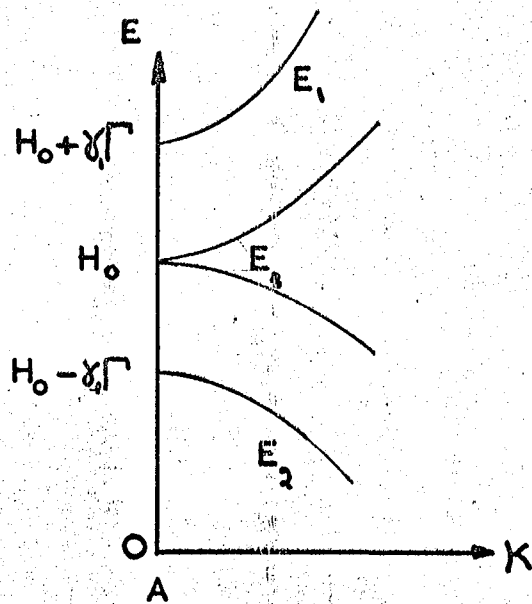
properties considerably, it was necessary to use group theory to investigate in more detail the structures in this region.

1.1.5. Band Structure of Graphite

Several authors have made group theoretical studies of the graphite lattice and band structure. Johnston (1955, 1956), Lomer (1955), Slonczewski (1955), Carter (1953) have all analysed the two and in some cases the three dimensional lattice. Slonczewski and Weiss (1958) have made the most complete study of the problem. Using Carter's analysis of the graphite lattice to obtain the wave functions at the zone corners, they obtained the energies of these states, E_i^O, $i = 1,2,3$.

Several other authors have made estimates of these functions E_i^O using the tight binding approximation (Wallace 1947, Lomer 1955, Johnston 1955, and Carter and Krumhansl 1953). They all find:-

$$E_1^O, E_2^O = \Delta \pm \gamma_1 \Gamma \qquad E_3^O = \frac{1}{2} \gamma_2 \Gamma^2$$

$$\underline{1.5.}$$

where Γ is as before and Δ, γ_1 and γ_2 are constants with dimensions of energy. Three possible forms of these equations are shown in Figs. 6 (a), (b) and (c).

Of the three variations shown in Fig. 6, two have

FIGURE 6
POSSIBLE VARIATIONS OF ENERGY WITH k_z
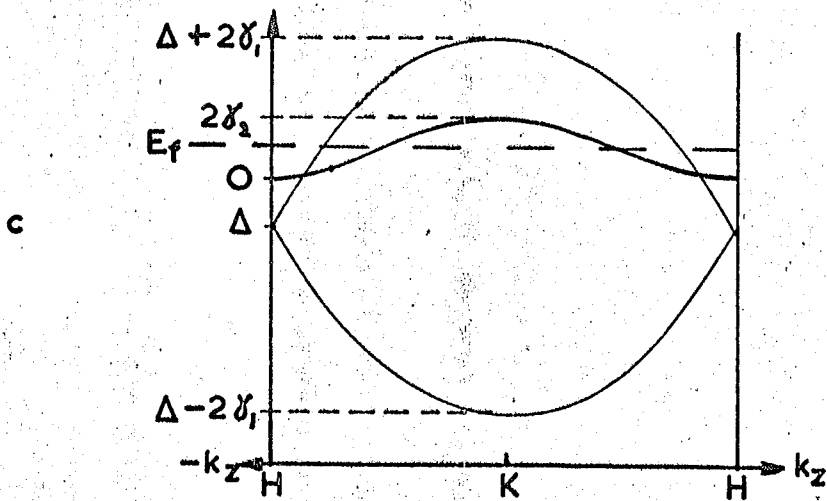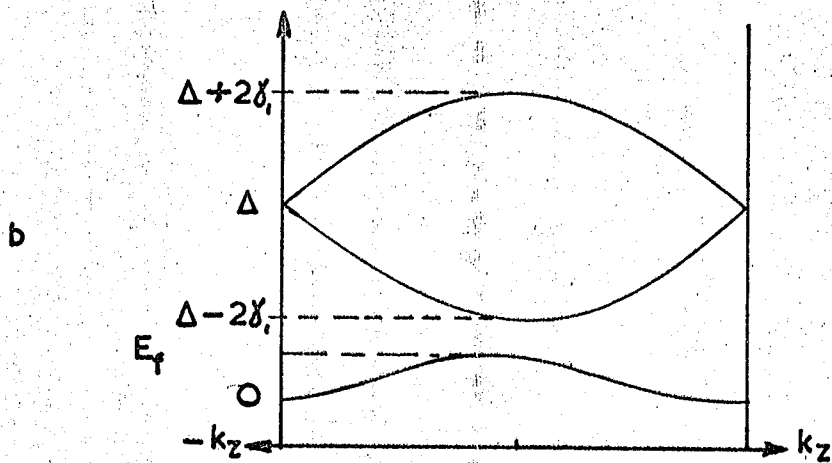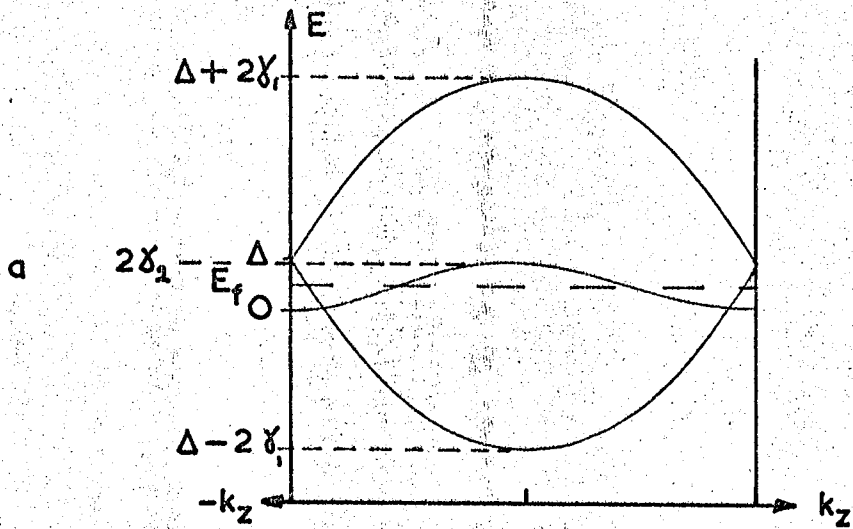
almost been eliminated by McClure (1956, 1957, 1958, 1960,
1962, 1963, 1964) in correlating the experimental work
with this model, but some authors (Haering and Wallace 1957)
claim that that shown in Fig. 6.(b) can be used to explain
several effects. It has been called the small γ_1 model
since it requires that γ_1 be of the order of 0.005 eV while
the 'overlap model' as it is called (Fig. 6.(c)), requires
γ_1 to be of the order of 0.5 eV.

Recently Soule, McClure and Smith (1964), using
the Schubnikov - de Haas effect, in a very elegant experiment,
mapped out the Fermi surfaces proving conclusively that the
model shown in Fig. 6.(c) is the most likely.

These equations, of course, give the variation of
energy along the zone edge. To find the variation of energy
with κ away from the zone edge S.W. used $\kappa.p$ perturbation
theory. In this they put $k = k_H + \kappa$ with $k_z = 0$, where k_H
is as defined in 1.1.3., and calculate $E(k_H + \kappa)$ by dia-
gonalising the perturbed Hamiltonian. Making use of a
formal similarity with the two dimensional case, they arrive
at the secular equation:-

$$
\begin{vmatrix}
E_3^O + F - E & -D(1+r) & pD & qD^* \\
-D^*(1+r^*) & \frac{1}{2}(E_1^O + E_2^O) + F - E & \frac{1}{2}(E_1^O - E_2^O) & p^*D \\
p^*D & \frac{1}{2}(E_1^O - E_2^O) & \frac{1}{2}(E_1^O + E_2^O) + F - E & -D(1+r^*) \\
qD & pD^* & -D^*(1+r) & E_3^O + F - E
\end{vmatrix} = 0
$$

1.6.

where $F = \frac{\hbar^2 k^2}{2m}$ and $D = \frac{\sqrt{3}}{2} a_o \gamma_o k\, e^{i\alpha}$ and the coefficients

p, q, r, are functions of k_z.

In terms of McClure's γ's

$$q = \gamma_3 \Gamma / \gamma_o, \quad r = \gamma_4 \Gamma / \sqrt{2}\gamma_o, \quad p = r - 1/\sqrt{2}.$$

On solving this for E, neglecting the parameters

p, q, r, and F for a first approximation, S.W. find:-

$$E_1, E_3 = \frac{1}{2}(E_1^{\,o} + E_3^{\,o}) \pm \left[\frac{1}{4}(E_1^{\,o} - E_3^{\,o})^2 + \frac{3}{4} a_o^{\,2} \gamma_o^{\,2} \kappa^2 \right]^{1/2}$$

$$E_2, E_3' = \frac{1}{2}(E_2^{\,o} + E_3^{\,o}) \pm \left[\frac{1}{4}(E_2^{\,o} - E_3^{\,o})^2 + \frac{3}{4} a_o^{\,2} \gamma_o^{\,2} \kappa^2 \right]^{1/2}$$

1.7.

These equations represent hyberboloids of revolution in κ,

E space, as shown in Fig. 7.

On including q the above equations become

$$E_1, E_3 = \frac{1}{2}(E_1^{\,o} + E_3^{\,o} + qD') \pm \left[\frac{1}{4}(E_1^{\,o} - E_3^{\,o} - qD')^2 + D'^2 \right]^{1/2}$$

$$E_2, E_3' = \frac{1}{2}(E_2^{\,o} + E_3^{\,o} - qD') \pm \left[\frac{1}{4}(E_2^{\,o} - E_3^{\,o} - qD')^2 + D'^2 \right]^{1/2}$$

1.8.

where $D' = \frac{\sqrt{3}}{2} a_o \gamma_o k_y$. The inclusion of this extra term

shows more structure, which is shown in Fig. 8a. This

'warping' of the bands has a three fold symmetry about the

E axis in E - κ space. For arbitrary k_z the warping is as

shown in Fig. 8b. (Nozieres 1958).

FIGURE 7

VARIATION OF ENERGY WITH K
ACCORDING TO FIGURE 6(C)
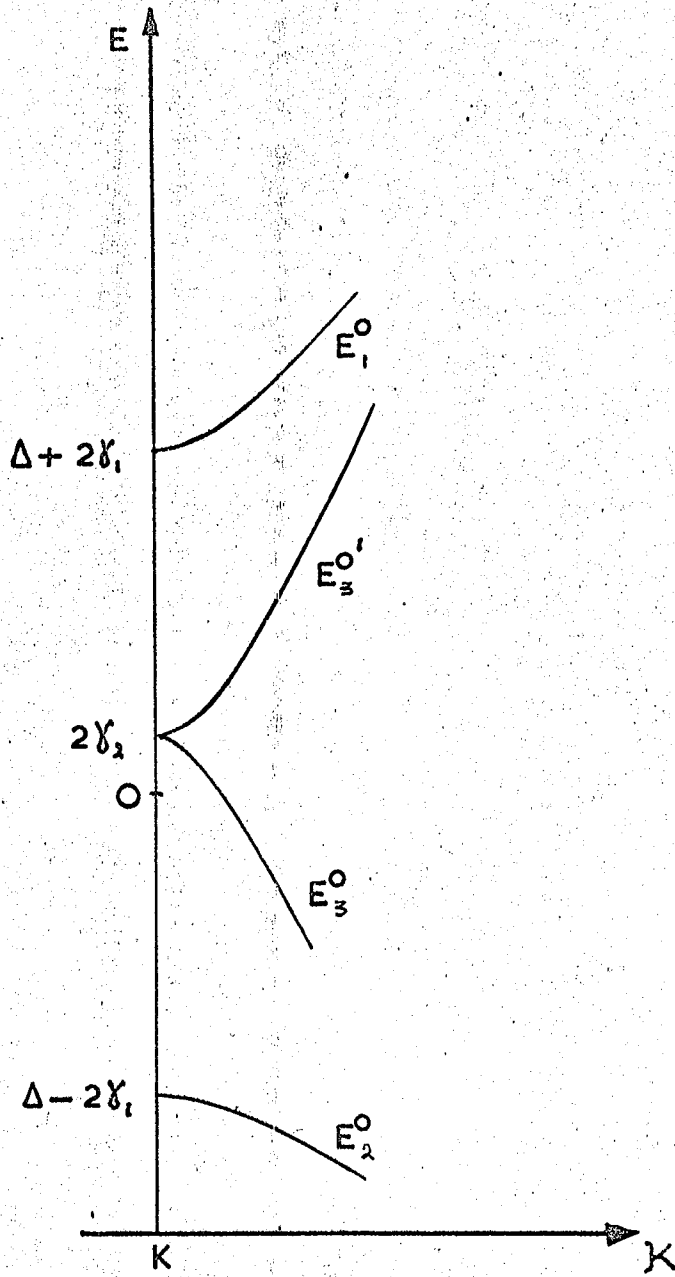
FIGURE 8
WARPING DUE TO q
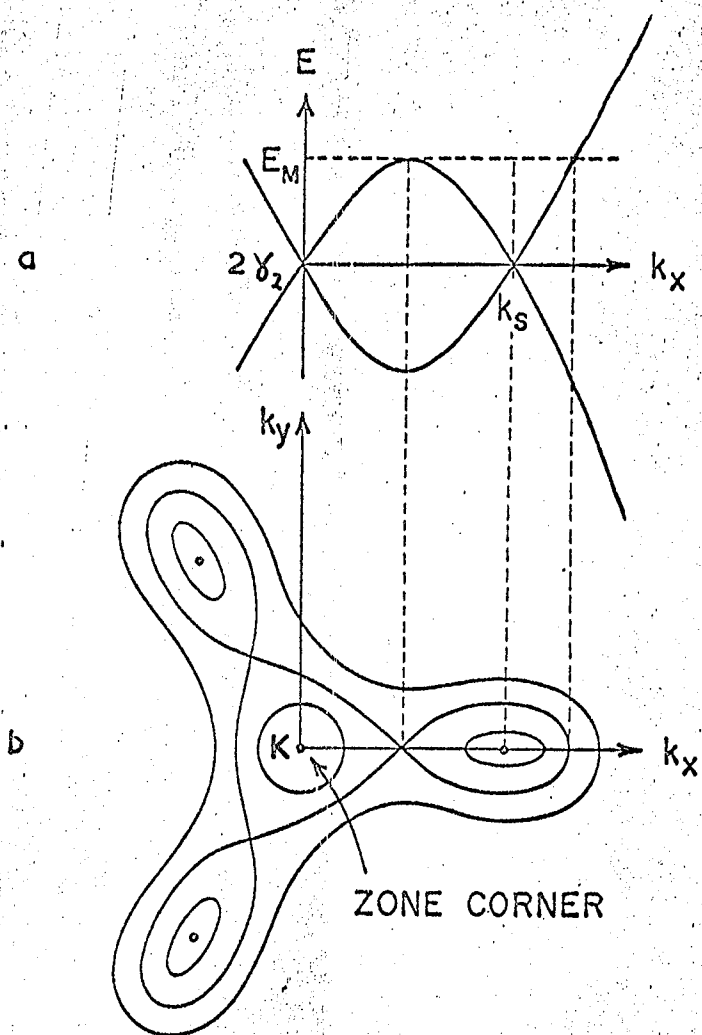
The Fermi surface, obtained by setting $E = E_f$ and rearranging the equation 1.8 is shown in Fig. 9, which is according to the overlap model (Fig. 6.(c)). As can be seen the surface consists of three ellipsoids of revolution, with 'feet' at the junctions. These feet are the result of the structure mentioned previously due to q. Soule (1958b) McClure (1958) and Nozieres (1958) have shown that these 'feet' are responsible for the minority carriers which become important at low temperatures and small magnetic fields. Here minority means a carrier with a different mass and a much smaller density.

Since the bands overlap at the zone edges, some of the electrons in the first band will overflow into the second band, leaving holes behind, thus depressing the Fermi level to the position in $E - k_z$ space, shown in Fig. 6.(c). Thus holes and electrons will be present simultaneously in accordance with the galvanomagnetic data of Soule (1958a).

It will be observed that because of the dependence of E on κ^2 the cross-section of the Fermi surface perpendicular to the c-axis will be circular (ignoring the warping). Thus as long as the motion of the carriers is confined to this plane it can be said that graphite has an effective two dimensional isotropy.

FIGURE 9

THE FERMI SURFACE OF GRAPHITE
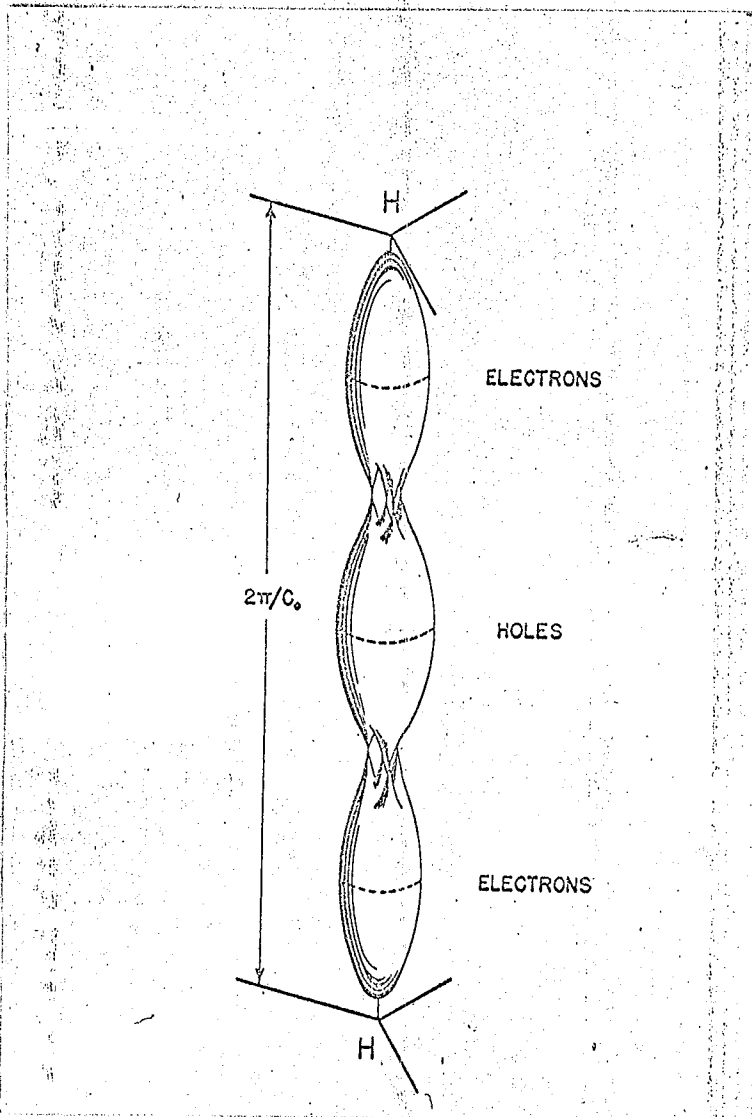
1.1.6. <u>Parabolic Dependence of Energy on Wave Vector</u>

In the next chapter, in order to solve the Boltzmann equation, it is necessary to assume that $E \propto k^2$, where E is the energy and k the wave vector. In this section this approximation is examined and it is shown that it holds for wave vectors around the Fermi surface. Klein (1964) also uses this approximation to explain the galvanomagnetic effects in pyrolytic graphite.

From section 1.1.5., (equation 1.7) neglecting the higher order terms,

$$E_3, E_1 = \frac{1}{2}(E_1^{\,o}+E_3^{\,o}) \pm \left[\frac{1}{4}(E_1^{\,o}-E_3^{\,o})^2 + \frac{3}{4}\gamma_o^{\,2}a_o^{\,2}\kappa^2\right]^{1/2}$$

$$E_3, E_2 = \frac{1}{2}(E_2^{\,o}+E_3^{\,o}) \pm \left[\frac{1}{4}(E_2^{\,o}-E_3^{\,o}) + \frac{3}{4}\gamma_o^{\,2}a_o^{\,2}\kappa^2\right]^{1/2}$$

<div align="right">1.7.</div>

Assuming that $\frac{3}{4}\gamma_o^{\,2}a_o^{\,2}\kappa^2 \lll \frac{1}{4}(E_1^{\,o}-E_3^{\,o})^2$ the terms in the square bracket can be expanded to give

$$E_1 = E_1^{\,o}+ \frac{3}{4}\gamma_o^{\,2}a_o^{\,2}\kappa^2(E_1^{\,o}-E_3^{\,o})^{-1}; \quad E_2 = E_2^{\,o}+ \frac{3}{4}\gamma_o^{\,2}a_o^{\,2}\kappa^2(E_2^{\,o}-E_3^{\,o})^{-1}$$

$$E_3 = E_3^{\,o}+ \frac{3}{4}\gamma_o^{\,2}a_o^{\,2}\kappa^2(E_1^{\,o}-E_3^{\,o})^{-1}; \quad E_3' = E_3^{\,o}+ \frac{3}{4}\gamma_o^{\,2}a_o^{\,2}\kappa^2(E_2^{\,o}-E_3^{\,o})^{-1}$$

<div align="right">1.9.</div>

Now the values of k which are predominant for most transport processes are those which lie within kT of the Fermi surface, which is obtained by setting $E = E_f$ in the

equation 1.7. obtaining

$$(E_f - E_1{}^O) \; (E_f - E_3{}^O) \; = \; \frac{3}{4} \gamma_o{}^2 a_o{}^2 \kappa^2, \quad i = 1, 2.$$

<div align="right">1.10</div>

However the functions $E_i{}^O$ are dependent on k_z since

$$E_1{}^O = \triangle + \gamma_1 \Gamma, \quad E_2{}^O = \triangle - \gamma_1 \Gamma, \quad E_3 = E_3{}' = \frac{1}{2} \gamma_2 \Gamma^2$$

and k_z is restricted to the range $\mp \pi/c_o$ making Γ lie within the range $0 - 2$. Thus if the assumption holds for the two extreme values of Γ it will be assumed that it holds at intermediate values. Since E_2^O lies deep below the other bands (Fig. 6.(c)) it will not be used in the conduction processes.

The most recent values of the band parameters are

$\gamma_o = 2.6$ eV, $\gamma_1 = 0.3$ eV, $\gamma_2 = 0.017$, $\triangle = - 0.12$ eV

$E_f = 0.02$ eV (McClure and Smith 1963, Soule, McClure and Smith 1964) and $kT = 0.025$ eV for $T = 300^O K$. Thus if

$$\left| (E_f - E_1{}^O) \; (E_f - E_3{}^O) \right| < \frac{1}{4}(E_1{}^O - E_3{}^O)^2$$

then the expansion will be valid.

For wave vectors on the Fermi surface:-

$\Gamma = 2$ $E_1{}^O = 0.48$ eV $E_3{}^O = 0.034$ eV

$\left| (E_f - E_1{}^O)(E_f - E_3{}^O) \right| = \left| (-0.46)(-0.014) \right| = 0.006 (eV)^2$

$\frac{1}{4}(E_1{}^O - E_3{}^O)^2 = \frac{1}{4}(0.444)^2 = 0.05 (eV)^2$

$\Gamma = 0$ $E_{1,2}^O = - 0.12$ eV $E_3{}^O = 0.0$ eV

$\left| (E_f - E_{1,2}^O)(E_f - E_3{}^O) \right| = \left| (-0.1)(0.02) \right| = 0.002 (eV)^2$

$\frac{1}{4}(E_{1,2}^O - E_3{}^O)^2 = \frac{1}{4}(-0.12)^2 = 0.0036 (eV)^2$

For wave vectors defined by $E_f + kT$:-

$\Gamma = 2$ $E_1^o = 0.48$ eV $E_3^o = 0.034$ eV

$\left| (E_f + kT - E_1^o)(E_f + kT - E_3^o) \right| = \left| (-0.435)(0.011) \right| = 0.00475 (eV)^2$

$\frac{1}{4}(E_1^o - E_3^o)^2 \qquad = \frac{1}{4}(0.44)^2 \qquad = 0.05 (eV)^2$

$\Gamma = 0$ $E_{1,2}^o = -0.12$ eV $E_3^o = 0.0$ eV

$\left| (E_f + kT - E_{1,2})(E_f + kT - E_3^o) \right| = \left| (0.165)(0.045) \right| = 0.0075 (eV)^2$

$\frac{1}{4}(E_{1,2}^o - E_3^o)^2 \qquad = \frac{1}{4}(-0.12)^2 \qquad = 0.0036 (eV)^2$

Thus, although the assumption holds good for carriers on the Fermi surface, the expansion is not strictly valid for carriers with wave vectors defined by $E_f + kT$ at the zone corners. However, since the number of carriers in this region is small compared to that in the rest of the bands, the departure from the parabolic dependence can be ignored.

CHAPTER II

General Theory of Transport Processes

1.2.1. Introduction

Transport processes are those processes by which electronic charge or thermal energy is carried in materials, usually crystalline solids, but the expression can also be used for similar processes in liquids and gases. In this thesis it will always refer to solids.

The theory of these processes has been treated by many authors (Wilson 1936, 1953, Kohler 1941, Smith 1961, Putley 1960, Tsidil'kovski 1963), and there exist several different notations. In the one used here the gradient of the electrochemical potential and the heat current density, which will be defined later, are used.

1.2.2. General Theory for One Carrier

The fundamental equation of the theory is Boltzmann's. This can be derived from Liouville's theorem which states that the distribution function of particles in an isolated system is constant for motion along a phase trajectory, i.e.

$$\frac{df}{dt} = \left(\frac{df}{dt}\right) + \left(\frac{df}{dt}\right)_{coll} + \left(\frac{df}{dt}\right)_{ext} = 0^* \qquad 2.1.$$

where $f(\underline{v},\underline{r})$ is the particle distribution function.

The two terms $\left(\frac{df}{dt}\right)_{ext}$ and $\left(\frac{df}{dt}\right)_{coll}$ represent the effect of applied external forces and internal restoring forces. The latter are due to the vibrations of the lattice and impurities in the lattice, which tend to restore the perturbed distribution function to its equilibrium value. The former are due to the applied electrical or magnetic fields. Since only steady state processes are considered the carriers are assumed to be in equilibrium and therefore $\left(\frac{df}{dt}\right) = 0$. Thus the effects of the internal and external forces must cancel out. Expanding $\left(\frac{df}{dt}\right)_{ext}$ in terms of $\underline{k}$ and $\underline{r}$ and using the general relation $\hbar.d\underline{k}/dt = \underline{F}$ (Wilson 1953, Smith 1961) where $\underline{F}$ is the applied force, $\underline{k}$ is the wave vector, $\underline{r}$ the position vector and $\hbar = h/2\pi$, h being Planck's constant, it can be shown that

$$\nabla_{\underline{r}} \, f.\underline{v} + \frac{1}{h} \nabla_{\underline{k}} \, f.\underline{F} = - \left(\frac{df}{dt}\right)_{coll} \qquad 2.2.$$

where $\underline{v}$ is the velocity of the carrier with energy E.

The force $\underline{F}$ represents the action of the electrical and magnetic fields and is given by the Lorentz force

* Footnote. Since typing only gives $\frac{df}{dt}$ not $\frac{\partial f}{\partial t}$, it will be assumed that $\frac{df}{dt}$ represents the partial differential.

$\pm$ e($\cancel{H}$ + $\underline{v} \times \underline{B}$), the negative referring to the carriers of one sign and the positive to the carriers of the other sign. (See Wilson 1953, Ziman 1960 for a full treatment).

To calculate $(\frac{df}{dt})_{coll}$ from first principles is a task which is extremely difficult if not impossible. It can be shown (Wilson 1953) that, if it is assumed that the perturbation of the distribution function by the external fields is small, and also that the return to equilibrium when the external forces are removed is a relaxation process, then this term can be replaced by

$$\frac{f - f_o}{\tau} = - \frac{\underline{v} \cdot \underline{c}(E)}{\tau} \frac{df}{dE}$$

2.3.

where τ is the relaxation time associated with the return to equilibrium and $\underline{c}(E)$ is a function which is to be determined.

Thus the Boltzmann equation becomes

$$- e(\underline{X} + \underline{v} \times \underline{B}) \cdot \nabla_k f + \hbar \underline{v} \cdot \nabla f = - \frac{\underline{v} \cdot \underline{c}}{\tau} \frac{df}{dE} \hbar$$

2.4.

Making use of the relations

$$\nabla f = kT \frac{df_o}{dE} \nabla (\frac{E - E_f}{kT}), \qquad \underline{X} \cdot \nabla_k f = \underline{X} \cdot \nabla_k f_o = \underline{X} \cdot \underline{v} \, \hbar \frac{df_o}{dE}$$

$$(\underline{v} \times \underline{B}) \cdot \nabla_k f = \underline{v} \cdot (\underline{B} \times M^{-1} \underline{c}) \, \hbar \frac{df_o}{dE}$$

where M^{-1} is the reciprocal effective mass tensor, this

becomes

$$-\hbar e\ \underline{X}.\underline{v}\ \frac{df_o}{dE} + \hbar e\underline{v}.(B\ x\ M^{-1}\underline{c})\frac{df_o}{dE} + \hbar kT\underline{v}.\nabla(\frac{E-E_f}{kT})\frac{df_o}{dE} = -\ \frac{\underline{v}.\underline{c}}{\tau}\ \frac{df_o}{dE}\hbar$$

<div align="right">2.5.</div>

i.e. $\hbar\underline{c} - e\tau\hbar\ (B\ x\ M^{-1}\underline{c}) = e\tau\hbar\underline{X}^{+}$

<div align="right">2.6.</div>

where $\quad \underline{X}^{+} = \underline{X} - \frac{kT}{e}\nabla(\frac{E-E_f}{kT})\quad.$

An explicit expression for $\underline{c}$ is obtained by taking scalar and vector products with $\underline{B}$ (Wilson 1953, Ziman 1960)

$$\underline{c} = -\ \frac{e\tau\ \underline{X}^{+} + \tau\ \underline{B}\ x\ (M^{-1}\underline{X}^{+}) + e\ \tau^{2}\left|M^{-1}\right|\ (\underline{X}^{+}.\underline{B})M^{-1}\underline{B}}{1 + (e\tau)^{2}\left|M^{-1}\right|\ (M\underline{B}.\underline{B})}$$

<div align="right">2.7.</div>

If $e^{2}\left|M^{-1}\right|\ (M\underline{B}.\underline{B})\sim\frac{kT}{\hbar}$, then the theory behind the Boltzmann equation is no longer valid. It is assumed that the value of B required for this region is so large that it need not be considered.

The expression (2.3) is now substituted in the equations for the transport of electrical charge and energy:-

$$\underline{j} = -\ e\int\underline{v}fdn \qquad \underline{w}^{e} = \int E\underline{v}fdn \qquad 2.8.$$

where f is the perturbed distribution function and dn the number of carriers in the interval E to E + dE.

After suitable rearrangements these give the phenomenological equations

$$\underline{j} = (S^1)\underline{X}^+ - \frac{1}{T}(S^2)\,\nabla\,T \qquad w^e = (S^3)\underline{X}^+ - \frac{1}{T}(S^4)\,\nabla\,T$$

$$2.9.$$

where the (S^i) are three dimensional tensors with elements which can only be derived easily for the case of spherically symmetric energy surfaces.

In this case M^{-1} becomes $(1/m^*)$ (1) where (1) is the unit matrix, m^* the effective mass, and $E = \frac{(\hbar k)^2}{2m^*}$. If the energy surfaces are not spherical, but ellipsoidal, they can be transferred into spheres by a transformation of type $\frac{k_i}{\sqrt{m_i^*}}$ (Blatt 1957) where the k_i and m_i^* are the wave vector and effective mass in the direction of the ith axis of the ellipsoid.

Thus the tensors above become two dimensional with elements given in Table I

TABLE I

$$S^1{}_{11} = S^1{}_{22} = e^2 I_{10} \qquad\qquad S^1{}_{12} = -S^1{}_{21} = e^2 I_{20}$$

$$S^2{}_{11} = S^2{}_{22} = e I_{11} = S^3{}_{11} = S^3{}_{22} \qquad S^2{}_{12} = -S^2{}_{21} = e I_{21} = S^3{}_{12} = -S^3{}_{21}$$

$$S^4{}_{11} = S^4{}_{22} = I_{12} \qquad\qquad S^4{}_{12} = S^4{}_{21} = I_{22}$$

where $I_{ij} = \frac{1}{3\pi^2}(eB)^{i-1}\int k^3 (\frac{\tau}{m})^i E^j (1 + \omega^2\tau^2)^{-1}\frac{df_0}{dk}\,dk$ 2.10

k being the magnitude of the wave vector and $\omega = eB/m^*$.

However, Mazur and Prigogine (1951) have shown that it is best to transform these equations partially to give the j_i as dependent variables. Thus

$$\underline{X}^{\bullet} = \rho(B)\,\underline{j} - \alpha(B)\,\nabla T$$

$$\underline{W}_e^{\bullet} = \pi(B)\,\underline{j} - K(B)\,\nabla T \qquad \underline{2.11.}$$

where $\underline{X}^{\bullet} = \underline{X} - \frac{1}{e}\nabla E_f$ and $\underline{W}_e^{\bullet} = \underline{w}_e - \frac{E_f}{e}\,\underline{j}$. This version of the phenomenological equations was first suggested by Meixner (1941). The elements of the above tensors are given in Table 11.

TABLE II

$$\rho_{11} = \rho_{22} = \frac{1}{e^2}\frac{I_{10}}{(I_{10}^2 + I_{20}^2)} \qquad\qquad \rho_{12} = -\rho_{21} = \frac{1}{e^2}\frac{I_{20}}{(I_{10}^2 + I_{20}^2)}$$

$$\alpha_{11} = \alpha_{22} = \frac{1}{Te}\frac{(I_{10}I_{11} + I_{20}I_{21})}{(I_{10}^2 + I_{20}^2)} - E_f \qquad \alpha_{12} = -\alpha_{21} = \frac{1}{Te}\frac{(I_{10}I_{21} - I_{20}I_{11})}{(I_{10}^2 + I_{20}^2)}$$

$$\pi_{ij}(B) = T\,\alpha_{ji}(-B)$$

$$K_{11} = K_{22} = \frac{1}{T}\left\{ I_{12} + \frac{(I_{21}^2 I_{10} - 2I_{11}I_{20}I_{21} - I_{11}^2 I_{10})}{I_{10}^2 + I_{20}^2} \right\} - K_L$$

$$K_{12} = -K_{21} = \frac{1}{T}\left\{ I_{22} - \frac{(I_{21}^2 I_{20} + 2I_{10}I_{11}I_{21} - I_{11}^2 I_{20})}{I_{10}^2 + I_{20}^2} \right\}$$

K_L = lattice thermal conductivity.

1.2.3. Theory for More than One Carrier

In the preceding theory it has been assumed that there has been only one carrier. However many materials including

graphite have more than one type of carrier, each with a different effective mass and relaxation time.

In order to derive the coefficients for all the carriers, it is necessary to add together the contributions from each band:-

$$j_i = \sum_{m=1}^{N} j_i^m \qquad\qquad \underline{2.12.}$$

$$W_i = \sum_{m=1}^{N} W_i^m \qquad\qquad \underline{2.13.}$$

changing e to $|e|$ in 2.4 and 2.8 so that difference in sign between holes and electrons is taken into account, the subscript being a direction index. It is also necessary to remember that $E_f^1 = E_f^2 = E_f^3 = \dots E_f$, the Fermi level of the whole system, and that the position of the energy zero is the same for each carrier.

Thus, when this is done for two carriers of opposite sign it turns out that it is equivalent to adding the various I_{ij} due to the holes and electrons according to:-

$$I_{10} = I_{102} + I_{101} \qquad\qquad I_{11} = I_{112} - I_{111} + E_G I_{102}$$

$$I_{20} = I_{202} - I_{201} \qquad\qquad I_{21} = I_{212} + I_{211} + E_G I_{202}$$

$$I_{12} = I_{122} + I_{121} + 2E_G I_{112} + (E_G)^2 I_{102} \qquad \underline{2.14.}$$

where the third suffix m = 1,2 indicates the contribution

from electrons and holes respectively, and E_G is the energy

gap. The contribution to the thermal conductivity coefficient

from the lattice is not taken account of here, since the

effects to be calculated do not use this coefficient.

In the following chapters unless stated otherwise,

the coefficients I_{ij} will stand for the total coefficients

and the I_{ijm} for the coefficients of each carrier.

1.2.4. Definitions and Auxiliary Conditions

Having derived the phenomenological equations 2.11.

it is now necessary to introduce the appropriate conditions

and definitions for the galvanomagnetic and thermomagnetic

effects. The classification used here is due to Jan (1957).

In the following we consider a set of mutually perpendi-

cular axes Ox_1, x_2, x_3. The magnetic field is directed along

the x_3 axis and the primary current flow (electrical or

thermal) is directed along the x_1 axis. In graphite let

Ox_3 be along the c_o-axis. Since the two directions in the

planes are equivalent, there is an effective isotropy in the

Ox_1-x_2 plane.

The effects can be divided into two main groups:-

galvanomagnetic and thermomagnetic. They are defined by the

primary current flows. Those with an electrical current are

termed galvanomagnetic and those with a temperature gradient

(i.e. a thermal energy flow) thermomagnetic.

These two main groups can be further subdivided into

two sections according to the direction in which the effect
is measured.   These are:-

(1)   Transverse effects in a transverse magnetic induction.

In these, the primary flow, the measured effect

and the magnetic field are all mutually perpendicular.

(2)   Longitudinal effects in a transverse magnetic induction.

In these the measured effect is in the same direction

as the primary flow, both being perpendicular to

the magnetic field.

A third group in which the magnetic field is in the
same direction as both the primary flow and the measured
effect also exists but will be neglected here.   These are
given by the term $\underline{B}(\underline{B}.\underline{X})$ in the equation 2.7.

Some authors use a different classification of the
effects, (Putley 1960, Tsidilkovski 1963).   In this the two
main groups are called isothermal and adiabatic according to
the conditions prevailing mutually perpendicular to the primary
flow and the magnetic field.   If there is a temperature
gradient in this direction, it is an adiabatic effect, while
if there is no gradient it is an isothermal effect.

In the classification used here, unless the effect
requires a temperature gradient in that direction the effect
is split into two by the auxiliary conditions.   For an iso-
thermal effect, $dT/dx_2 = 0$, while for an adiabatic effect
$W_2' = 0$.

The definitions of the effects are shown in the fourth column of Table III, along with the letter most commonly used as a symbol. The third column gives the auxiliary conditions which are substituted in the equations 2.11 to give the expressions for the various coefficients in column 5.

It is obvious from these expressions that several of the effects are related.

1.2.5. Relations between Coefficients

The relations between isothermal and adiabatic coefficients were first discussed by Heurlinger (1915, 1916) and are also given by Jan (1957), Putley (1960) and Harman and Honig (IV and V, 1963). They are:-

$$
\begin{aligned}
R_{ij}^{a} &= R_{ij}^{i} + \alpha_{jj}^{i} P_{ji} & Q_{ij}^{a} &= Q_{ij}^{i} + \alpha_{jj}^{i} S_{ji} \\
\rho_{ii}^{a} &= \rho_{ii}^{i} - Q_{ij}^{i} P_{ji} B_{k}^{2} & \alpha_{ii}^{a} &= \alpha_{ii}^{i} - Q_{ij} S_{ji} B_{k}^{2} \\
K_{ii}^{a} &= K_{ii}^{i}(1 + S_{ji}^{2} B_{k}^{2}) & \pi_{ii}^{a} &= (\pi_{ii}^{i} - P_{ij} S_{ji} B_{k}^{2}) \frac{K_{ii}^{i}}{K_{ii}^{a}}
\end{aligned}
\qquad \underline{2.15.}
$$

where the coefficients R, α, P etc. have the meanings given in Table III and the superscripts a, i, refer to the conditions in the Ox_2 direction while the subscripts, i, j, k, are the direction indices of the system.

Several other relations exist, especially in anisotropic solids (Harman, Honig and Tarmy 1963), but the two of the

TABLE III

Galvanomagnetic Effects

Transverse Effects in a Transverse Induction

Hall

isothermal: $dT/dx_2 = 0$, $j_2 = dT/dx_1 = 0$

adiabatic: $w_2 = 0$

$$\frac{X_2}{j_1} = \begin{cases} R^i_{12}B = -\rho_{12} \\ R^a_{12}B = -\rho_{12} \div \alpha_{11}\dfrac{\pi_{12}}{K_{11}} \end{cases}$$

Ettingshausen

$w_2 = j_2 = dT/dx_1 = 0$

$$-\frac{dT/dx_2}{j_1} = P_{12}B = -\frac{\pi_{12}}{K_{11}}$$

Longitudinal Effects in a Transverse Induction

Electrical Resistivity

isothermal: $dT/dx_2 = 0$, $j_2 = dT/dx_1 = 0$

adiabatic: $w_2 = 0$

$$\frac{X_2}{j_1} = \begin{cases} \rho^i_{11} = \rho_{11} \\ \rho^a_{11} = \rho_{11} - \alpha_{12}\dfrac{\pi_{12}}{K_{11}} \end{cases}$$

Nernst

isothermal: $dT/dx_2 = 0$, $j_2 = w_1 = 0$

adiabatic: $w_2 = 0$

$$-\frac{dT/dx_1}{j_1} = \begin{cases} \pi^i_{11} = \dfrac{\pi^i_{11}}{K_{11}} \\ \pi^a_{11} = \dfrac{1}{K^a_{11}}\left(\pi_{11} + \dfrac{\pi_{12}K_{12}}{K_{11}}\right) \end{cases}$$

TABLE III (continued)

Thermomagnetic Effects

e Effects in a Transverse Induction

$$j_1 = j_2 = w_2 = 0 \qquad \frac{dT/dx_2}{dT/dx_1} = S_{12}B = \frac{K_{12}}{K_{11}}$$

Nernst Ettingshausen adiabatic $w_2 = 0$

$$j_1 = j_2 = 0 \qquad = \frac{X_2}{j_1} = \left\{ \begin{array}{l} Q_{12}^i B = -\alpha_{12} \\[4pt] Q_{12}^a B = -\alpha_{12} + \alpha_{11}\dfrac{K_{12}}{K_{11}} \end{array} \right.$$

Longitudinal Effects in a Transverse Induction

Thermal Conductivity isothermal $dT/dx_2 = 0$ adiabatic $w_2 = 0$

$$j_1 = j_2 = 0 \qquad -\frac{w_1}{dT/dx_1} = \left\{ \begin{array}{l} K_{11}^i = K_{11} \\[4pt] K_{11}^a = K_{11}\left(1 + \dfrac{K_{12}^2}{K_{11}^2}\right) \end{array} \right.$$

Longitudinal Nernst Ettings-hausen (thermo-electric power or Seebeck) isothermal $dT/dx_2 = 0$ adiabatic $w_2 = 0$

$$j_1 = j_2 = 0 \qquad -\frac{X_1}{dT/dx_1} = \left\{ \begin{array}{l} \alpha_{11}^i = \alpha_{11} \\[4pt] \alpha_{11}^a = \alpha_{11} + \alpha_{12}\dfrac{K_{12}}{K_{11}} \end{array} \right.$$

most interest in isotropic materials are Kelvin's (which

has been used in Table II) and Bridgman's (1924):-

$$\pi_{ii}(B) = T\alpha_{ii}(-B) \qquad\qquad Q_{ij}^{t}(B)T = K_{jj}(B)P_{ji}(B)$$

The first is useful for calculating the Nernst effect ($\pi_{ii}(B)$)

from the longitudinal Nernst-Ettingshausen coefficient, while

the second is useful for predicting the Ettingshausen from

the transverse Nernst-Ettingshausen coefficient.

In this work attempts will be made to measure all

of the effects mentioned in Table II except the following:-

The Nernst or the change in the Peltier coefficient

in a magnetic induction.

The change in the thermal conductivity in a magnetic

induction or the Maggi-Righi-Leduc effect.

Only the adiabatic coefficients will be measured, the

isothermal coefficients being derived from equations 2.15.

ERRATA

In Chapters III and IV
the superscripts i and a are
dropped for convenience. The
expressions derived are the
isothermal coefficients.

1.3.1.   Introduction

The theory of galvanomagnetic effects in graphite

has been examined by McClure (1958) in analysing the data of

Soule (1958a) and, in a simplified version by Soule himself

(1958a).

McClure used the full theory as developed in the

last chapter giving expressions for the integrals I_{ijm} by

expanding the integrand about the Fermi level. This is

permissible since the differential of the distribution

function in the degenerate range is a peaked function. He

then used a computer to fit the terms from each carrier by

the method of least squares, the electronic parameters being

given by the constants used in the fitting process. This

method is practicable only when the data includes measure-

ments out to large values of the magnetic induction. Soule

measured the Hall and magnetoresistance effects out to 2.5

W/m^2.

However, Soule analysed his own data using the low

magnetic induction approximation and his results agree fairly

well with McClure's. This led Klein (1961) and other workers

to use his method in analysing data on pyrolytic graphite,

to give the mobilities and densities of the carriers. In

this thesis Soule's method is employed but it is not clear if the values obtained by this method are correct as they differ from McClure's values by as much as 40%.

1.3.2. Hall and Magnetoresistance Effects

Using Tables II and III and equations 2.10 and 2.14 it can be shown that:-

$$I_{10} = \frac{1}{3\pi^2} \left[\int_o^\infty (1+\omega_2^2\tau_2^2)^{-1} k^3 \left(\frac{\tau_2}{m_2}\right) \frac{df_o}{dk} dk + \int_o^\infty (1+\omega_1^2\tau_1^2)^{-1} k^3 \left(\frac{\tau_1}{m_1}\right) \frac{df_o}{dk} dk \right] \quad \underline{3.1.}$$

$$I_{20} = \frac{1}{3\pi^2} \left[\int_o^\infty (1+\omega_2^2\tau_2^2)^{-1} k^3 \left(\frac{e\tau_2 B}{m_2}\right) \frac{df_o}{dk} dk - \int_o^\infty (1+\omega_1^2\tau_1^2)^{-1} k^3 \left(\frac{e\tau_1 B}{m_1}\right) \frac{df_o}{dk} dk \right] \quad \underline{3.2.}$$

where $\omega_i = eB/m_i$. [+]

Since it was shown that the Fermi level lies near the edges of two degenerate bands (Chapter I), it can be assumed that df_o/dk is a delta function and that the integral can be replaced by the value of the integrand at the peak (Wilson 1953, McClure 1958) i.e. at E_f. To eliminate $k^3(E_f)$ it is best to divide by $n = \frac{1}{3\pi^2} \int_o^\infty k^3 \frac{df_o}{dk} dk$ and multiply by n.

Thus $I_{10} = \frac{1}{e}(n_2\mu_2(1+\mu_2^2B^2)^{-1} + n_1\mu_1(1+\mu_1^2B^2)^{-1})$ $\qquad$ $\underline{3.3.}$

$\qquad I_{20} = (n_2\mu_2^2(1+\mu_2^2B^2)^{-1} - n_1\mu_1^2(1+\mu_1^2B^2)^{-1})B$ $\qquad$ $\underline{3.4.}$

where $\mu_i = \dfrac{e\tau_i(E_f)}{m_i}$, the zero magnetic induction mobility.

[+] Note that the * has been dropped from the m^* for convenience.

After substitution and manipulation of the terms

$$\rho = \frac{\mu_1 n_1(1 + \mu_2^2 B^2) + \mu_2 n_2(1 + \mu_1^2 B^2)}{e\left\{(\mu_1 n_1 + \mu_2 n_2)^2 + \mu_1^2 \mu_2^2 B^2(n_2 - n_1)^2\right\}} \qquad \underline{3.5.}$$

$$R_H = \frac{\mu_1^2 n_1 - \mu_2^2 n_2 - \mu_1^2 \mu_2^2 B^2(n_2 - n_1)}{e\left\{(\mu_1 n_1 + \mu_2 n_2)^2 + \mu_1^2 \mu_2^2 B^2(n_2 - n_1)^2\right\}} \qquad \underline{3.6.}$$

which on neglecting terms of the order of B^2 gives

$$R_H = (\mu_1^2 n_1 - \mu_2^2 n_2)/e(n_1 \mu_1 + n_2 \mu_2)^2 = (1 - ab^2)/n_1 e(1 + ab)$$
$$\underline{3.7.}$$

$$\frac{\Delta \rho}{\rho_0} = n_1 n_2 \mu_1 \mu_2 B^2 (\mu_1 + \mu_2)^2 / (n_1 \mu_2 + n_1 \mu_2)^2$$

$$= ab(1 + b)^2 \mu_2^2 B^2 / (1 + ab)^2 \qquad \underline{3.8.}$$

where $\rho_0 = (n_1 e \mu_1 + n_2 e \mu_2)^{-1}$ is the resistivity in zero magnetic induction, and $a = n_1/n_2$, $b = \mu_1/\mu_2$.

Now in graphite, Soule (1958a) has shown that the densities of the two carriers are almost equal, i.e. $a = 1$ and $n_1 = n_2 = n$.

Therefore in this approximation

$$\Delta \rho/\rho_0 = b\mu_2^2 B^2 = \mu_1 \mu_2 B^2 = \mu_{av}^{o\,2} B^2, \text{ where } \mu_{av}^o = (\mu_1 \mu_2)^{1/2} \qquad \underline{3.9.}$$

and $R_H = (1 - b)/n_1 e(1 + b)$, or $b = (1 - R_H n_1 e)/(1 + R_H n_1 e)$
$$\underline{3.10.}$$

From the experimental data using 3.10.b is found to be almost equal to one. Thus $1/b = 1$ and the zero magnetic induction resistivity is given by $\rho_o = (en_2\mu_2 b(1/b + a))^{-1} = (2en_2\mu_{av})^{-1}$. Therefore $n_{total} = n_1 + n_2 = \left[\rho_o e(\Delta\rho/\rho_o B^2)^{1/2}\right]^{-1}$.

It can now be seen that if the zero induction resistance, the magnetoresistance, and the Hall coefficient are known for low magnetic induction, the mobilities of each carrier and the total density of carriers can be calculated.

The limit for the low induction coefficients is given by the condition $\mu_{av}^o B < 0.15$ as can be seen by examining Fig. 6. of Soule's paper (1958a). As the temperature decreases, and the mobility increases the above condition becomes difficult to fulfil, the lowest induction at which measurements can be made being 0.03 W/m^2. Soule (1958a) has shown that the temperature dependence of the average mobility μ_{av} at a particular value of induction is independent of the magnetic induction out to 0.8 W/m^2 and down to 77^oK, and gives the temperature dependence of his samples as $T^{-1.2}$. Many workers have taken this as an indication of the perfection of their material and it will also be used for this purpose here. To obtain the true mobilities, that is, the value calculated in the low induction limit, it is necessary to use the following procedure.

In the present work, the measurements are all made at an induction of 0.286 W/m^2, this being a convenient value near to Soule's 0.3 W/m^2. Using values for the mobility

from Fig. 6. of Soule's paper a graph of μ_{av} against $\mu_{av}^{O}B$
is plotted, and a series of curves parallel to this are
drawn, each with the low induction limit at $\mu_{av}^{O}B = 0.15$.
It is then noted that the values for μ_{av} for a particular
value of B all lie on a straight line which crosses these
curves at an angle of $\pi/4$. (See Fig. 10.). The line for
$B = 0.286 \text{ W/m}^2$ was drawn. The values of μ_{av}^{O} were then deduced
from this graph knowing the value at 0.286 W/m^2. This method
can be employed because the variation of μ_{av} with magnetic
induction at various temperatures lies on these curves,
as is shown in the Fig. 10.

It is further justified by the fact that this method
gives Soule's tabled values of μ_{av}^{O} (Table III of 1958a)
within 5% from his graph of μ_{av} against T at 0.3 W/m^2 (Fig. 7
of 1958a).

The Hall coefficient was found to be independent of
the induction down to $80^{O}K$, as long as the induction was less
than 0.5 W/m^2, and no unusual low induction behaviour was
noted.

Recently McClure and Smith (1963) have reported the
preliminary results of some calculations using the correct
energy equation to give the galvanomagnetic coefficients and
the Seebeck coefficient. Their preliminary results are in
moderate agreement with experimental data.

FIGURE 10

GRAPH OF μ_{av} AGAINST $\mu_{av}^\circ B$

μ_{av}

30.0
M^2/V SEC

$B = 0.286$ W/M^2

SOULE

3.0

20A 85°K

22D 83°K

SOULE
20A 300°K

1.0

0.3

0.3   1.0   3.0 $\mu_{av}^\circ B$
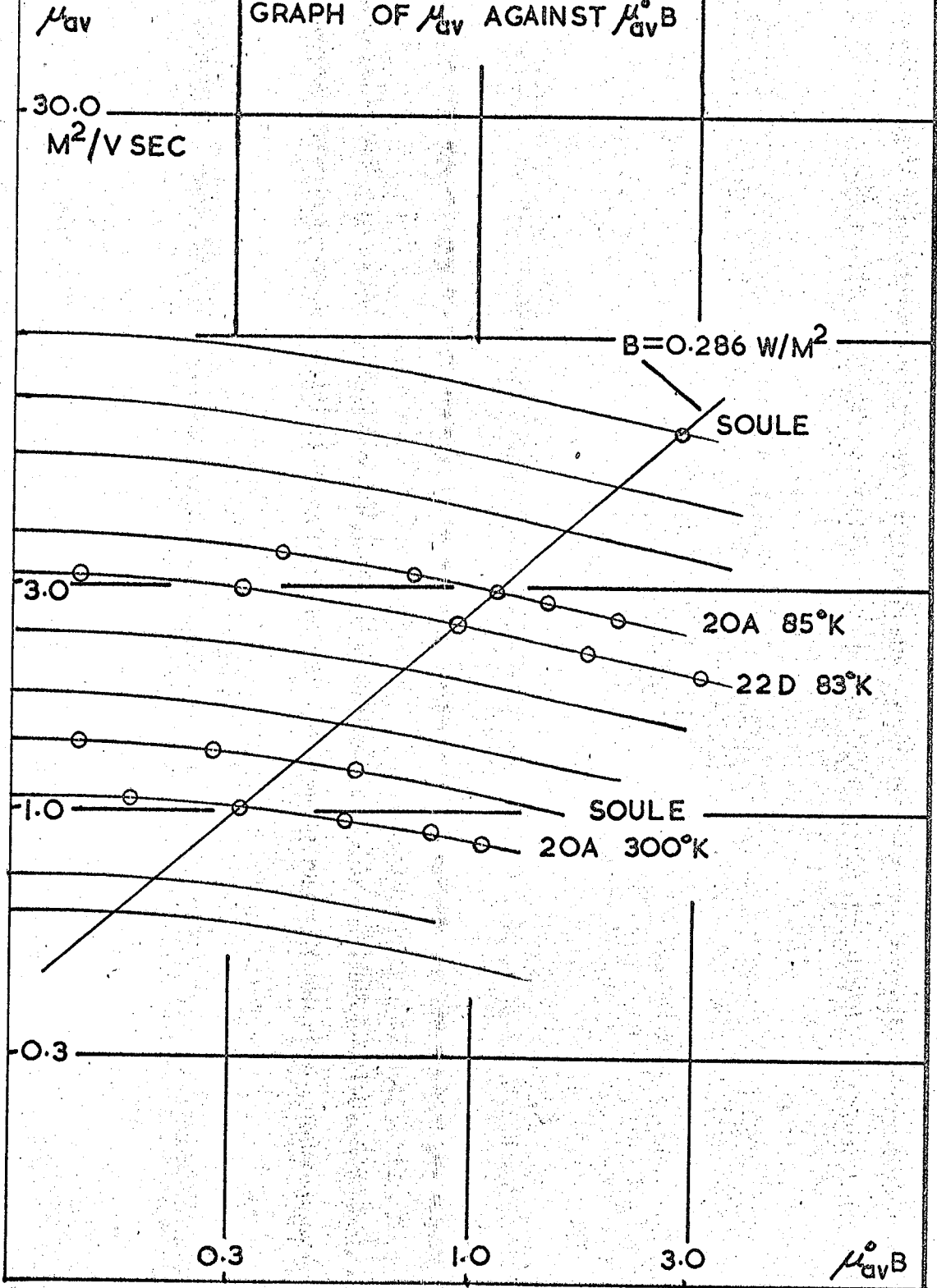
CHAPTER IV

Thermomagnetic Effects

1.4.1.   Introduction

Thermomagnetic effects (hereinafter T.M.) were discovered in the late nineteenth century in bismuth and were the subject of many experiments and theories during the next few years.   It is interesting to note that Gottstein (1923) investigated several of these effects in graphite.

For many years they were only of academic interest, since the galvanomagnetic effects are much simpler to analyse to give information on the transport properties, and no material had a large enough effect to be of use commercially.

However, with the advent of many new semiconductors, and much purer samples of the old materials, T.M. effects are being used increasingly as useful tools for investigation of transport properties (Tsidil'kovski 1963) and for energy conversion (Harman and Honig I, II, III, IV, V, 1962-63, Wright 1962, Ure 1960, El-Saden, 1962, and many others).

The prospects for refrigeration down to liquid helium temperatures are improving as the investigations proceed and new and better materials are discovered.   Thermoelectric effects are now in use for refrigeration and for the conversion of heat to electricity.   Theoreticians predict that

better efficiencies should be obtainable using the thermo-
magnetic effects.

Expressions (for the thermomagnetic coefficients)
similar to equations 3.5, 3.6 can be derived (Putley 1960).
These expressions are obtained by combining equations 2.14
with Tables II and III and rearranging. They are very useful
if the coefficients for the individual parameters can be
measured. They give the same results however as those obtained
from the computor programme described below, if the individual
coefficients are calculated with the same assumptions as
those employed here.

1.4.2. Application of the Theory of Thermomagnetic Effects to Graphite

In Chapter II the Boltzmann equation was solved and
the phenomenological equations derived. Using the definitions
and conditions given in Table III the expressions for the
various effects are derived. Because of the complexity of
the expressions for the coefficients only the case of the low
magnetic induction coefficient for the transverse Nernst
Ettingshausen effect is derived analytically. However, with
such a large mobility in graphite (5.0 m^2/V sec at 100^OK)
the low magnetic induction condition means that inductions
of less than 0.1 W/m^2 must be used at low temperatures. Later

a computer was used to calculate the coefficients over a larger range of the magnetic induction.

Only the longitudinal and transverse Nernst-Ettingshausen coefficients were computed since the other effects require a term in the lattice thermal conductivity which is difficult, if not impossible to predict theoretically, especially in a polycrystalline material like pyrolytic graphite, in which it can vary by an order of magnitude from one sample to another.

1.4.3.   The Integrals I_{ij}.

These integrals contain terms in k, τ and E, and it is necessary to convert these to one variable, usually $x = E/kT$. To do this the relations $E = (\hbar k)^2/m$ and $\tau = \tau_0 x^{r-1/2}$ are used, but to eliminate the constant terms such as τ_0 it is best to resort to a mathematical trick (Tsidil'kovski 1963). In this are used the relations

$$n = \frac{1}{3\pi^2}\int_0^\infty k^3 \frac{df_0}{dk}\, dk \ , \quad \text{and} \quad \mu^0 = e\frac{\int_0^\infty k^3 \frac{\tau}{m} \frac{df_0}{dk}\, dk}{\int_0^\infty k^3 \frac{df_0}{dk}\, dk} \qquad \underline{4.1.}$$

The latter relation can be derived from the zero magnetic induction conductivity. On multiplying and dividing by the appropriate power of n and μ^0 it can be shown that

$$I_{ijm} = \frac{(\mu_m B)^{i-1} \frac{n_m \mu_m}{e} (kT)^j \int_0^\infty x^{(3/2+i(r-1/2)+j)} \frac{df_o}{dx} (1+W^2 x^{2r-1})^{-1} dx}{\int_0^\infty x^{3/2} \frac{df_o}{dx} dx}$$

$$\left[\frac{\int_0^\infty x^{3/2} \frac{df_o}{dx} dx}{\int_0^\infty x^{r+1} \frac{df_o}{dx} dx} \right]^i \qquad \underline{4.2.}$$

where $W = \mu' B$ and $\mu' = \mu^o \frac{(2r+2)}{3} (kT)^r \frac{F_r(E_f)}{F_{1/2}(E_f)}$ $\qquad \underline{4.3.}$

μ^o is the classical mobility for lattice scattering. Equation
4.3 is derived from equation 4.1. To simplify computation
classical statistics were assumed which makes equation 4.3.,
$\mu' = \frac{4}{3\sqrt{\pi}} \mu^o$ for $r = 0$.

Writing this as

$$I_{ijm} = \frac{(\mu_m n_m)}{e} (\mu_m B)^{i-1} (kT)^j a_{ijm} \qquad \underline{4.4.}$$

where the a_{ijm} are the actual integrations, equations 2.14
become

$$I_{10} = \frac{\mu_2 n_2}{e} (a_{102} + aba_{101}) = \frac{\mu_2 n_2}{e} I'_{10}$$

$$I_{20} = \frac{\mu_2^2 n_2}{e} (a_{202} - ab^2 a_{201}) B = \frac{\mu_2^2 n_2}{e} B I'_{20}$$

$$\qquad \underline{4.5.}$$

$$I_{11} = \frac{\mu_2 n_2}{e} (a_{112} - aba_{111} + E_g^* a_{102}) kT = \frac{\mu_2 n_2}{e} kT I'_{11}$$

$$I_{21} = \frac{\mu_2^2 n_2}{e} (a_{212} + ab^2 a_{211} + E_g^* a_{202}) BkT = \frac{\mu_2^2 n_2}{e} kTB I'_{21}$$

where $E_g^* = E_g/kT$, and $a = n_1/n_2$, $b = \mu_1/\mu_2$.

In the case of low magnetic induction, the integrals a_{ijm} can be expanded in terms of $(\mu B)^2$ and terms of the order of $(\mu B)^2$ neglected. The a_{ijm} then become a_{ijm}^o where

$$a_{ijm}^o = \frac{F_{(1/2+i(r-1/2)+j)}}{F_{1/2}} \left(\frac{3F_{1/2}}{2F_r}\right)^i \frac{(3+2j+i(2r-1))}{3(r+1)^i} \qquad \underline{4.6.}$$

(Tsidil'kovski 1963), and the F_m are the Fermi integrals.

1.4.4. <u>The Computer Programme</u>

The programme was written in Elliot Algol, a language in which the calculations need not be broken down into simple arithmetic steps. The programme starts by filling the elements of a three dimensional array $I(i,j,m)$, computing the integrals a_{ijm} by using Gauss' procedure. Since the integrand is sharply peaked due to the term $\frac{df_o}{dx}$ and is very small for all x greater than 15 the integration is split into two parts, each part consisting of five steps. The accuracy is such that when a Fermi integral is calculated the difference between the computed and tabled value was only one part in 10^5. This was felt to be accurate enough for this purpose.

Before these elements can be calculated, the parameters r, E_g^*, E_f^*, W and b are needed.

Soule has shown that in single crystal graphite, lattice scattering predominates except at the lowest tempera-

tures. Since the original idea of the programme was to
calculate the transverse Nernst-Ettingshausen coefficient
for perfect graphite the scattering parameter in the programme
was given the value of 0. In pyrolytic graphite however, the
crystallite boundaries introduce additional scattering with
a different parameter r. This extra scattering term will
be discussed later.

E_g^* and b are read in as 'control' parameters. That is
to say, these are used to control the length of the programme,
a set of these parameters being read in signifying the
beginning of a new calculation. A third parameter N stops
the programme when there are no more sets of the above two
parameters to be read in.

After reading these W is set equal to 0 and looped
through the following values 0.2, 0.5, 1.0, 2.0, 4.0, 6.0, 8.0,
10.0. Having given W a value, the programme sets $E_f^* = - 0.5E_g^*$,
and increases it by $- 0.2E_g^*$ until it reaches $- E_g^*$. For each
value of E_f^*, the elements I(i,j,m) are calculated. a is then
given a value of 0.9 and the elements of a two dimensional
array IT(i,j) are calculated according to equations 4.5,
without the terms outside the square brackets. These elements
are then combined to give the longitudinal and transverse
Nernst-Ettingshausen coefficients. a is then given the values
of 1.0, and 1.1 and this repeated.

The results are printed in the form of a table an example of which is given in Appendix A. A copy of the programme is given in Appendix B.

1.4.5. The Transverse Nernst-Ettingshausen Coefficient

Using the conditions of Table III, Chapter II, the following equation can be derived from equations 2.11:-

$$Q_{12}^i B = \frac{1}{eT} \frac{(I_{11}I_{20} - I_{10}I_{21})}{(I_{10}^2 + I_{20}^2)} \qquad \underline{4.7.}$$

On using the equations 4.5 this becomes:-

$$Q_{12}^i = \frac{k}{e} \mu_2 Q', \text{ where } Q' = \frac{(I_{11}'I_{20}' - I_{10}'I_{21}')}{(I_{10}'^2 + I_{20}'^2 \mu_2^2 B^2)} \qquad \underline{4.8.}$$

is the expression calculated in the computer.

However to show the complexity of the expression for even a simplified case like that of the low magnetic induction the approximation Q' is written

$$Q' = \frac{I_{11}^o I_{20}^o - I_{10}^o I_{21}^o}{I_{10}^{o2} + I_{20}^{o2} \mu_2^2 B^2} \qquad \underline{4.9.}$$

where the I_{ij}^o are given by equations 4.5 with a_{ijm}^o substituted for the a_{ijm}. When the substitutions are carried out in the above equation the following expression results:-

$$Q_{12}^i = \frac{k}{e} \left[\frac{K_1^2 + b^3 a^2 K_1^1 - ba \, (K_2^{21} + bK_2^{12}) + E_g^* \, (K_3^{21} + bK_3^{12})}{(a_{102} + aba_{101})^2} \right] \mu_2 \qquad \underline{4.10.}$$

where $\qquad K_1^i = (a_{20i}^O a_{11i}^O - a_{21i}^O a_{10i}^O)$

$$K_2^{ij} = (a_{20i}^O a_{11j}^O + a_{21i}^O a_{10j}^O) \qquad \underline{4.11.}$$

$$K_3^{ij} = (a_{20i}^O a_{10j}^O)$$

and the a_{ijm}^O are given by equation 4.6. and a and b are as before.

Using tabled values for the integrals $F_k(E_f)$ contained in the a_{ijm}^O's the coefficient can be calculated. It will be seen that these calculations are lengthy. Computing by hand, one value of Q_{12}^i took in the region of four hours. A computer programme was written to make use of the tabulated values of the Fermi integrals to calculate Q_{12}^i using equation 4.10. This was done more as an exercise in writing computer programmes than for the values of Q it produced, since it required that several values of the $F_m^i(E_f)$ be interpolated, obviously an unsatisfactory approach. However the values of Q_{12}^i obtained from this programme lie within one percent of those computed in the main programme for zero magnetic induction. The results of both these programmes are given in Part III.

1.4.6. The Longitudinal Nernst-Ettingshausen Effect

The equation for the coefficient of this effect is

$$\alpha(B) = \frac{1}{eT} \left[\frac{I_{11}I_{10} + I_{21}I_{20}}{I_{10}^2 + I_{20}^2} - E_f \right] \qquad \underline{4.12.}$$

which on using equations 4.5. becomes

$$\alpha(B) = \frac{k}{e} \left[\frac{I'_{11}I'_{10} + I'_{20}I'_{21}\mu_2^2 B^2}{I_{10}^{'2} + I_{20}^{'2}\mu_2^2 B^2} - E_f^* \right] \qquad \underline{4.13.}$$

where $E_f^* = E_f/kT$.

This is the relation used in calculating $\alpha(B)$ in the computer, except that the value of E_f^* is not subtracted.

No analytical expression was derived for this co-efficient. The results of these calculations are given in Part III.

PART   II

EXPERIMENTAL

CHAPTER   I

Preparation of Samples

2.1.1.   Preparation of Pyrolytic Graphite

The graphite was grown by R. A. Morant who designed
and constructed the apparatus. Only a brief description of
the process will be given here. The pioneering work on the
process was carried out by Brown and Watt (1958) whose apparatus
was used as a basis for the design used here.

A bar of polycrystalline graphite was heated resistively
to temperatures exceeding 2000°C in a vacuum furnace. Propane
gas, at a pressure of less than 200 millimeters of mercury,
was passed continuously over the hot bar on which it 'cracked'
depositing the carbon in a layered structure on the substrate,
the hydrogen and any other gaseous by-products being pumped off.
A temperature of at least 2000°C is found to be necessary to
grow material which has properties near to the single crystal
values. For instance the density falls well below the single
crystal value of 2.265 gms/cc for temperatures of deposition
less than 2000°C. (Brown and Watt 1958).

In the early samples the final cross-section of the
bar was limited by the power available to heat the bar as its
resistance decreased due to its increased cross-section. This
limitation in power also meant that the initial bars had to be

less than a critical cross-section if the final deposit was

to be thicker than 1 mm. Later, however, a larger power source

became available and the initial cross-section could be increased

and still thicker samples depositied. A typical example would

be an initial cross-section of 10 x 2 mm^2 increasing to

16 x 7 mm^2. These thicker deposits were used in an investigation

of the electronic properties throughout the thickness of the

bar. Photograph No.1.(a) shows the original bar and (b) shows

the same bar after the pyrolytic graphite had been formed. The

black shiny appearance of the bar in (b) is typical of the

product of this method of growing graphite.

The exact process by which the carbon atoms are deposited

is still under much discussion. An examination of a highly

polished cross-section of the deposit in polarised light under

a microscope, reveals that the structure is layered with growth

cones. In the barely graphitised deposits, the cones appear

to originate on the substrate and have a large semi-vertical

angle. The more highly graphitised specimens have a much finer

structure with many small angle cones some of which do not

originate on the substrate. This variation in structure is

shown in photographs No. 2 and 3 which are reproduced from a

paper by Harvey, Clark and Eastabrook, 1962.

2.1.2. Preparation of Samples

The samples on which measurements were made were cut

b

Photograph No. 3

from the bars by means of a thin Carborundum grinding wheel,
about 0.25 mm thick lubricated by a soluble oil. During the
cutting process the bar was held in position by sticking it
with Aerofix cement to a steel cylinder, which was clamped in
position by the magnetic chuck of the grinding machine.

Samples were usually cut about 3 mm wide and about
25 mm long from the widest flat side of the bar. Those from
some of the earlier bars, as mentioned previously (section
2.1.1.) were not as wide as this since the width of the widest
flat side was less than 3 mm. The photograph of a polished
cross-section (No.4) shows why, although the original bar had a
flat of 3 mm, a sample this wide could not be cut from the
final bar due to distortion of the layers by the corners.

After the sample had been cut out, but was still in
position, the whole bar was washed in acetone in a Soxslip,
in order to wash the sample free from the soluble oil, and to
free the bar from the fixing cement.

The sample peeled away from the substrate very easily
because of the layer of soot formed during the initial surge
of propane over the hot surface. This sample, varying in
thickness from one to three millimetres, was then cleaved
carefully along the layers into several specimens each a fraction
of a millimetre thick. These were the actual samples used for
the measurements.

The nature of the cleaved surfaces was such that they
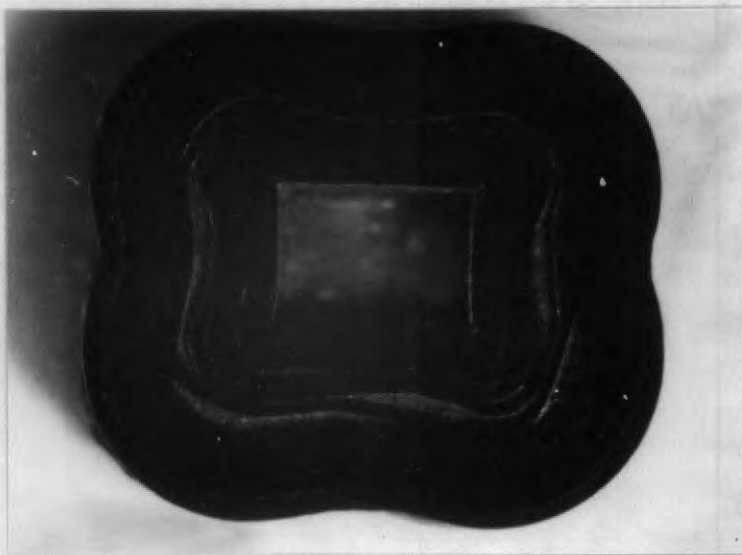
appeared to need grinding in order to give smooth flats on which to make accurate measurements of the dimensions. Samples were not usually ground for two reasons. The outside layers of some of the bars had stresses built in during the growing and cooling processes (Blackman and Ubbelohde 1962). This resulted in the samples being curved along their length, as in Fig. 11. The curvature on some was too great to allow the surfaces to be ground flat without starting on a specimen over a millimetre thick, and as is shown later, the properties varied widely over such a thickness.

A further more important reason for not grinding the cleaved surfaces was in the nature of the surfaces themselves. Due to the ʔgrowth coneʔ formation, the surfaces were not regular, but they were parallel. The contours of any particular layer followed the contours of the immediately adjacent layer exactly, so that the shape of one face of the specimen was an exact replica of its partner. This is shown in photograph No.5 where a ʔnoduleʔ formed on a larger particle of soot than usual can be followed through the thickness of the sample.

Soot deposited on the innermost layer was gently scraped away to reveal the shiny surface of the graphite beneath. This process was necessary since it was thought that the soot would affect the measurement of the bulk properties.

FIGURE 11
CURVATURE OF SAMPLES

SUBSTRATE

FIGURE 13
CIRCUIT DIAGRAM

galvanometer

terminal strip

standard resistance

shunt

accumulator

multiway switch

potentiometer

standard cell
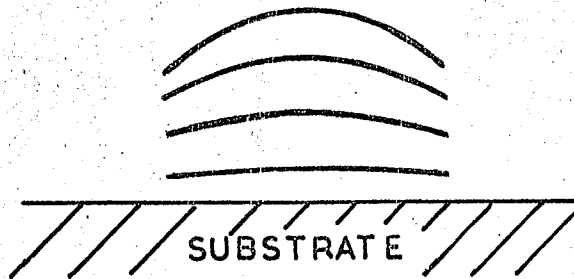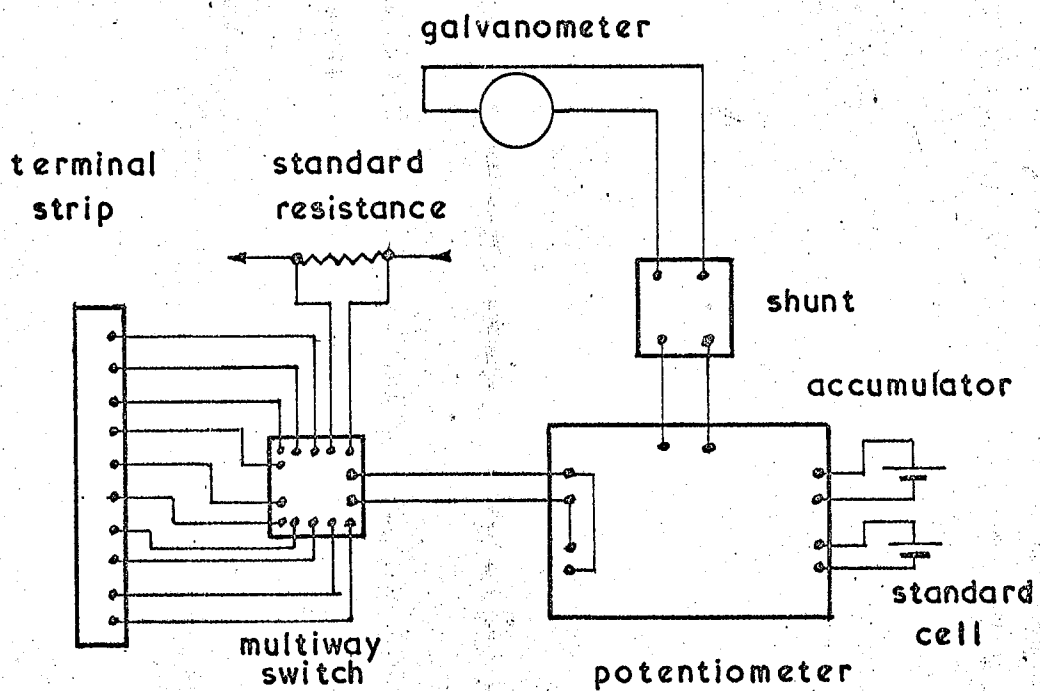
outer surface
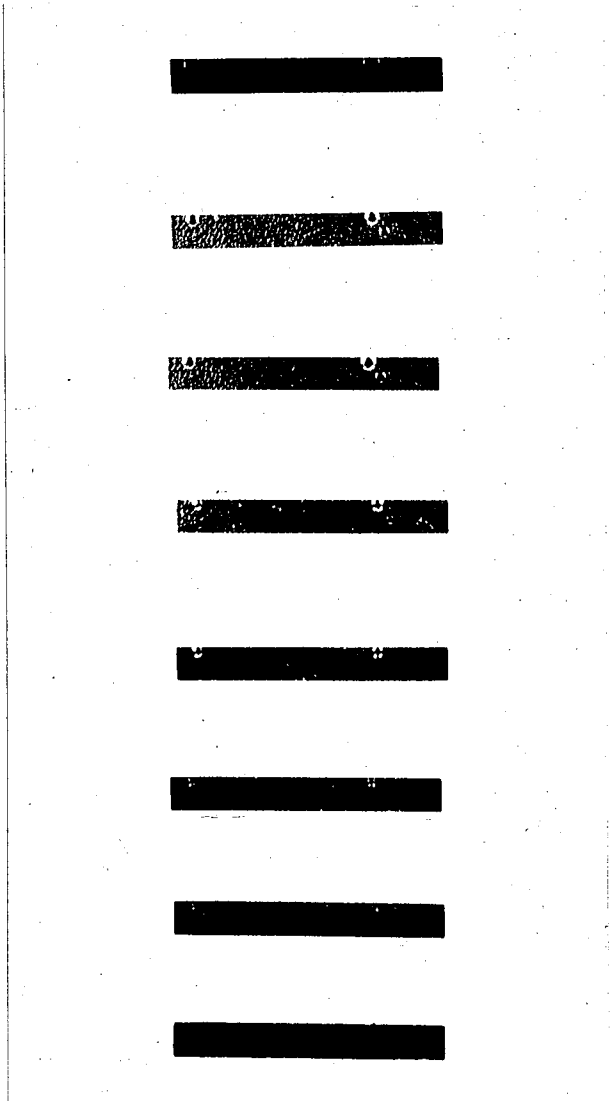
substrate

2.1.3. Dimensions

These were measured by two methods, one being a check
on consistent errors in the other. The width and the thickness
were determined by means of a travelling microscope. The
accuracy of this instrument was quoted to be 0.02 mm. In
measuring the width this was sufficient to determine this
dimension to 1 percent. The uncertainty was reduced even
further by taking the mean of several readings. It is thought
that the error in this measurement could therefore be ignored.

The width of the samples were measured by the same
method. With samples of a typical thickness of 0.2 mm, the
error in measurement due to the instrument became quite large.
This could be reduced by taking the mean of several readings,
but consistent errors could not be avoided by this method.
The readings were checked on a micrometer screw gauge. The
error in this measurement was therefore less than 2 percent.

2.1.4. The Samples

Since the original purpose of making the pyrolytic
graphite was to produce as near single crystal graphite as
possible, the conditions of growth were purposely varied from bar
to bar. The following sections set forth the conditions of growth
for each of the bars used for measurement. Also included are
a few density and x-ray measurements which were made in order
to give a rough estimation of the quality of the graphite.

The four bars used for the measurements were numbers

6, 10, 20, 22. These were chosen because they each marked a point where a definite improvement was made in the growing technique, producing the best material at that time.

Since R. A. MORANT was primarily concerned with the growing process the facts in the following paragraphs are reproduced with her kind permission.

2.1.5. Bar No.6.

This bar was grown during the first run in which there was full water cooling to the electrode system. A rough pressure controller was used in this run but its pumping speed proved to be too low to allow the pressure to be kept steady. Later a proper Cartesian Manostat supplied by Edwards High Vacuum was fitted. During the run a fault developed in the power supply making a temporary shut down necessary. The polished cross-section shown in photograph No.4 shows the sooty layer which developed then.

X-ray powder photographs from both sides of the fault indicated that this deposit was fairly well graphitised but definitely not single crystal. The original filament had a cross-section of 3×2 mm^2 which increased to 9.5×7.5 mm^2, giving a sample of just over 3 mm thick.

2.1.6. Bar No. 10.

The pressure and temperature during this run were under control for the first time. In addition, with this bar the

corners were rounded off, but there was still some distortion

of the layers by the corners. The original cross-section of

10 x 2 mm^2 increased to 13 x 4.5 mm^2.

Specific gravity measurements made on this bar indicated

that its density was approaching the theoretical x-ray value

of 2.26 gm/cc.

The x-ray photographs indicated that while the deposit

was more highly graphitised than previous bars it was still

very far from being a single crystal.

2.1.7. Bar No.20.

Previous evidence (Ubbelohde 1962) coupled with the

measurements on earlier bars, indicated that the graphite at

the inside of the thicker deposits was much better than the

average. The reasons for this will be discussed in detail

later. This bar was grown with the aim of seeing to what extent

this improvement was increased by making the final cross-section

as large as possible. Since the power was limited, the original

bar had to have as small a cross-section as possible. The

cross-section of the bar used measured 3 x 2 mm^2 and it increased

to 8 x 6.5 mm^2.

The pressure of the propane in this run was increased

from the usual 50 to 150 millimetres of mercury in order to

see what effect the pressure had on the growth rate. The run

following had a pressure of 50 torr for a direct comparison,

but there seemed to be no correlation between pressure and

deposition rate. No x-ray or specific gravity measurements were available for this bar.

2.1.8. Bar No. 22

This was the first bar to be deposited with a larger power supply (60 kilowatts). The temperature of deposition was now increased to $2200^{\circ}C$, the original cross-section was larger than usual, 10×2 mm^2, and the final thickness of graphite was greater than 2 mm.

In order to avoid the initial surge in the pressure created when the power was switched on, the pressure was reduced to 20 mm mercury and allowed to build up slowly to the set pressure of 50 over the first 10 minutes. Probably because of this, the growth rate was much slower than usual, being approximately half the normal rate. This slow rate of growth meant that the run had to be interrupted overnight. On re-starting, it was found that the growth rate had doubled and was about normal. This was probably due to the formation of soot in the previous day's run forming nuclei for deposition. In spite of the shut down a continuous deposit was formed. The final cross-section of the bar was 16×6.5 mm^2. It was estimated, from data taken from Moore, Ubbelohde and Young (Moore 1962), that the temperatures of the innermost layer of the deposit was just greater than $3000^{\circ}C$.

It was expected that the bar would exhibit a sooty layer where the run was interrupted overnight. However,

examination of the cross-section under a microscope showed that the bar was deposited uniformly.

X-ray photographs of various parts of the bar taken with a single crystal camera indicated that, near the substrate, the crystallites were aligned with their c_o axes accurately parallel, but were otherwise randomly oriented. Near the outside, the c_o axes were not so well aligned, and the dots of the near single crystal material of the inside layers became the arcs of circles of a more polycrystalline material.

This variation of the properties was investigated in great detail in this bar and will be discussed later.

CHAPTER II

Apparatus

2.2.1. Introduction

The apparatus described in this chapter was designed to meet the special requirements of measuring both thermo- and galvanomagnetic effects over a range of magnetic fields at low temperatures, in graphite of varying degrees of perfection.

2.2.2. The Magnet

The magnetic induction for the measurements was supplied by a 4 inch Electromagnet, powered by the standard 120 volts D.C. supply in the building. It was a copy, with modifications, of one already in use in the department. The modifications were mainly in the arrangements for adjusting the gap in the pole pieces and in the insulation of the windings. The original design allowed the gap to be adjusted by screwing the pole pieces in and out. The new magnet was designed with fixed pole pieces and the gap was adjusted by screwing on pole tips of different length. Improved insulation on the windings allowed it to be run at higher temperatures.

A gap of 2.5 cms was chosen for reasons which will be discussed in detail later. With this gap the maximum attainable value of induction was 1.0 W/m^2. The uniformity at this value

was 0.2 percent over a volume of 19 cms^2.

The 120 volts supply was connected to the magnet as shown in figure 12.
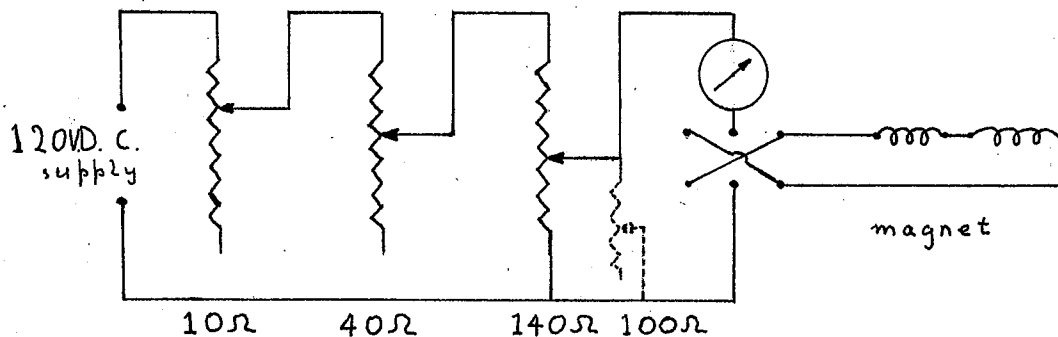
Fig. 12.

This arrangement allowed the current to be controlled over the whole of its range 0 - 12 amps, a dual range ammeter (0-5, 0-15 amps) being used for measurement. A specially designed switch was used for the shunt. In particular the lower end of the range of magnetic induction (up to 0.2 W/m^2) could be controlled to the same accuracy ($\pm$2 percent) as the larger fields for determining the low magnetic field dependence of any effect. To facilitate the control of the current at this low field end, an extra circular rheostat was connected in parallel.

As there was no means of rotating the magnet to reverse the magnetic field, a large reversing switch was used. This, however, complicated matters at the lower end of the range, because of the remanence field. When the field was to be

reversed, the current was first reversed, increased to a much larger value, reduced to zero, and finally increased to its original value. Using this technique, the magnetic induction could be set to within 0.002 W/m^2. In the large induction region, i.e. above 0.2 W/m^2, the error in just reversing the current was negligible, so that no special technique was necessary. In this region however, the fluctuation of the mains passing through the rectification system, caused small fluctuations in the field which could be picked up by the larger effects, e.g. the magnetoresistance, thus limiting the accuracy with which these measurements could be made. No cooling was needed even at the largest fields since the power consumed was only $1\frac{1}{2}$ kilowatts, which could easily be dissipated by the magnet. Provision for forced air cooling was incorporated in the coil windings, should a higher voltage power supply become available but this was never used.

2.2.3. Measuring Equipment

Since graphite, even in its worst form, is a low resistance semi-metal, the impedance shown to any measuring equipment will always be low. This means that normal potentiometer arrangements can be used for measurements. The circuit diagram is shown in Fig. 13.

Early measurements were made on a Tinsley potentiometer type 3387 B which used a slide wire arrangement. This made the measurement of small e.m.f.'s, i.e. below 5 microvolts impracticable, since the slide wire could not be set to better than 2 microvolts with any accuracy.

Later, more precise measurements were made on a Tinsley microvolt potentiometer type 4025 C in conjunction with a high sensitivity galvanometer. Since the potentiometer arrangement gave steps of one microvolt, by interpolating the deflection of the galvanometer, e.m.f.'s of a fraction of a microvolt could be detected. The ultimate sensitivity depending on the impedance of the voltage source, each source had to be calibrated individually.

With e.m.f.'s of this order to be detected, special precautions in the circuitry associated with the leads were necessary.

All exposed terminals were covered with blocks of 'Expanded Polystyrene' or 'Styrofoam' to shield them from draughts and radiation. The leads coming through the pinch seals in the cryostat (see section 2.2.4.) were sealed in with high vacuum black wax rather than by soldering, since it was found that soldering strained the fine wires used, rendering readings sensitive to the temperature of the seal. Since this could not be guaranteed from day to day, black wax was used. The leads coming from the cryostat and the reference

junction of the thermocouple were connected into a terminal strip behind the control panel of the whole apparatus. In this position, this junction, the most important, was shielded from draughts and radiation, but was accessible, thus allowing various combinations of the leads to be connected easily to the measuring apparatus. The leads from this terminal strip were permanently wired to a Pye 2-pole 6-way switch, in which the makers claim to have 'virtually eliminated thermal e.m.f.'s. Thermal e.m.f.'s are certainly less than 0.1 μV. The leads from the switch were connected to the terminals of the potentiometer. As this item possessed two sets of terminals, these were wired together so that its switch became a reversing switch, in order to accommodate e.m.f.'s of opposite polarity without having to touch the leads.

Using these precautions, the e.m.f. from two copper leads attached to a sample inside the cryostat at 82°K was less than 0.5 microvolts. However, the galvanometer used produced much larger e.m.f.'s by the heat of its light beam. It was found that by leaving the lid of the galvanometer box ajar, sufficient cooling was obtained to reduce this e.m.f. to about 0.1 microvolts. Since this was not reversible by the switch on the potentiometer, it could be detected and the results adjusted accordingly.

2.2.4. Cryostat

The design of this cryostat was developed to meet
the requirements of as low a temperature as possible in as
high a magnetic field as possible. If conventional dewars
had been used the gap would have been larger with a consequent
reduction in magnetic field. Since a gap of 2.5 cms in the
magnet's pole pieces gave a convenient value of 1.0 W/m^2, this
was used and the cryostat designed to function in this gap
without the use of conventional tailed dewars. The basic
idea of the design was used by Hurd (1962) for a cryostat to
measure optical properties at low temperatures. The coolants
to be employed were liquid nitrogen, solid carbon dioxide
powder in methanol and ice and water. If temperatures lower
than that attained using liquid nitrogen were required the
nitrogen could be pumped to its triple point 63.5^{O}K, thus
lowering the minimum temperature another 14°K. Below this
the nitrogen became solid and heat transfer became difficult.

The cryostat consists of three main parts as shown in
Fig. 14; the cryostat head, the cold reservoir and the
connecting tube.

The 'head' performs four functions:-

1)   It allows access to be made to the interior of the
cryostat, by means of a brass plate and an O-ring seal.

2)   Electrical leads to the sample holder enter the cryostat
through two 12-way pinch seals soldered into the brass plate.

FIGURE 14

THE CRYOSTAT

PINCH SEALS

ELECTRICAL LEADS

to vacuum

O-RING SEAL

'HEAD'

B CENTERING BUSH

CONNECTING TUBE

SAMPLE HOLDER

A, CONED JOINT

DEWAR

REFRIGERANT

D, HEAT SINK
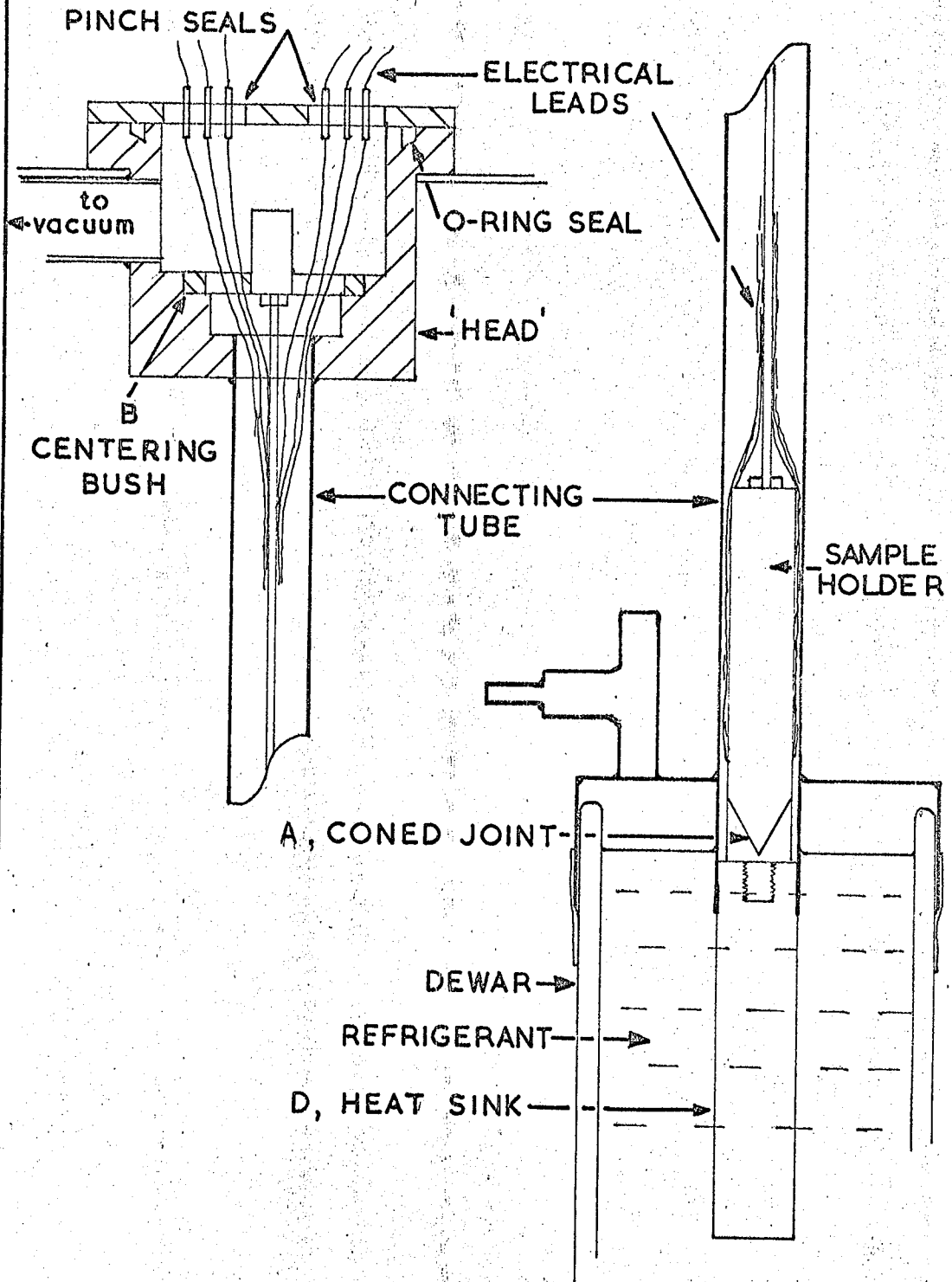
3)   The cryostat can be evacuated through it, connection to the vacuum system from the 'head' being through a 1 inch nominal diameter copper tube terminating in a 1 inch Speedivac valve, with demountable couplings, to facilitate dismantling.

4)   The cryostat, with the sample holder inside, is suspended in position by a flange on the 'head'.

The cold reservoir is a cylinder of copper 1 inch in diameter, $4\frac{1}{2}$ inches long, immersed in a suitable cryogenic liquid, in a 2 litre dewar, situated immediately below the pole pieces of the magnet. In the top face of this cylinder, there is a 3/8th inch B.S.F. tapped hole, half an inch deep, into which is screwed the female end of a coned joint (A). This arrangement allowed the joint to be removed from time to time and cleaned off the excess grease used to make good thermal contact.

The connecting tube was Nickel Silver with an outside diameter of just under 1 inch. This was hard soldered to the top end of the cold reservoir and the bottom face of the 'head'. As Nickel Silver is a poor conductor of heat, the cryostat head remained at room temperature making the vacuum seal simple no matter what cryogenic liquid was in the dewar. Nickel Silver was also non-magnetic and therefore did not affect the magnetic field.

The sample holder had the male end of the coned joint at the bottom end of it and the position of the cryostat was

adjusted so that the sample, in the holder, was exactly in the centre of the pole tips.

This arrangement meant that nearly all of the 1 inch gap of the magnet was available for evacuation and there was plenty of room for the sample holder. However, since the outer walls of the cryostat around the sample holder were at a much higher temperature than the sample, a radiation shield around the sample was needed.

In order to pump the liquid nitrogen, a brass cap on the dewar, below the gap of the magnet, was soft soldered to the connecting tube. A rough vacuum seal between the dewar walls and the cap was made by making the cap a close fit on the outside wall of the dewar and sliding a piece of inner tubing over the join, as in Fig. 14. The outlet tube on the top of the cap was a T junction so that the dewar could be evacuated through one arm and topped up through the other. A high capacity rotary pump was employed to pump the liquid nitrogen. Because the heat flow down the walls of the cryostat was large, this technique did not give very stable temperatures due to liquid level fluctuations.

The inside of the cryostat was pumped down to less than 10^{-5} mm mercury by means of an oil diffusion pump, backed by a rotary pump. The high vacuum conditions around the sample were needed to avoid losing by convection the small temperature differences created by some of the effects such as the Ettings-

hausen (see section 1.2.4). A one inch Speedivalve enabled the cryostat to be isolated and let down to air without stopping either pump. A roughing line, by-passing the diffusion pump, was incorporated in the system. This arrangement enabled samples to be changed without waiting for the diffusion pump to cool down.

The pressure in the system was measured on a Pirani gauge, which was calibrated against a McLeod gauge.

2.2.5. Sample Holder

The sample holder is designed to be an integral part of the whole cryostat, insofar as it must have the radiation shield, and the coned joint at the lower end. A diagram of it is given in Fig. 15 where these two parts can be seen clearly. The two halves of the joint were turned on the same setting of the lathe, so that they matched exactly. However to improve thermal contact, both surfaces were smeared with Silicone high vacuum grease. The radiation shield (A) was made as thick as possible so that there was negligible temperature gradient along it, due to any radiated heat flowing down it. To the top of this shield was attached a thin walled 1/8 inch diameter Nickel Silver tube, by which the holder was lifted out. The top end of this tube was screwed into a centering bush (B) by which the complete sample holder assembly could be rotated. The thin walled tube was also used

FIGURE 15

THE SAMPLE HOLDER

TO B
THE CENTERING BUSH

SUPPORTING TUBE

HEATER

A
RADIATION SHIELD

E
TUFNOL FORMER

LEADS

C
MAIN HEATER

CONED JOINT

D
HEAT SINK
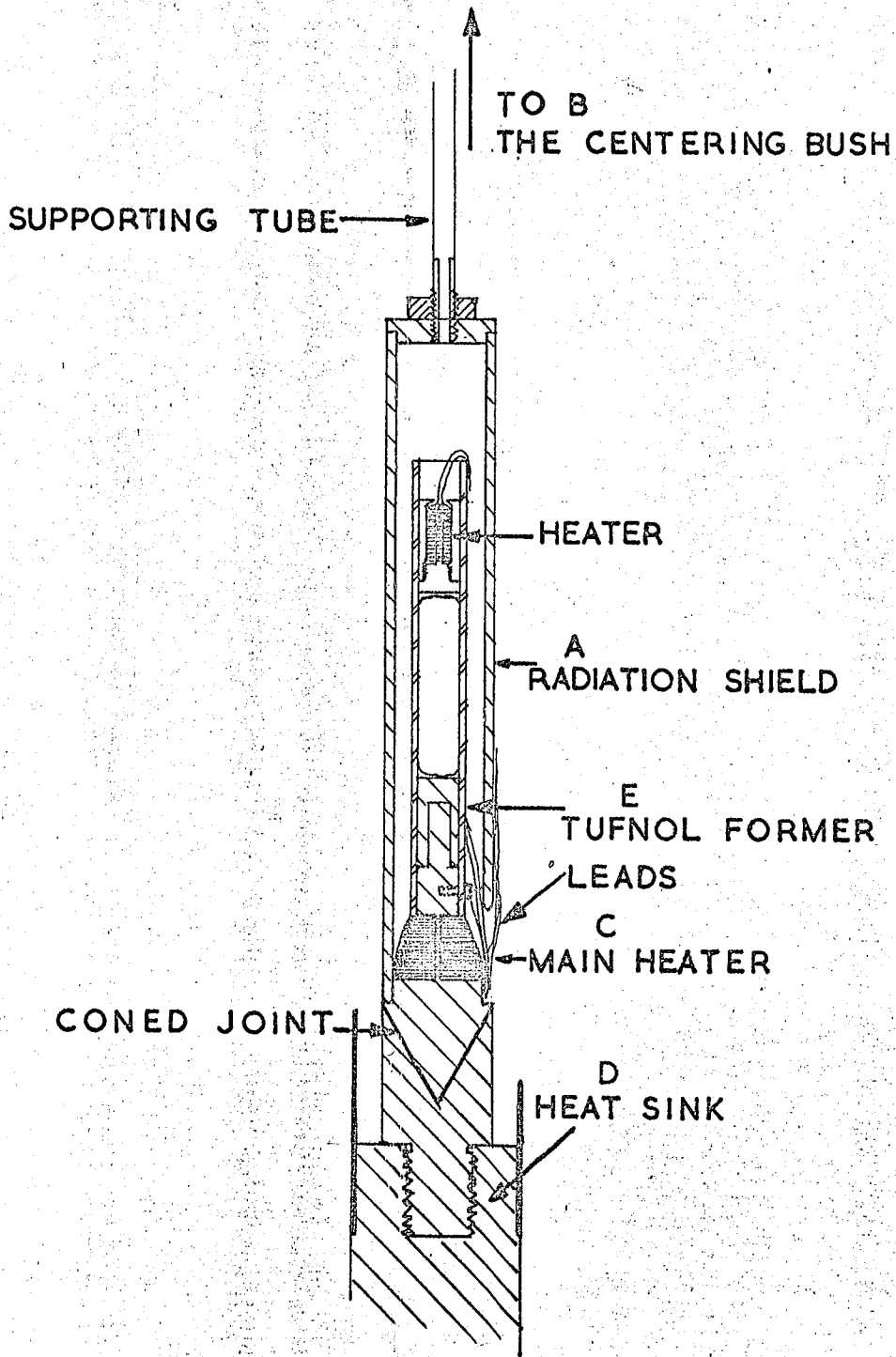
to support the electrical leads. In order that the angular dependence of any effect on magnetic field could be investigated, this bush was marked every 5° around its circumference, and an appropriate mark made on the cryostat head.

The sample holder itself, inside the radiation shield, consisted of three main parts: the heater, (C) the heat sink (D) and a Tufnol support for the heater and the electrical leads (E). Tufnol was chosen for this latter item because it was found that its coefficient of expansion was similar to that of graphite. The position of the heat sink was adjustable by sliding on a small spigot in order to accommodate different lengths of sample. As can be seen from the diagram, the small spigot was isolated from the cold source by a recess, in which was wound a 30 watt heater. This heater acted as a heat switch controlling the amount of heat flowing to or from the sample, thus controlling its ambient temperature. The radiation shield fitted tightly on another recess below this heater, being therefore independent of the control heater, and thus colder than the sample. The small heater, used to supply the temperature gradients along the sample, was a small cylinder of copper with the heating coil imbedded in Araldite, inside it. Its outside diameter was such that it was a tight sliding fit in the inside of its support. This meant that, once in position, its weight was born by the support and imposed no strain on the samples, some of which were quite soft.

CHAPTER III

Experimental Details

2.3.1. Contact Materials.

In use, the sample, usually a rod $2.5 \times 0.3 \times 0.03$ cm^3, rested in slots in the heater and heat sink end faces. Contact, both electrical and thermal, between the sample and these copper end faces was made by painting the area of contact with a silver dag, a dispersion of silver in methyl isobutyl ketone (M.I.B.K.). This proved to be the most reliable method of making contact to the samples after trying many other methods. Because of the high anisotropy of graphite, care had to be taken to ensure good contact with the sides of the sample. This made sure that all the basal planes carried current, thus giving a uniform current density across the thickness of the sample. For the same reason voltage and temperature probes had to be on the side, in order to measure the potential or temperature averaged over all the planes.

Contact between the probes and sample proved to be a major problem. At first Soule's technique (Soule 1958a) of copper plating and soldering with a low melting point solder was tried, without much success, since samples were often sooty and the copper did not adhere very well. Soldering with Wood's metal to a coating of silver dag was then tried

again without success since the soldering tended to remove

the layer of silver. The most reliable method, however,

proved to be to paint the area of contact with silver dag,

and before it had dried, place the probe in position. When

the M.I.B.K. had been baked out (a convenient oven being

an Anglepoise lamp), the probe was usually in good electrical

and thermal contact with the sample. A useful measure of

the contact resistance was the sensitivity of the potentio-

meter when the appropriate leads had been connected up.

It was found that the sensitivity between two copper leads

connected to different places on the sample was of the order

of 15 mm per microvolt. If the sensitivity was less than

this then a bad contact existed and the contact was remade.

A further test was made when the cryostat was cooled down.

2.3.2. Probes and Thermocouples

Probes to measure the electrical potential at, and

the temperature of various points in the samples were attached

by the method described in section 2.3.1. The configuration

was as shown in Fig. 16
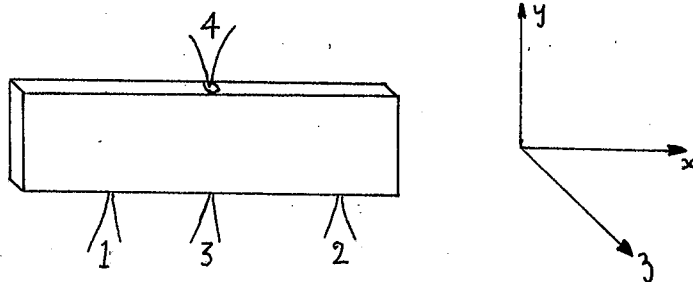
Fig. 16.

With this configuration of probes the magnetic field must be parallel to the c_o axis. This makes interpretation of the results simpler because of the isotropy in the planes, as discussed in sections 1.1.5. and 1.2.4. No measurements were made with any other configuration (e.g. the magnetic induction perpendicular to the c_o axis) as such measurements would have little meaning, due to the random orientation of the crystallites.

The probes were Copper-Constantan thermocouples. These were chosen since they gave a reasonable sensitivity at nitrogen temperatures, and since the copper leads could be employed to measure the electrical potential difference between the points of contact. 40 s.w.g. wires were chosen in order to minimise the heat losses to the sample holder.

The making and installing of thermocouples proved to be the major difficulty of this work. Straining of the constantan wire (which gave spurious e.m.f.'s) occurred very easily so that great care was necessary to avoid this at critical points in the wire, such as the anchoring point to the heat sink. Several techniques were tried, including a method suggested by Smirnov (1964), but none proved to be very reliable. Corrections of up to 5 microvolts had to be applied to the thermocouples in order to make them read the same at the same temperature, and this was not felt to be very satisfactory. However it proved to be impossible to have

two couples which consistently read the same after they
had been attached to more than one sample. Therefore the
following technique was adopted. On cooling down below
room temperature, the sample was allowed to reach equilibrium
and the thermocouples were checked to see if they read the
same. A simple method of checking whether the sample had
reached equilibrium was to switch on the magnet. If
potential difference could then be detected at the Hall probes,
then an estimate of temperature gradient could be calculated
assuming a rough value for the transverse Nernst-Ettingshausen
coefficient. The actual temperature difference when the
sample had reached equilibrium was usually less than 0.5
microvolts (Thermocouple output). On the best samples even
this small temperature difference gave a Nernst-Ettingshausen
field which could be measured.

The correction to be applied to the thermocouples
was only used to determine the temperature gradient, since
a few microvolts did not make much difference to the mean
temperature of the sample. The error involved in this technique
will be discussed in more detail later.

To cut down the heat influx to the sample as much as
possible, the wires were anchored to the heat sink by tying
them to it with thread and painting with a solution of
Polystyrene in toluene. When this had set, the wires were
thermally anchored to the sink. The wires remained anchored

to the sink even after repeated thermal cycling.

To avoid any further spurious e.m.f.'s caused by
the wires touching before they had reached room temperature,
the Constantan wire was threaded through Refrasil sleeving,
and, in addition, the wires were kept apart as much as possible
up to the cryostat head. To help achieve this they were
anchored to opposite sides of the heat sink.

2.3.3. Probe Separation

The separation of the 'Conductivity' probes (Nos. 1
and 2 in Fig. 16.) was measured by means of a travelling
microscope. The full accuracy of this instrument could not
be taken advantage of because of the large diameter of the
areas of contact of the probes. Care was taken to keep these
as small possible. However it proved to be extremely
difficult to make contact in an area of diameter less than
0.5 mm, a typical value being 0.6 mm. With an average probe
separation of 10.0 mm the error in this measurement was
therefore never less than 5 percent. This length is used
in calculating the resistivity and the transverse Nernst-
Ettingshausen coefficient. The error in these effects was
therefore never less than this value.

2.3.4. Alignment

With the probes in position and their separation

measured, the radiation shield could be fitted, taking care not to disturb the probes. To facilitate this a small jig was made to allow the shield to slide over the sample holder uniformly. The holder could now be fitted in the cryostat using a thin film of high vacuum grease on the coned joint to improve thermal contact.

The sample was aligned by making use of the large magnetoresistance effect, following the technique developed by Soule (1958a). By this means the sample was aligned along the axis parallel to the current flow to within $\pm 1^{\circ}$. Alignment of the sample perpendicular to this was carried out when fitting the sample into the holder. Since this was achieved by lining up the sample parallel to the axis of the holder by eye, the accuracy was limited to 3° which included misalignment of the holder in the cryostat.

The cryostat could then be evacuated, and the whole apparatus allowed to attain equilibrium. To increase the thermal mass at room temperatures and above, the dewar of the cryostat system was filled with water or ice. This cut down to a minimum any drifting of the temperature, especially during the measurement of the thermomagnetic effects.

2.3.5. Measurement of the Galvanomagnetic Coefficients

The current through the sample was supplied by a 2 volt accumulator, and was controlled by three wire wound rheostats in a series-parallel arrangement. A rough

indication of the value of the current was given by a 0-1000 milliammeter. During measurements however, the current was set to within one part in 10^4 before every reading by comparing the potential difference across a one ohm sub-standard resistance with the required value, usually 100 millivolts, set on the potentiometer. After the initial drift on first switching on, the drift between readings was less than one part in 10^4. Thus the error in the current may be neglected.

To eliminate stray e.m.f.'s such as those due to the thermomagnetic effects, readings were taken with both the current and the magnetic field reversed. The resistivity was the mean of two readings I+ and I- and the Hall and Ettingshausen coefficients and the magnetoresistance, the mean of four readings (I+B+, I+B-, I-B-, I-B+.). This technique, however, did not eliminate contributions to these readings from the Ettingshausen effect due to the adiabatic conditions round the sample. The Ettingshausen coefficient was to be measured, if it was detectable, and the adiabatic coefficients corrected. If the Ettingshausen effects could not be detected, then this correction could be neglected. This can be seen by considering the Hall coefficient. From Equations 2.15 of Part I it can be shown that

$$V_H^a = V_H^i + \alpha \Delta T_E \qquad\qquad \underline{2.1.}$$

where the V's are the measured potential differences and ΔT_E

the temperature difference across the sample due to the Ettingshausen effect.

Now the Hall coefficient in graphite is of the order of 5×10^{-8} m^3/coulomb, (Soule 1958a), while the Seebeck coefficient, α, is of the order of 10 microvolts, (Blackman, Ubbelohde and Saunders 1961). The change in α in a magnetic field is neglected. Thus with a current of 0.1 A through a typical sample of dimensions $25 \times 3 \times 0.2$ mm^3 in a magnetic induction of 1.0 W/m^2, the potential difference across the sample due to the Hall effect would be 25 micro-volts. For $\alpha \triangle T_E$ to be 5 percent of this, $\triangle T_E$ would need to be 0.125°K or 2 microvolts on the thermocouples at their least sensitivity. This can easily be detected on the potentiometer.

The Nernst coefficient (the change in Peltier coefficient in a magnetic field) was not measured.

2.3.6. <u>Measurement of the Thermomagnetic Coefficients</u>

The current through the small heater used to establish the temperature gradients necessary for these effects was supplied by the arrangement employed for the current in the galvanomagnetic effects. The change was made by switching leads at the terminal strip mentioned in section 2.2.3. The milliammeter in the circuit now gave an indication of the power being supplied to the heater, assuming its resistance was independent of temper-

ature. Occasionally the voltage was increased to 6 volts,
in order to establish more easily measured temperature
gradients in some of the samples which had particularly high
thermal conductivities (30 watts/^{o}K cm in the best samples).

Establishment of the temperature gradient was a
tricky problem. In some samples the thermal conductivity
was greater than that of copper and the application of a
small quantity of power at the top of the sample merely raised
the ambient temperature without providing temperature gradient.
Thus it was difficult to keep the temperature low and have
a reasonable temperature gradient at the same time. In
addition the corrections applied to the gradients because
of the thermocouples were of the same order of magnitude as
the temperature gradients themselves which made the error
in these coefficients at the lowest temperatures large.

The high thermal conductivity meant that the technique
of reversing the temperature gradient could not be used. Since
this technique relies on no heat sink being necessary, only
materials with poor thermal conductivities can be used.

The transverse Nernst-Ettingshausen effect was large,
and the potential differences normally measured were greater
than 5 microvolts. However, when determining the magnetic
field dependence for this coefficient, special precautions
were necessary at the lowest fields. These consisted of
checking the zero error due to the galvanometer, by making
use of the reversing switch on the potentiometer. Any stray

e.m.f. in the leads themselves were eliminated by reversing

the magnetic field and taking the mean of the two readings.

This technique could not be used for the longitudinal Nernst-

Ettingshausen effect in zero magnetic field (the Seebeck effect)

for which further precautions were generally necessary. For

this measurement the potential difference along the sample

for zero temperature gradient was measured at the same time

as the correction to the thermocouples was determined. This

was then applied as a correction to the potential difference

measured when there was a gradient. To eliminate drift this

correction was also determined after the readings.

The Righi-Leduc coefficient was to be determined if

detectable by noting the change in temperature on switching

on and reversing the magnetic field.

2.3.7.   Low Temperature Techniques

For temperatures below room temperatures the cryogenic

liquids mentioned in section 2.2.4. were employed. The minimum

temperature normally attained in the sample holder was 82^OK.

Temperatures below this could be reached by pumping on the

liquid nitrogen, as discussed in section 2.2.4. With this

technique the minimum temperature attained was 68^OK. However,

the instability of the temperature proved to be too great and

this technique was not used very often. Temperatures above 82°K and 200°K were reached by driving the main heater from the D.C. supply of 24 volts. As nearly 40 watts were required to cover the two ranges 80 - 200°K and 200 - 275°K this heater frequently burned out. It was found that the best material for this was 40 s.w.g. Kanthal wire sleeved in Refrasil and potted in Araldite. The araldite had to be thermoset by passing a small current through the heater before it would take the high powers developed inside the heater. The wire was wound non-inductively.

In order to measure the thermomagnetic effects at temperatures in these ranges two methods were used. Either the temperature gradient could be kept constant and the ambient temperature increased by means of the main heater, or the ambient temperature could be increased by increasing the temperature gradient. A combination of both was used as a check on the reliability of the thermocouples, by taking readings with different temperature gradients about a mean temperature. The checking of the thermocouples discussed in section 2.3.2. and of the stray e.m.f.'s mentioned in section 2.3.6. was carried out each time the ambient temperature was changed by the main heater.

2.3.8. Errors

In this section the total error in the measurements is

discussed. It is assumed that the error in the current for the galvanomagnetic coefficients can be neglected.

In all the coefficients the errors arise from the error in:- The magnetic field; the dimension; and the measurements of the potential differences, either the output of the thermocouples or from the effects.

Except when the potential difference was less than 20 microvolts, the error in the latter factor was less than 2 percent. For the very small potential differences the uncertainty was limited to 3 or 5 percent by the special pre-cautions mentioned above. When the potential difference was greater than 100 microvolts the error was less than 0.5 percent and could be ignored, except when the difference of two readings was required.

For those measurements made at a constant value of the magnetic induction the error in this factor was less than 0.5 percent. When the value of the magnetic induction was less than 0.1 W/m^2, then the uncertainty became much larger, of the order of 10 percent at a value of 0.026 W/m^2, which was the lowest value obtainable. This decreased in proportion as the field was increased above 0.1 W/m^2.

The error in the dimensions was generally large. The probe separation was indeterminate to never less than 5 percent while the inaccuracy in the determination of the thickness was of the order of 2 percent. The error in the width of the

sample was less than 0.5 percent, and could be ignored.

The absolute value of the resistivity could be only determined to within ± 7 percent. The Hall coefficient could be determined to within ± 3 percent for those values determined at a constant field, and to within ± 13 percent at the lowest fields, errors at intermediate fields being less than the latter value. The magnetoresistance, being obtained from the ratio of two voltages, was perhaps the most accurate of all. The error was less than 1 percent for all samples except those with a magnetoresistance of less than 1 percent. For these the difference in $V_c(B)$ and $V_c(0)$, where the V_c's are the potential differences across the conductivity probes in and out a magnetic field, was of the order of a few microvolts, and the error was accordingly much larger, generally being about 5 percent.

The error in the parameters determined from these effects varies with the effect. The average mobility for most samples will be indeterminate to within ± 0.5 percent, this being the error in the magnetic field. The error in the zero field value however will be larger than this because of the process of reading from a graph. It is expected that this process will not give an error greater than 2 or 3 percent. Since the total number of carriers involves the absolute value of the resistivity, the inaccuracy in this parameter will be never less than 7 percent. This will not affect the value of

b, the ratio of mobilities very much since it is very insensitive to changes in n or R_h, the Hall coefficient. Although the total error in $R_h n_e$ was never less than 10 percent this made the inaccuracy in b less than 2 percent.

The greatest uncertainty in the thermomagnetic effects lay in the determination of the temperature gradients. For those temperatures at which temperature gradients of the order of a degree per centimetre could be maintained, the error in the gradients was about 2 percent. For those temperatures at which the corrections were important, the uncertainty was very large, being of the order of 25 percent. This could be reduced a little by investigating the dependence of the effects on the magnitude of the gradient, as discussed in section 2.3.7., but rarely did this reduce the error to below 5 percent.

In addition to these errors the transverse Nernst-Ettingshausen coefficient had the uncertainty inherent in the measurement of the probe separation. The combination of these two large errors meant that the total error in this coefficient at the temperatures discussed above was never less than 20-25 percent. For all other temperatures the error was less than this and was of the order of 8 percent. In the longitudinal Nernst-Ettingshausen in zero magnetic field (the Seebeck coefficient) an additional error was introduced in the measurement of the small potential differences. Since this was never less than 3 percent, the uncertainty in this coefficient varied between 5 percent and 25 percent.

PART III

RESULTS.

CHAPTER I

Theoretical

3.1.1. Introduction

In the last chapter of part I, the programme for
the computer was described. The range of values given to the
parameters used in the programme will now be discussed.

The reduced energy overlap E_g^* is inversely proportional
to temperature. Therefore to find the variation of the co-
efficients with temperature, E_g^* was allowed to range over the
values - 10 to 0. Positive values of E_g^* (0 to 10), corresponding
to a band gap, were also substituted in the programme in order
to provide a complete basis for comparison of the experimental
data with the theory. In addition, for large positive E_g^*,
that is, the non-degenerate region, simple expressions can be
derived for the coefficients. Therefore a check on the
accuracy of the computation was available.

Since the programme running time was originally
approximately 4 hours, it was essential to minimise the overall
length of the programme. This was achieved by restricting
b, the ratio of mobilities, to only two values 1.0 and 1.1,
restricting the reduced Fermi level E_f^* to one half of the
overlap. In addition the number of values of μB in that loop
was cut to a minimum as the early programmes indicated that
the coefficients varied smoothly with this parameter. With
all these adjustments, the running time was cut down to just

under two hours.

However, in the programme, E_f^* is set equal to minus a fraction of E_g^*. In the Fermi level loop the computer compares the current value of E_f^* with the maximum before going on to the next value. With zero energy gap this implies a comparison of a negative zero with a positive zero. The result is that the computer cannot get out of the loop and performs the calculation for only one value of E_f^*. Thus a special programme is necessary for the case of zero energy gap. In this particular programme, E_f^* was given the values -2.0, -1.0, -0.5, 0.0, 0.5, 1.0, 2.0, to check the variation of the calculated coefficients with the Fermi level through the intrinsic state. The programme was also run through with an additional value of b of 0.9 to investigate the variation with b less than one.

One point which must be emphasized concerning this programme is that it assumes that the position of the Fermi level is independent of the value of the ratio of the densities of the carriers. However, physically these two parameters are related through the equation:-

$$a = \frac{n_1}{n_2} = \left(\frac{m_1}{m_2}\right)^{3/2} \frac{F_{1/2}(E_{f_1}^*)}{F_{1/2}(E_{f_2}^*)} \qquad \underline{1.1.}$$

Inclusion of this expression would have made the

programme prohibitively long,

The results of the computer are printed out in the
form of long tables. It would be impossible to give all
the results in this thesis. Here the computer 'print out'
is summarised by plotting the graphs of the coefficients as
functions of the various parameters.

The results for the transverse Nernst-Ettingshausen
coefficient will now be examined.

3.1.2. The Transverse Nernst-Ettingshausen Coefficient or Q^t

The transverse Nernst-Ettingshausen coefficient is
also known in the literature as the Nernst coefficient.
Historically, however, the Nernst effect is the variation
of the Peltier coefficient with magnetic field $\pi(B)$[*]. Since
this ambiguity of notations can easily cause confusion,
the first notation or more simply Q^t will be employed in
this thesis.

Q' is defined by equation

$$Q^t = Q' \frac{k}{e} \frac{1}{\mu_2} = Q^i_{12} \qquad\qquad \underline{1.2.}$$

and is the actual number calculated by the computer.

The variation of Q' with E_g[*] is shown in figure 17
for the two regions of magnetic induction $\mu B \ll 1$, evaluated
at $\mu B = 0$, and $\mu B \gg 1$, evaluated at $\mu B = 13.3$. The crosses
on the former curve are those computed with the early

[*] See Campbell 1923 for review of early work.

FIGURE 17

THE VARIATION OF Q' WITH ENERGY
GAP FOR : $E_f = 0.5E_G$.
         $a = 1.0$
         $b = 1.1$

$Q = Q' \dfrac{te}{k} \dfrac{1}{\mu}$

$\mu^o B \ll 1$

$\mu^o B \gg 1$

nondegenerate lines

-8.0
-7.0
-6.0
-5.0
-4.0
-3.0
-1.0

THE VARIATION OF Q' WITH ENERGY
GAP FOR : Ef = 0.5Eg ,
a = 1.0
b = 1.1

$Q = Q' \dfrac{e}{k} \dfrac{1}{\mu}$

nondegenerate lines

$\mu^{o}B \gg 1$

$\mu^{o}B \ll 1$

Eg/kT
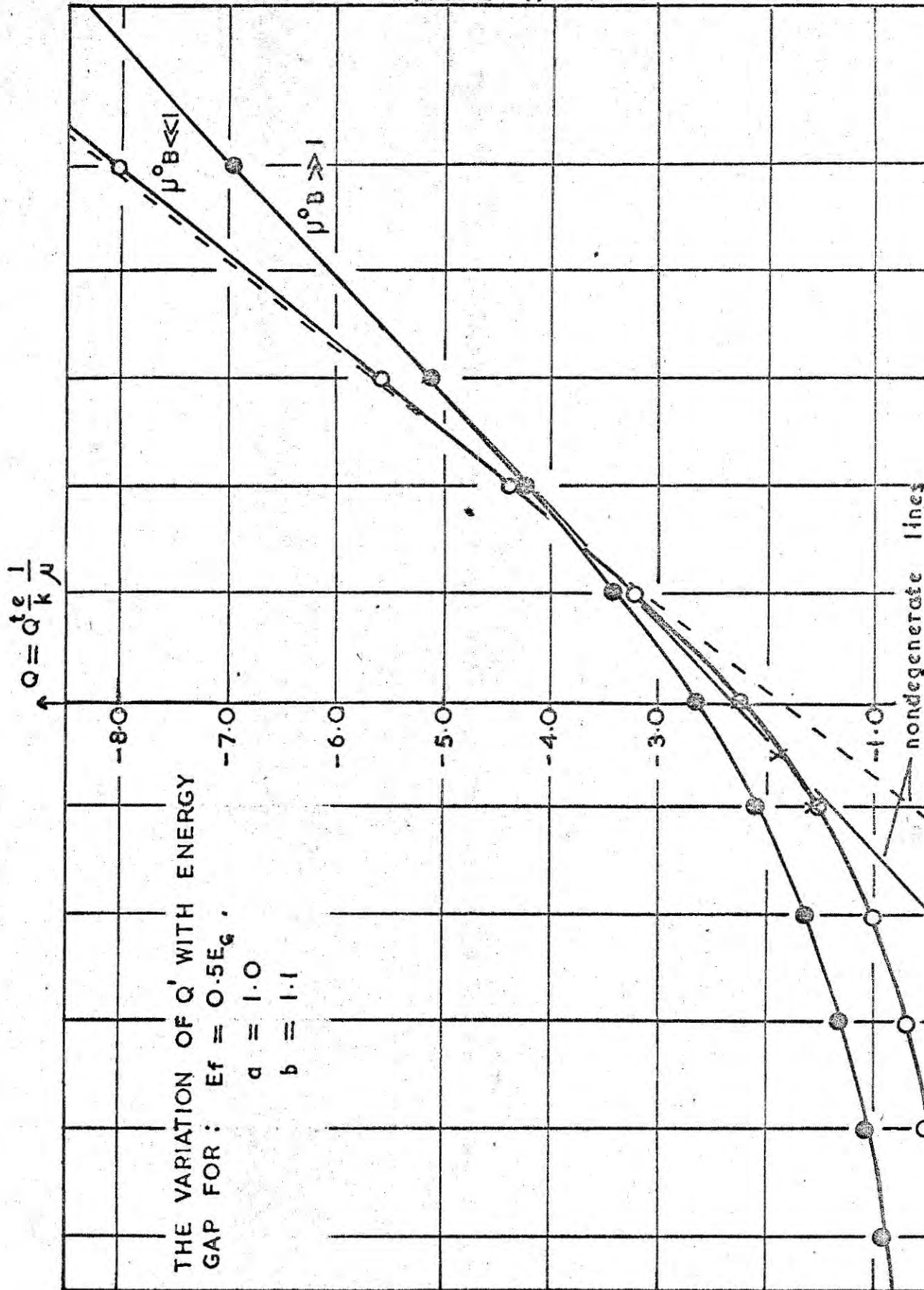
FIGURE 17

programme mentioned in section 1.4.5. The two straight
lines were calculated by hand from the equations for the
region of classical statistics with $n_1 = n_2 = n$.

$\mu B \ll 1$)
$$Q'_6 = P \ \frac{1 + b^3 - b(1 + b)(7 + 2Eg)}{(1 + b)^2}$$

$\mu B \gg 1$)
$$Q'_{\infty} = R \ \frac{b}{(1 + b)} \quad (4 + Eg) \qquad (R \ \text{is negative})$$

where P and R are constants.

It will be noted that whereas for negative $E_g{}^*$, Q'
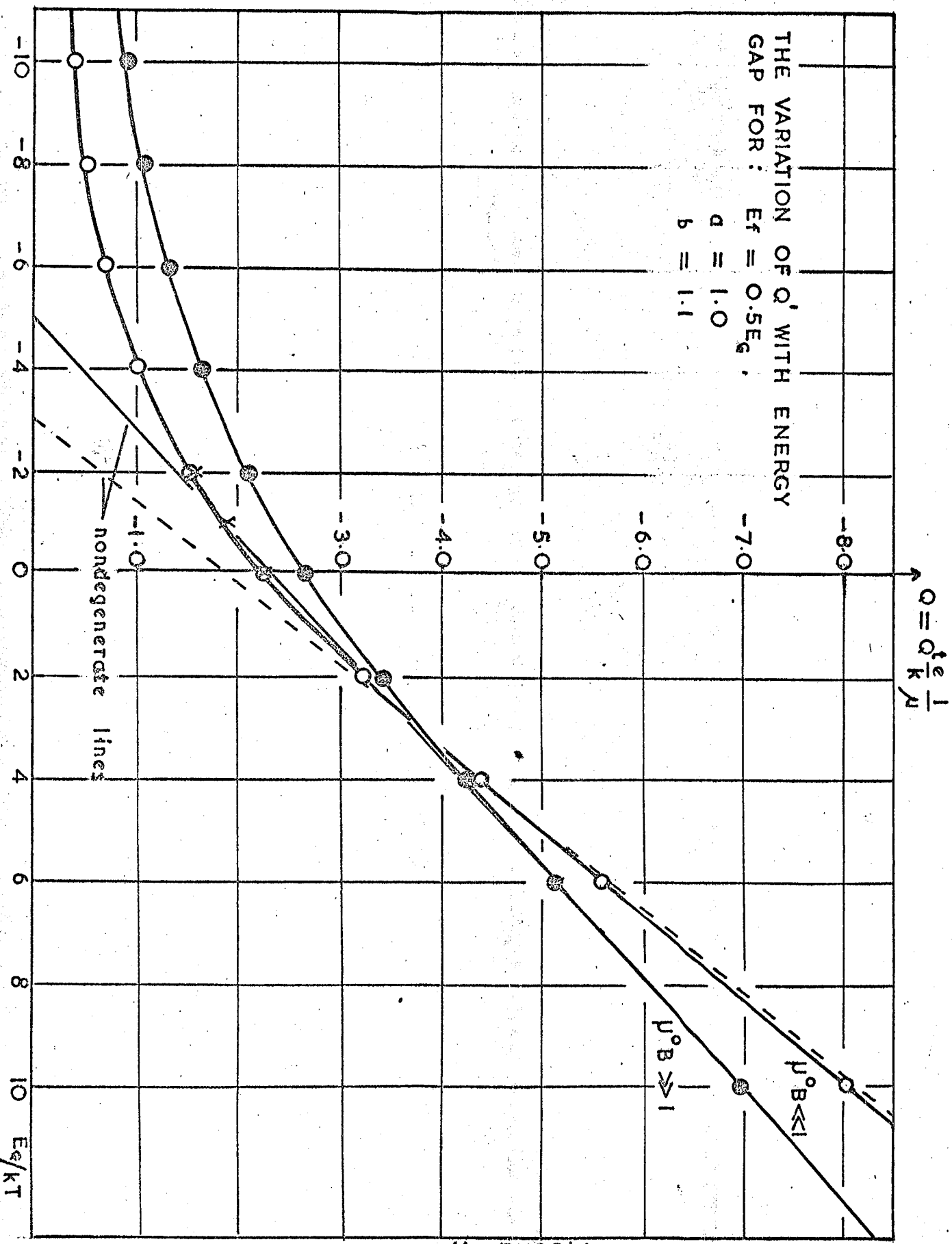increases on increasing the magnetic induction, for positive $E_g{}^*$
greater than 3, Q' decreases. This is shown more completely
in figure 18 which shows Q' as a function of μB for various
energy gaps and overlaps. For each value of $E_g{}^*$, the results
are plotted for two values of $E_f{}^*$; $E_f{}^*$ at the centre of the
overlap and one other value. From this graph it can be seen
that Q' is sensitive to the Fermi level at high values of
magnetic induction.

In addition figure 18 shows that the conditions for
the low and high magnetic induction regions are given by
$\mu B \ll 0.15$ and $\mu B \gg 8.0$. The former agrees with the conditions
for the lower induction region obtained from the mobility
measurements. To indicate how this coefficient varies with
the position of the Fermi level and the ratio of the carrier
densities, graphs of Q' against $E_f{}^*$ for the three values of

FIGURE 18

VARIATION OF Q WITH μB FOR VARIOUS ENERGY GAPS
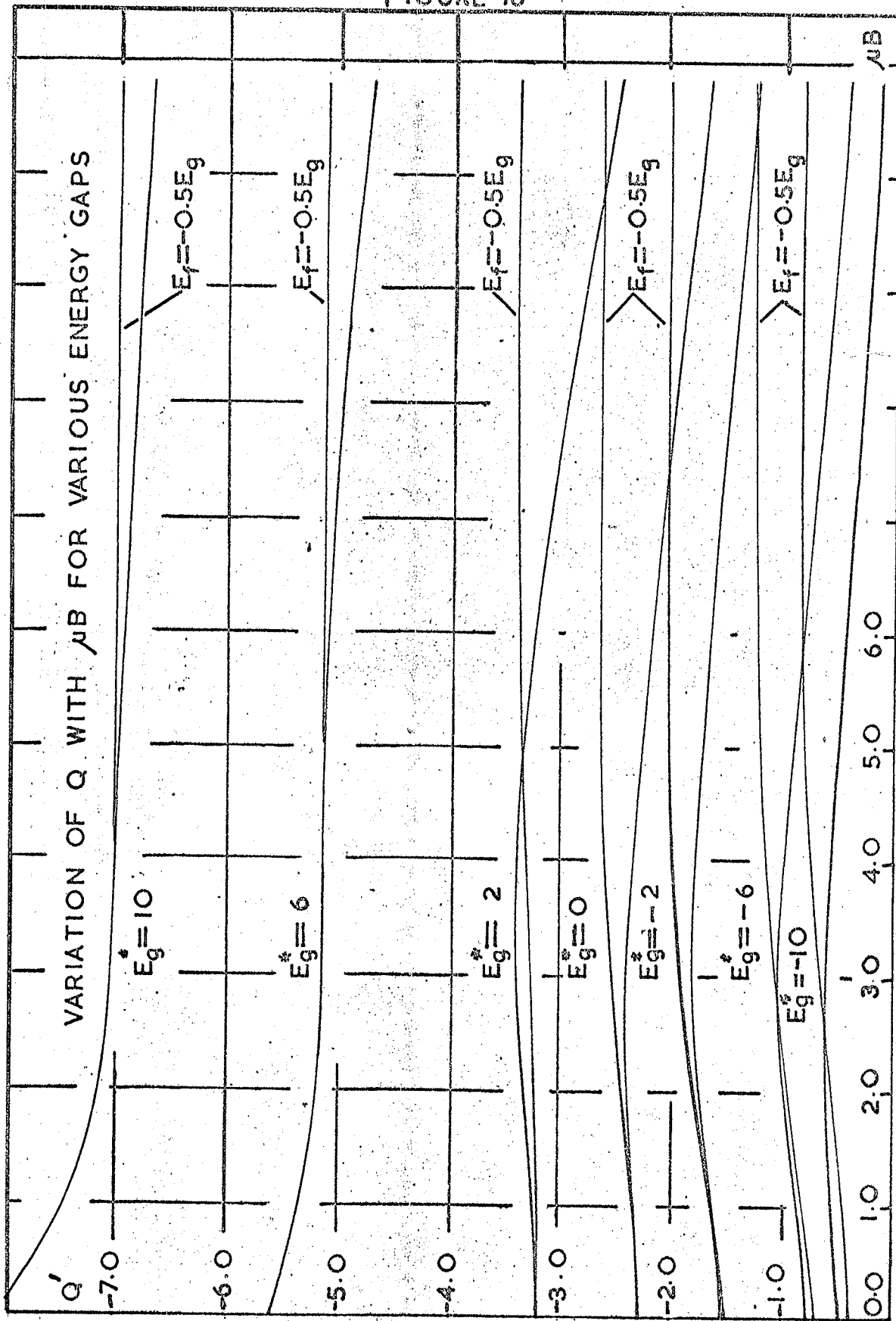
FIGURE 18

a are given in figure 19 for E_g^* = O. The sensitivity of
Q' to these parameters becomes even more apparent in these
graphs. However care must be exercised in the interpretation
because of equation 1.1.

The variation of Q^t with b and E_f^* is shown in
figure 20, for zero energy gap only. There is a similar
variation with b and a for other energy gaps and overlaps.
All of these curves can be employed to provide graphs of Q^t
against μB for various intermediate values of E_f.

If a particular value of energy gap or overlap is
chosen, then the temperature dependence of this coefficient
can be deduced from figure 17 by following the curve, since
as the temperature decreases E_g^* increases. This is shown
for the two regions of magnetic induction $\mu B \ll 1$ and $\mu B \gg 1$
in figure 21. In this graph, the curves show the expected
temperature variation of Q^t for various overlaps including the
theoretical value of 0.032 eV, a and b are assumed constant.

Figure 22 shows a similar curve for an arbitrary
energy gap. In an attempt to trace the temperature variation
of Q^t down to very low temperatures the programme was used to
compute Q^t for large negative values of E_g^*. Unfortunately
for E_g^* less than -25, Q^t became positive and increased linearly
with decreasing E_g^*. This is impossible since at 0^OK all
thermomagnetic effects are zero. This discrepancy results
from the integrations.

The integrand contains a term $e^{-E_g^*}$. For large

FIGURE 19

VARIATION OF Q' WITH FERMI LEVEL FOR VARIOUS VALUES OF a AND μB
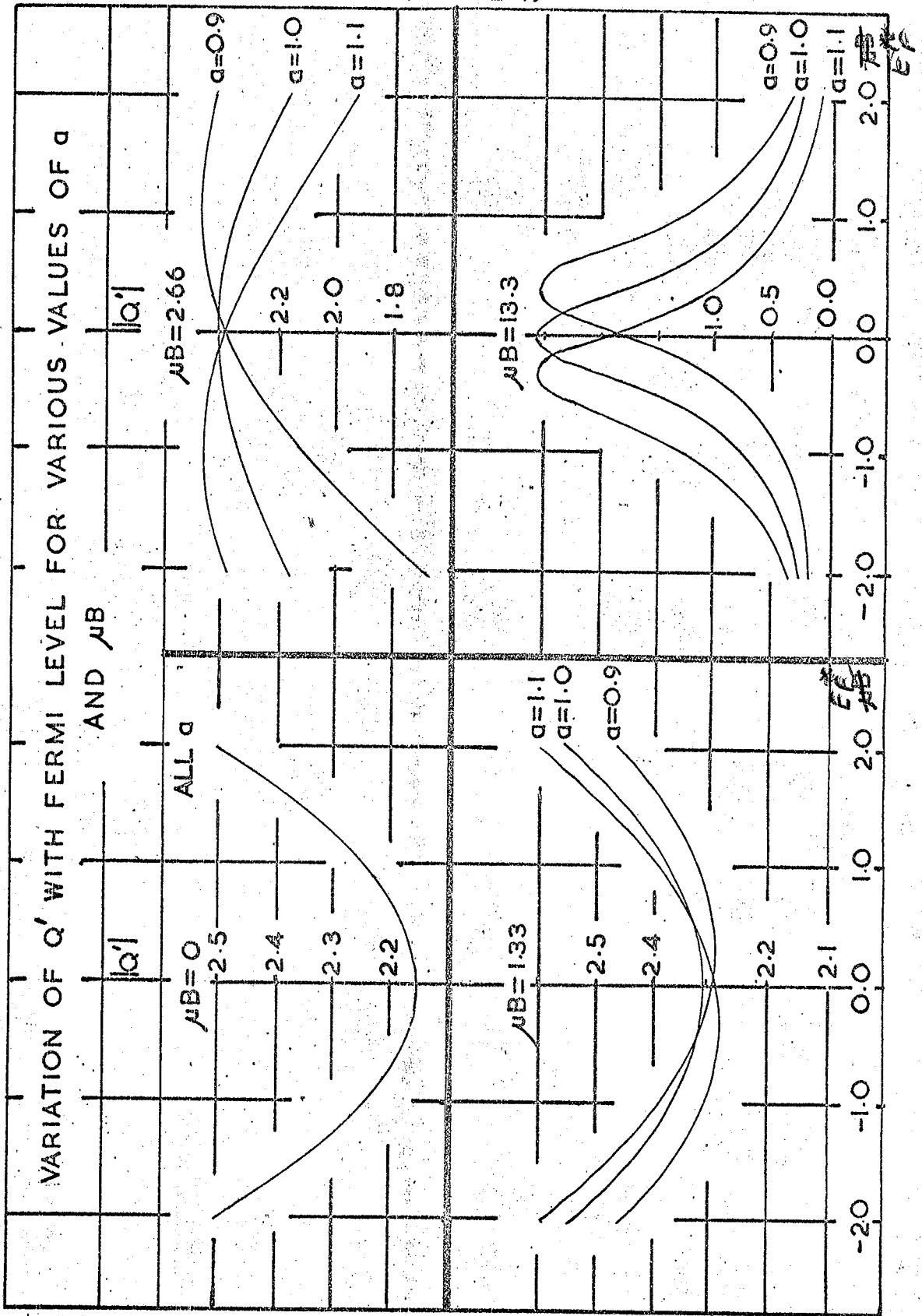
negative E_g^* this term will become very large, greater than 10^5. Thus, the accuracy of these large numbers will become such that the difference between two similar integrations could change sign. The low field expression for Q^t is the difference of two products, each a sum and a difference of two of the integrations.

Figures 17 to 22 can now be used in one of several ways. This will be discussed later after the discussion of the theoretical results for the longitudinal Nernst-Ettingshausen coefficient $\alpha(B)$.

3.1.3. The Longitudinal Nernst-Ettingshausen Coefficient ($\alpha(B)$)

Other names for the longitudinal Nernst-Ettingshausen effect are the magneto-Seebeck effect or the magnetothermo-electric effect. The value in zero magnetic induction is known as the Seebeck coefficient or the thermoelectric power $\alpha(0)$. In this thesis it will be known as the Seebeck coefficient in zero magnetic induction and as $\alpha(B)$ for the value in a magnetic induction. $\alpha^*(B)$ is defined by $\alpha(B) = k/e \; \alpha^*(B)$. The variation of $\alpha^*(0)$ and $\alpha'(B)$ for large magnetic fields with E_g^* is shown in figure 23. As will be shown later the latter curve has very little meaning since the coefficient is very sensitive to the electronic parameters. It is included for comparison with the transverse Nernst-Ettingshausen coefficient. There is no crossing over of the two lines in this case. The straight line

FIGURE 23

VARIATION OF $\alpha'(B)$ WITH ENERGY GAP.

$a=1.0$ $b=1.1$ $E_f=-0.5E_g$

$\mu B\ll 1$

$\mu B\gg 1$

$\alpha'(B)$

FIGURE 23
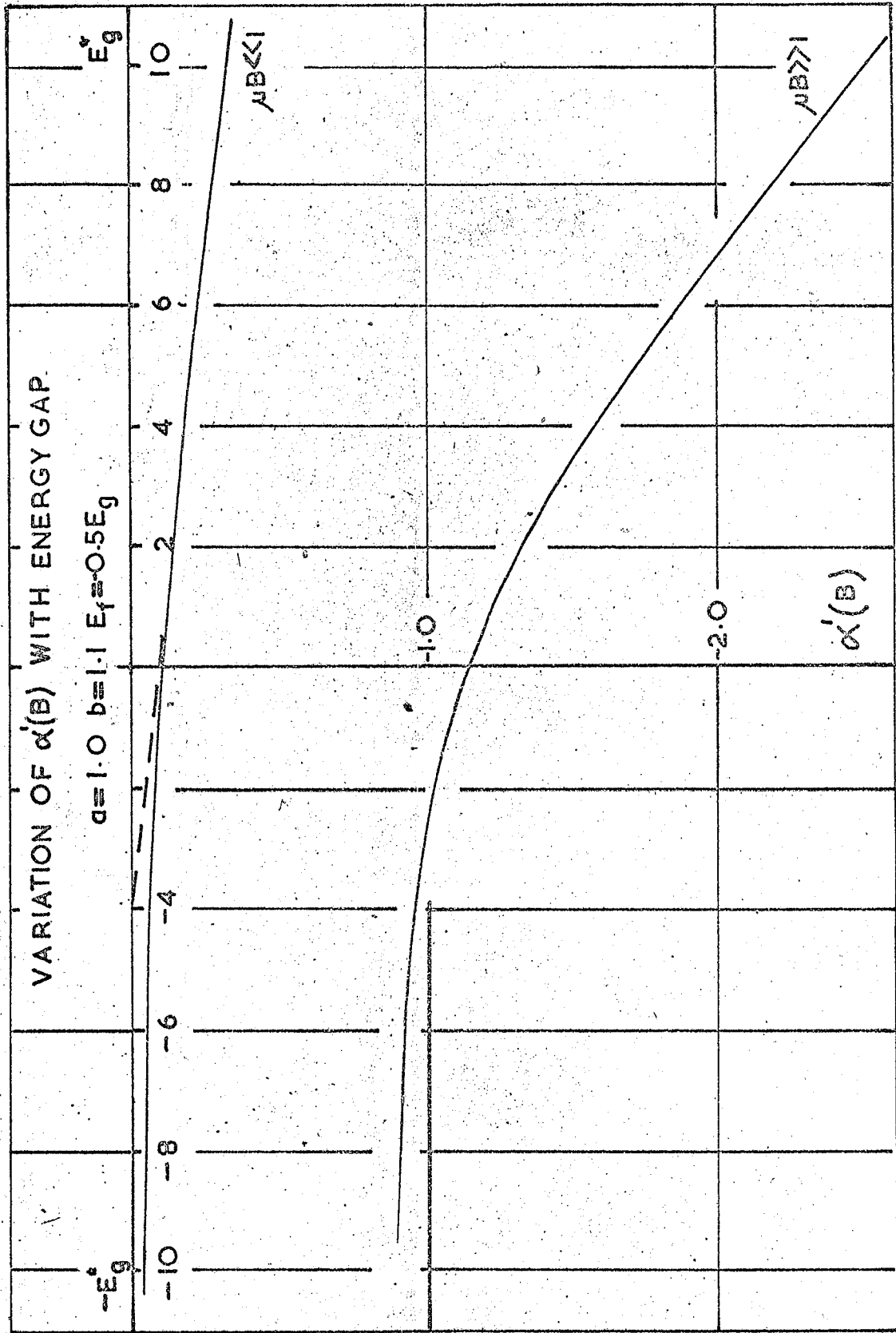
is calculated by hand from the expression $\alpha(0) = \dfrac{\alpha_1 \sigma_1 + \alpha_2 \sigma_2}{\sigma}$

for the classical region where the subscript refers to the ith carrier.

A rough check on the accuracy of this coefficient is provided by the calculated values for E_f in the centre of the overlap and a = b = 1. For this particular combination of parameters, no matter what overlap or magnetic field, $\alpha(B)$ should always be zero. This, in fact, is the case with all the results for this particular combination.

As figure 23 indicates, for intrinsic materials with large overlaps, the Seebeck coefficient is small, as expected. In this particular case it is negative since b, the ratio of the mobilities is 1.1, while E_f is in the centre of the overlap and a, the ratio of the densities is one. Since the variation of the values of $\alpha(0)$ with E_g^* is small in this region the variation of $\alpha'(B)$ with the other parameters for zero energy gap will be almost the same as for an overlap.

Figure 24 shows that for large values of μB, $\alpha'(B)$ becomes independent of μB for the case of an intrinsic material with large overlap. This is, of course, not true for any other case. Figures 25, 26, 27 show the variation of $\alpha'(B)$ with μB for various a, b and E_f^*. These curves indicate the extreme sensitivity of this effect to a, b, and E_f. Figure 28 is similar to figure 26 but is for b = 1.1 instead of 1.0. Symmetry would be expected in figures 25, 26, and 27, but the curves are not exactly symmetrical, indicating

FIGURE 24

VARIATION OF $\alpha'(B)$ WITH μB FOR VARIOUS ENERGY GAPS

$E_f = 0.5 E_g$ $a = 1.0$ $b = 1.1$

$E_g = 10$
$E_g = 4$
$E_g = 0$
$E_g = 4$
$E_g = 10$

$\alpha'(B)$

FIGURE 25

VARIATION OF $\alpha'(B)$ FOR $E_g = 0$ AND $a = 1.0$

FIGURE 26

VARIATION OF $\alpha'(B)$ FOR $E_g = 0$ AND $E_f = 0$

FIGURE 26

FIGURE 27

VARIATION OF $\alpha'(B)$ FOR $E_g = 0$ AND $b = 1.0$

FIGURE 28

VARIATION OF $\alpha'(B)$ FOR
$E_g = 0$ and $b = 1.1$

top curve $a = 0.9$
middle curve $a = 1.0$
bottom curve $a = 1.1$

$E_f^0 = 0.5$

$E_f^0 = 0.0$

$E_f^0 = -0.5$

$\alpha'(B)$
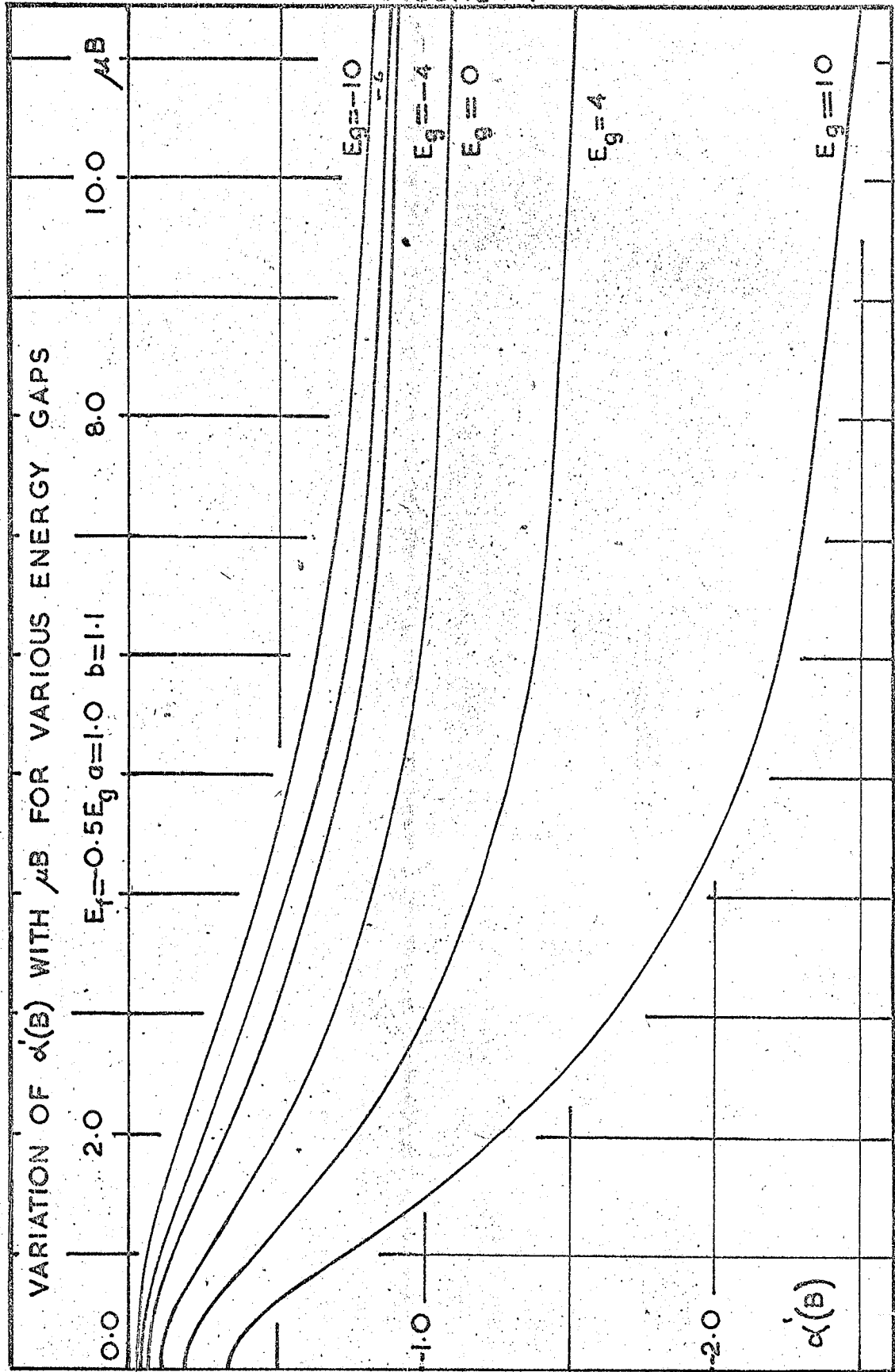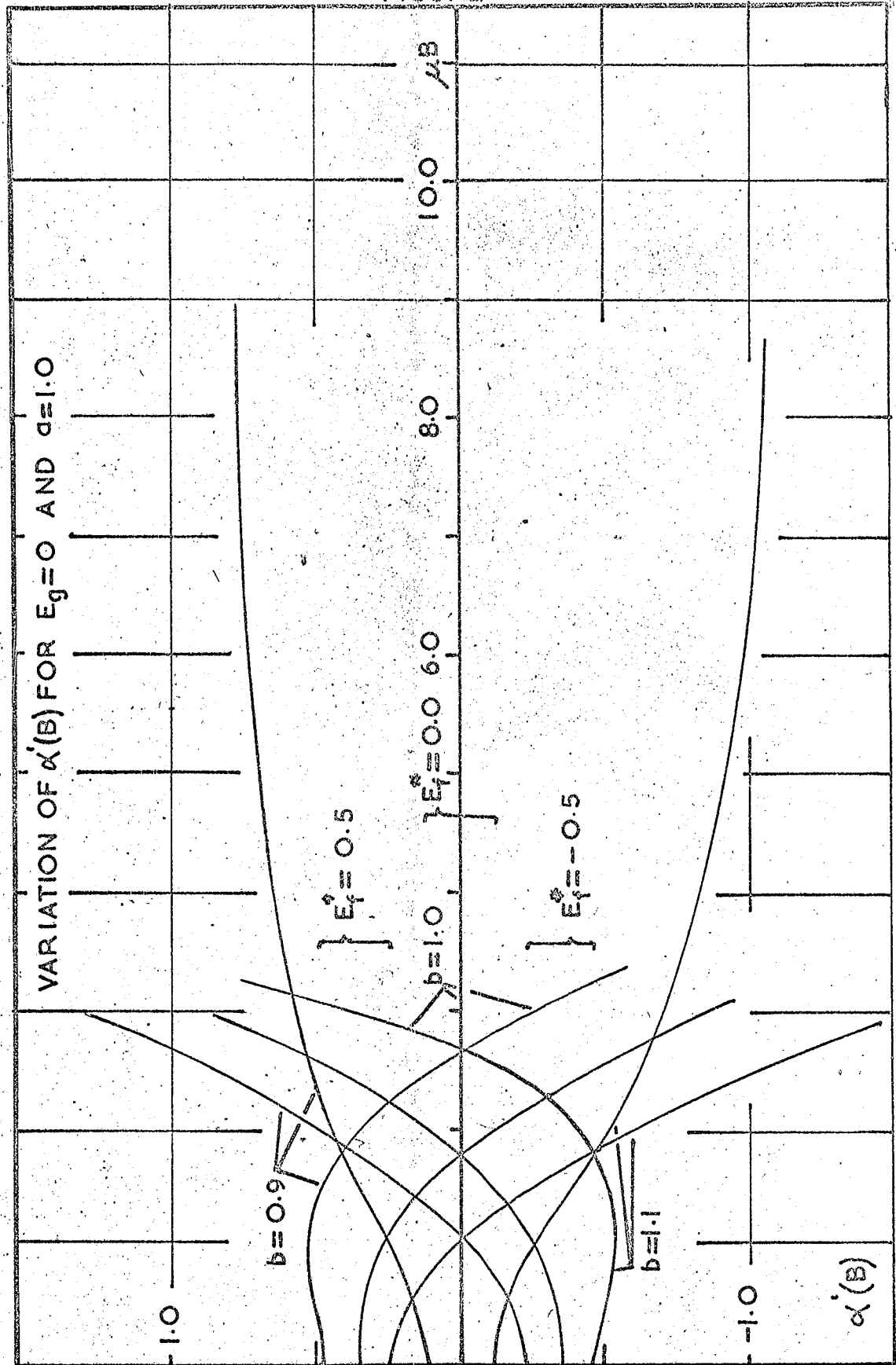
FIGURE 28

that there must be a small error in the programme. This error probably arises from the error in the integrations mentioned previously, but it is small enough to be neglected.

From these curves it can be deduced that values of $E_f = +0.5$, $b < 1$, and for $E_f = 0$, $a = 0.9$ cannot be correct since they give positive values of $\alpha(0)$.

Figures 29 and 30 show the variation of $\alpha'(B)$ with μB for $E_g = -4kT$ (corresponding to $E_g = 0.032$ eV at $95^{O}K$) for various a, b and E_f/kT. The curves in these figures are very similar in shape and magnitude to those in figures 25 to 27, indicating how insensitive $\alpha(B)$ is to the magnitude of the band overlap.

The dotted lines in figure 29 are the values of $\alpha(B)$ for $E_f = 1.2$ kT deduced by comparison with figure 28.
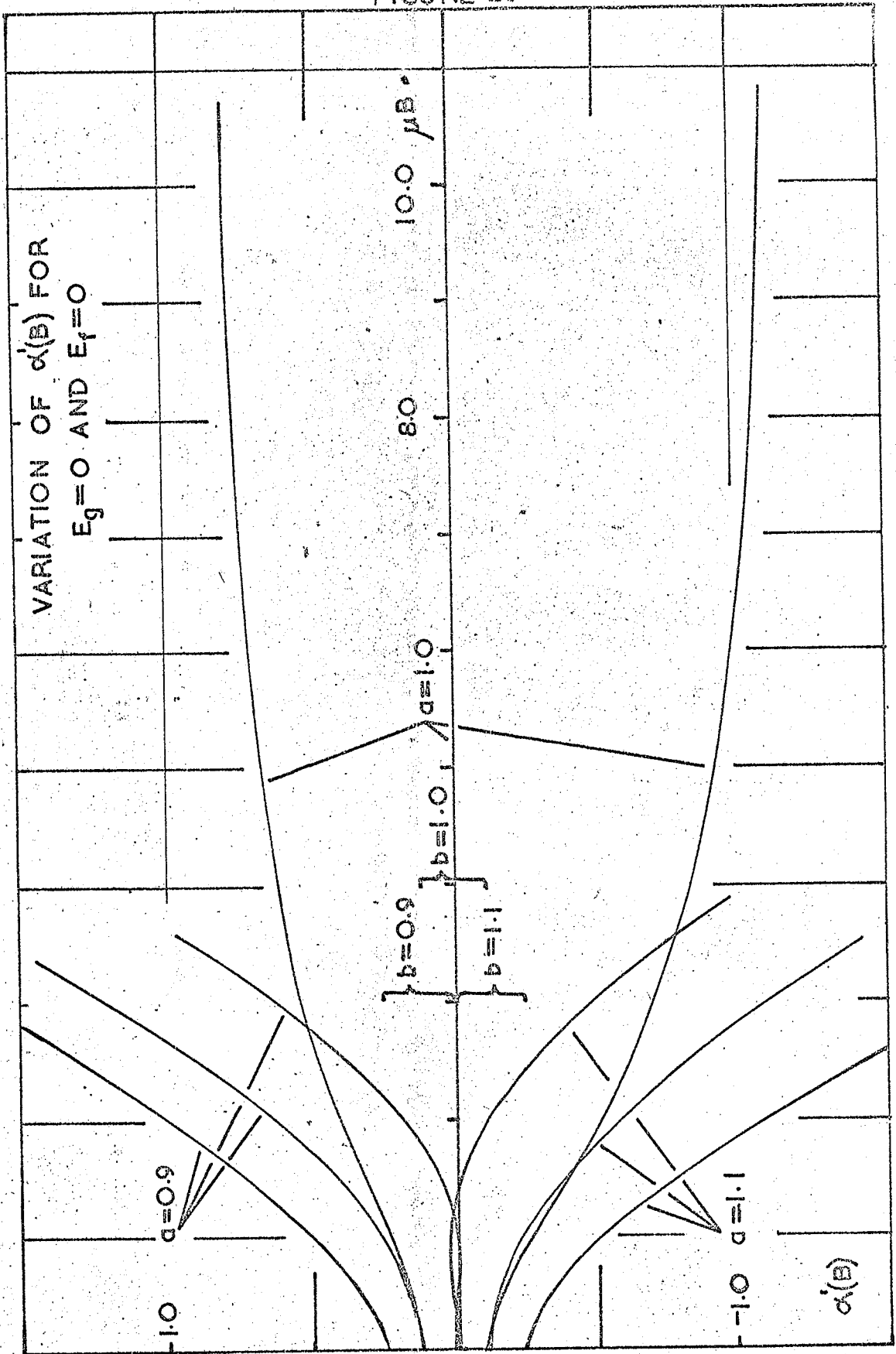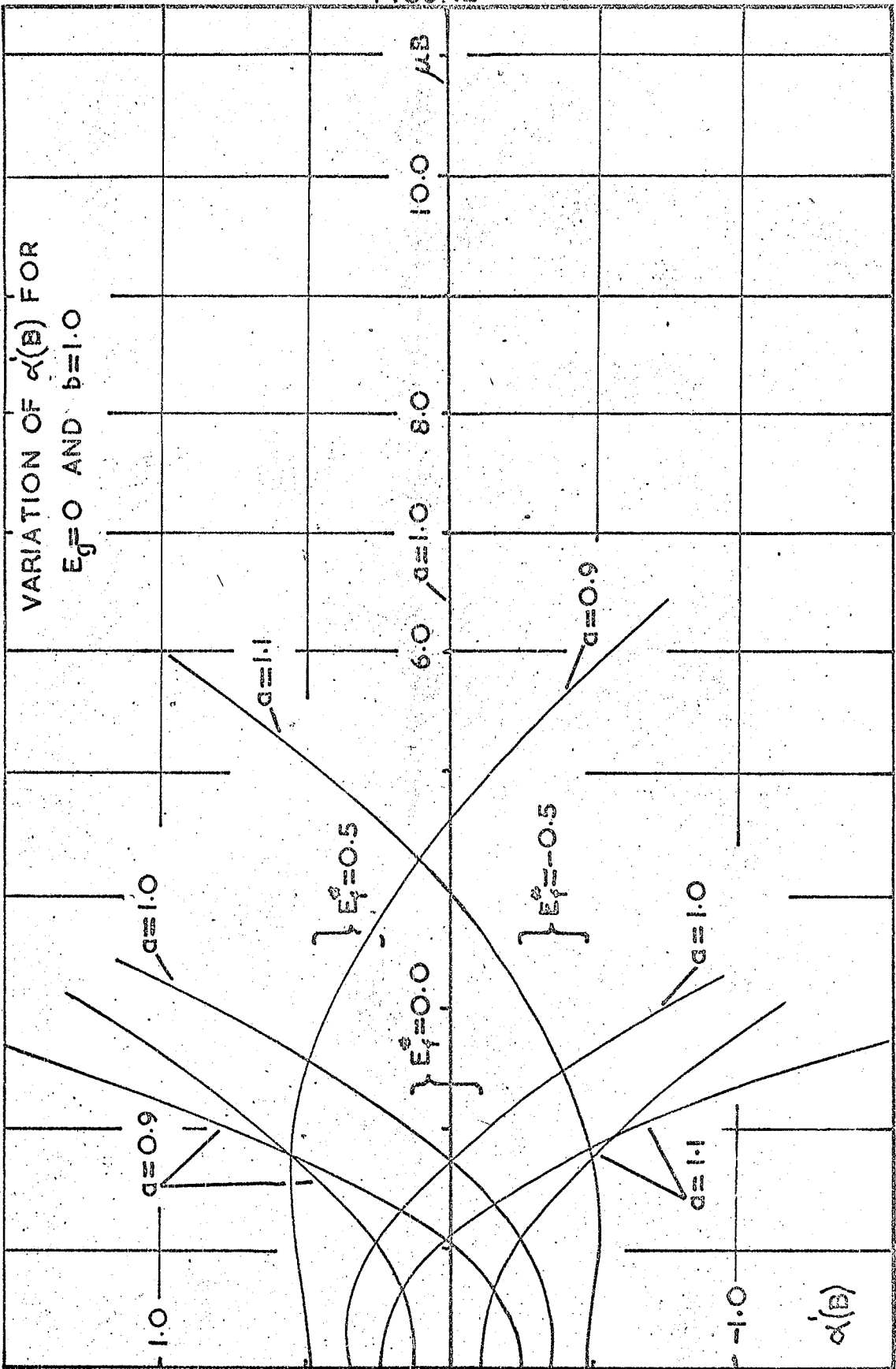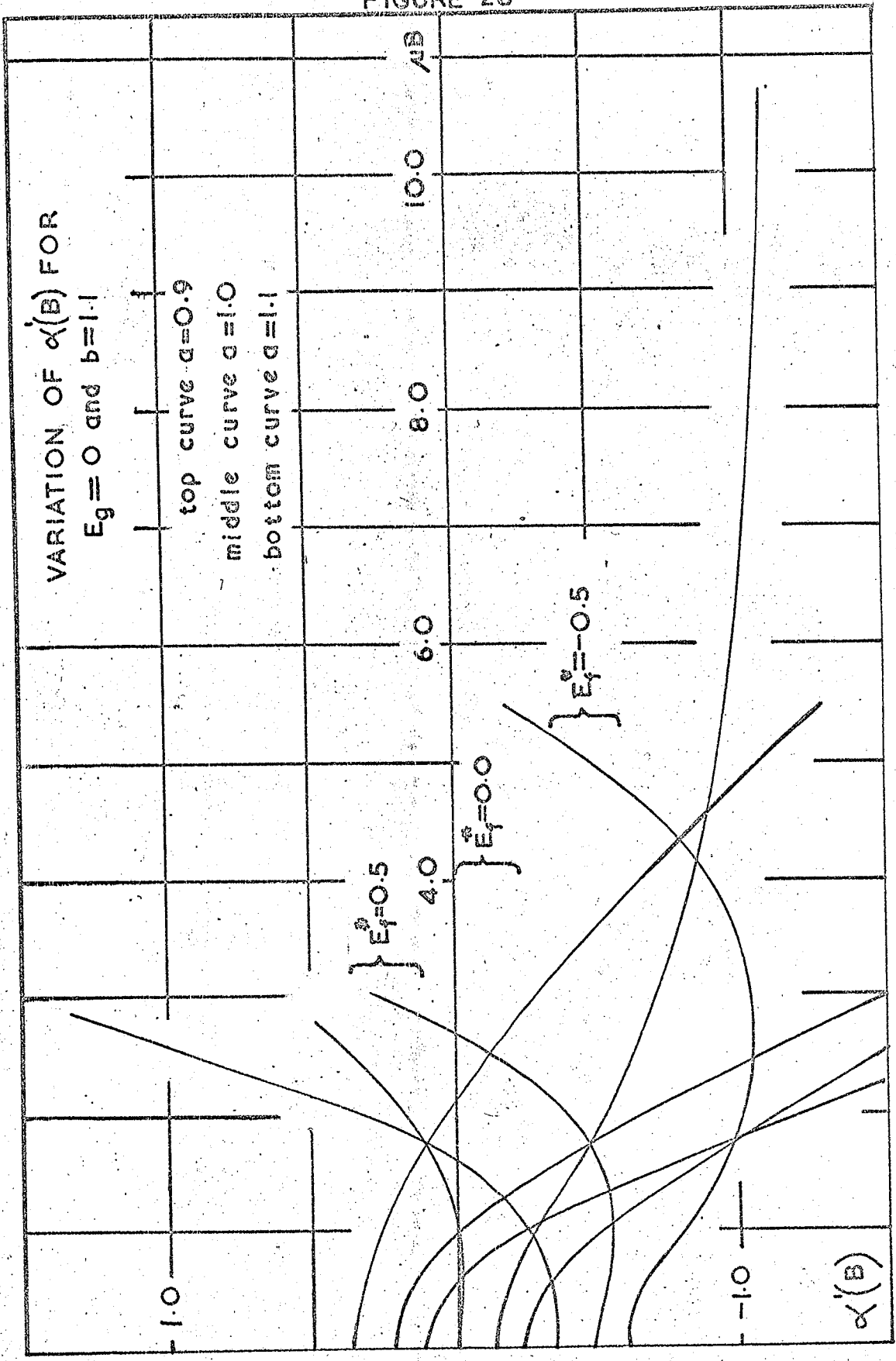
3.1.4. Correlation with Experiment

The results of the previous two sections can now be used in one of two ways; either to predict the measured values of the coefficients assuming values for E_g, E_f and a, using the values for b and μ_2 deduced from the galvanomagnetic effects, or, to compare the measured values of the coefficients with the curves in figures 17 to 30. Then values for E_g^*, E_f and a, can be deduced assuming that the values of b and μ_2 are given by the galvanomagnetic coefficients.

The latter course is perhaps the better to take since

FIGURE 29

VARIATION OF $\alpha'(B)$ FOR
$E_g = -4kT$ and $b = 1.1$

top curve $a = 0.9$
middle curve $a = 1.0$
bottom curve $a = 1.1$

$\} E_f^* = 2.8$

$\} E_f^* = 2.0$

$\} E_f^* = 1.2$

$\alpha'(B)$
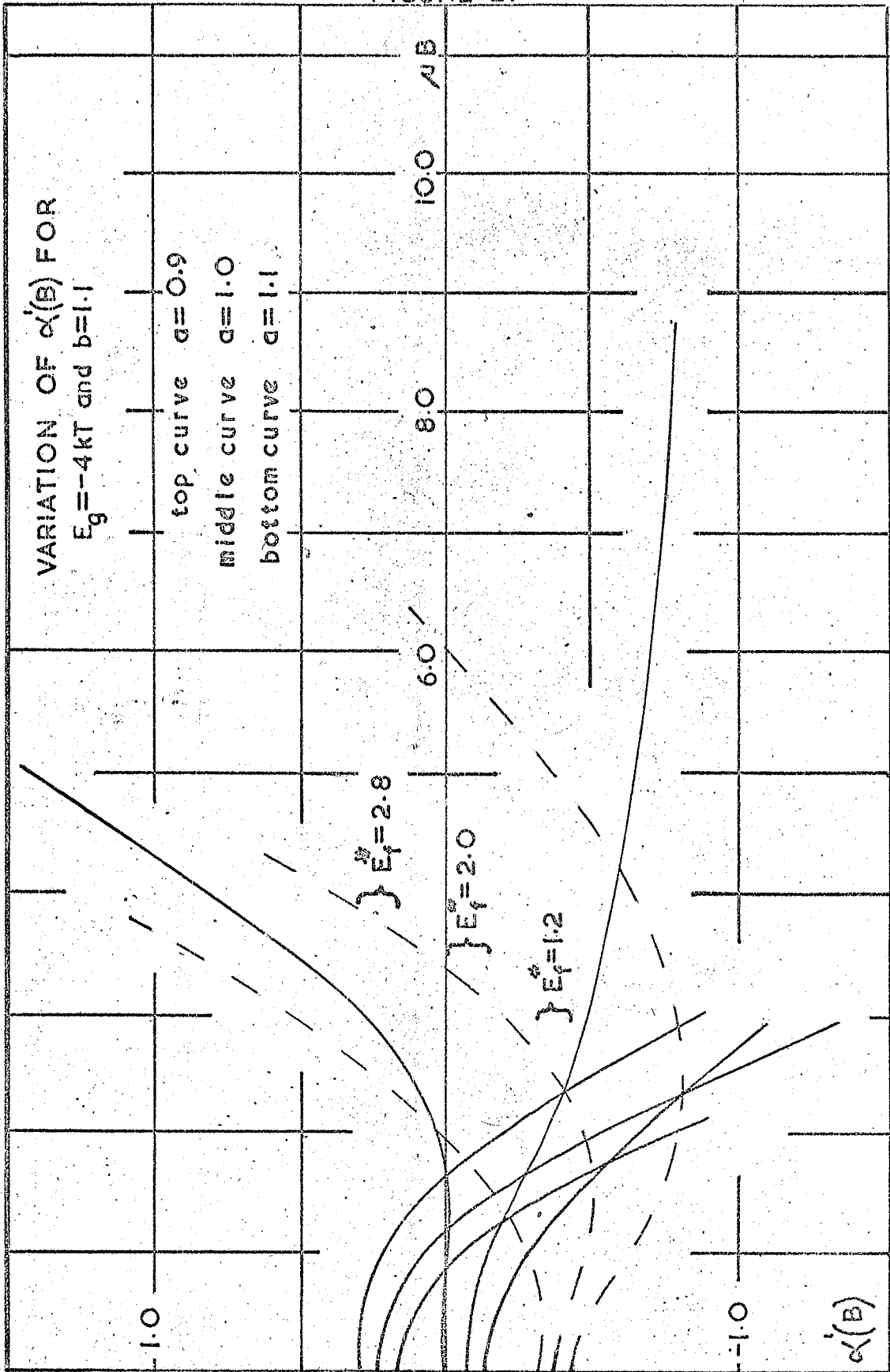
FIGURE 29

it is not certain that the values of the energy overlap and the position of the Fermi level will be the same in pyrolytic graphite as in single crystal graphite.

From the value of Q^l calculated from the measured Q^t and from figure 17, assuming in the first approximation that the material is intrinsic, $E_f^* = -0.5 \ E_g^*$ and b = 1.1, and a = 1, a value for the energy overlap can be deduced. This value can be checked at different temperatures. Knowing this value of E_g, the variation of the Q^t or Q^l with μB will give an indication of whether the sample is intrinsic or not.

This, however, is not a very sensitive test of the intrinsic condition and it would be difficult to deduce anything from this curve. It is apparent, however, from figures 25 to 28 that the variation of the longitudinal Nernst-Ettingshausen coefficient with μB is much more sensitive to departures from the intrinsic condition. Thus by comparing the measured variation of α^l(B) with μB, it should be possible to deduce values for E_f and a, and possibly to verify that the value of b is correct.

One advantage of using the longitudinal Nernst-Ettingshausen coefficient for this purpose is that it does not depend on either the carrier mobilities or the densities and so α^l(B) is measured directly. The Transverse Nernst-Ettingshausen coefficient, Q^t, must be reduced first of all by dividing by the hole mobility in order to compare Q^t with the theory.

Thus by comparing the experimental results with the theoretical results, it should be possible to obtain information on those electronic parameters not deduced from the galvanomagnetic coefficients.

In order to carry out this procedure it becomes necessary to assume that acoustic mode lattice scattering predominates. This is true for the better samples (see chapter 3.2. for definition) down to around 100°K when the crystallite boundary scattering begins to predominate. For the poorer samples the crystallite boundary scattering is likely to predominate until well above room temperatures. For these samples the theory will not be true. However, they will be very polycrystalline with poorly aligned crystallites. It is impossible to know exactly what is being measured in such a material especially with the large anisotropy ratio in graphite.

CHAPTER II

Experimental Results

3.2.1. Introduction

In this chapter the measurements on the galvanomagnetic effects are set out, discussed and compared with the available data on single crystals in order to assess the degree of perfection of the samples. The results are then employed to determine the electronic parameters of the samples. Knowing these parameters, other parameters can be deduced from the theoretical values of the thermomagnetic coefficients.

As mentioned previously (section 2.3.5.) all the measurements were made under adiabatic conditions. Attempts

ERRATA

Thus the error in assuming the isothermal and adiabatic coefficients are equivalent is less than one percent.

Measurements were made on the following samples:-

6B, 6E, 10C, 10D, 20A, 20B and 22B,C,D,F,G,H.

Samples 6B and E were measured while the apparatus was being developed and the data on these samples has therefore a larger error than the rest of the data.

3.2.2. The Resistivity and Magnetoresistance

The resistivity at $300^{\circ}K$ is given in table IV. Since the error in these data is large, the variation of resistivity with temperature is plotted as a relative resistivity ρ_T / ρ_{300}. This is shown in figure 31, for all the samples. The variation of ρ_T / ρ_{300} for Soule's specimen EP11 is also shown on this graph for comparison. The best samples 20A, B and 22B, C have room temperature values which lie in the range reported for single crystals $(40-60 \times 10^{-8}$ ohm m) (Primak and Fuchs 1954, Kinchin 1953 and Soule 1958). However none of the samples have resistivities at $80^{\circ}K$ which are comparable to the single crystal values at that temperature.

McClure (1958) has argued that from the position of 'break' in the resistivity versus temperature curve, band overlap may be deduced. The break in the present curves may, however, be a result of the imperfection of the samples. This possible measure of the overlap will be discussed later when more information regarding the mobilities and carrier densities is available.

The room temperature resistivities of 400×10^{-8} ohm m of the specimens from the outside of the bars are comparable to the values reported for pyrolytic graphite (Klein 1961, Blackman, Ubbelohde and Saunders 1961). The negative slope of these samples is also in agreement with these reports. Note the change in scale in crossing the axis $\rho_T / \rho_{300} = 1$.

TABLE IV

	22B	22C	22D	22F	22G	22H	20A	20B	10C	10D	6B	6E
$\rho_{300} \times 10^{-8}$ m	44	45	53	94	262	433	79	65	—	—	178	242
Slope of Lattice Mobilities	-1.28	-1.3	-1.17	-1.11	-1.35	—	-1.22	-1.29	—	—	-1.00	-1.00
Value at 300°K m²/V sec.	1.2	1.25	1.06	0.8	1.10	—	1.2	1.3	—	—	0.91	0.91
Temperature Independent Mobility m²/V sec.	19.0	9.5	8.0	2.0	0.22	0.13	12.2	20.5	0.23	0.13	0.5	0.3
Crystallite Diameter	3.8	1.9	1.6	0.4	0.04	0.026	2.44	4.1	0.046	0.026	0.1	0.06

FIGURE 31

VARIATION OF RELATIVE RESISTIVITY WITH TEMPERATURE
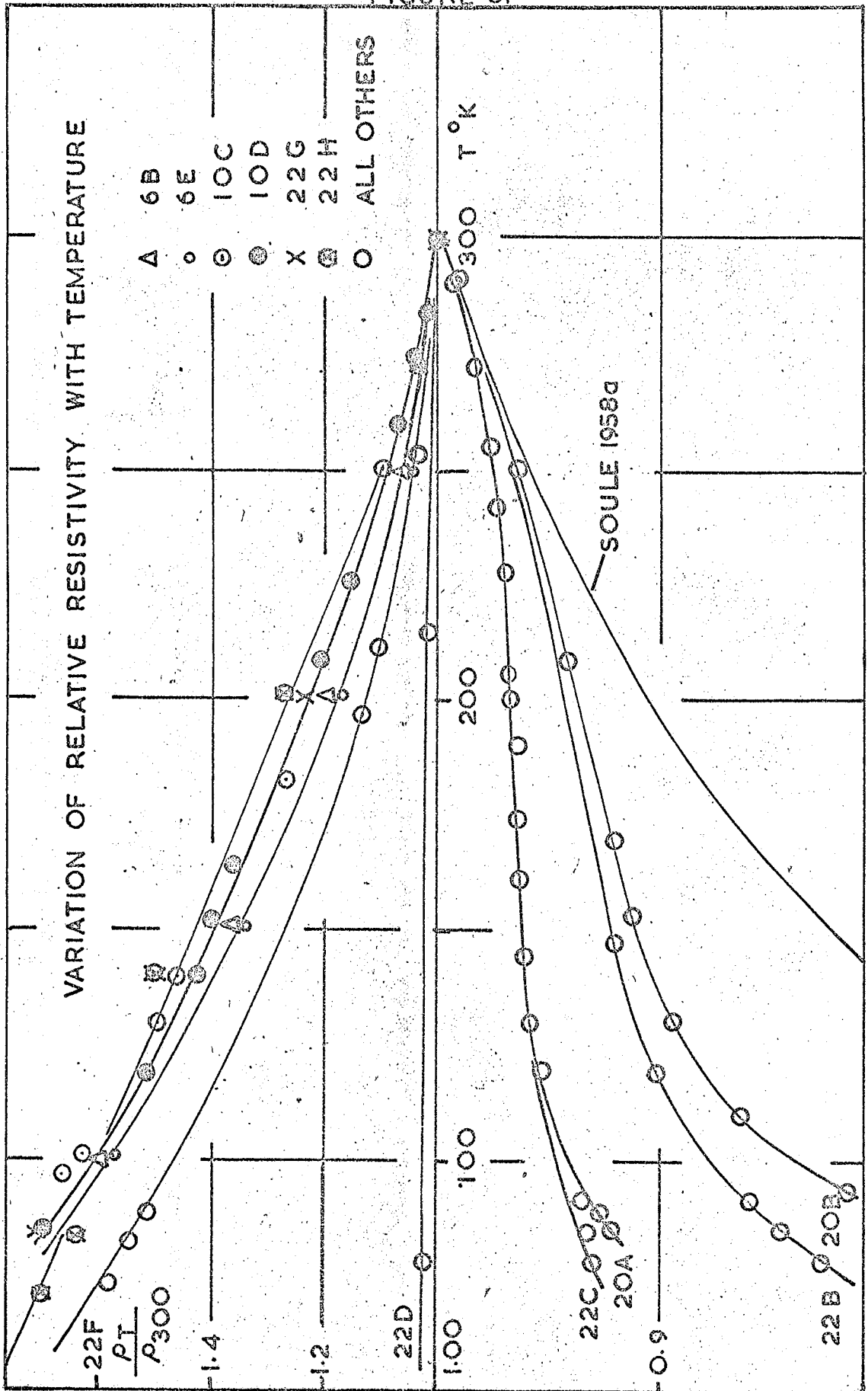
A log-log plot of the temperature variation of the resistivities of the samples with the negative slope is shown in figure 32. These samples all appear to vary in a similar way with a slope of $T^{-0.5}$ from a temperature of $120^{\circ}K$ upwards. Possible explanations for the temperature variation of the resistivity for all the samples will be discussed when the mobilities and densities of carriers are known.

The mobilities of the carriers (μ_{av}) are determined from the magnetoresistance effect, $(\frac{\Delta\rho}{\rho_0})$, (equation 3.8 of part I). The variation of this effect at 0.286 W/m^2 is shown in figures 33 and 34. In figure 33 is shown $\frac{\Delta\rho}{\rho_0}$ of samples from bar 22 while the curves in figure 34 shown $\frac{\Delta\rho}{\rho_0}$ for the rest of the samples.

The poorer specimens, that is, those with resistivities greater than 200×10^{-8} ohm m, sometimes exhibit negative magnetoresistance at low temperatures. This throws doubt on the use of this effect as a measure of the mobility in these samples at higher temperatures. The negative magneto-resistance can be explained in terms of gross defects (Saunders 1964a). Since this effect is not relevant to the present work it will not be discussed further . Note that the values exhibited for samples 10 C, D are at a value of induction of 0.5 W/m^2, instead of at the usual value of 0.286 W/m^2. This higher value of induction was employed to increase the size of the effect in these specimens.
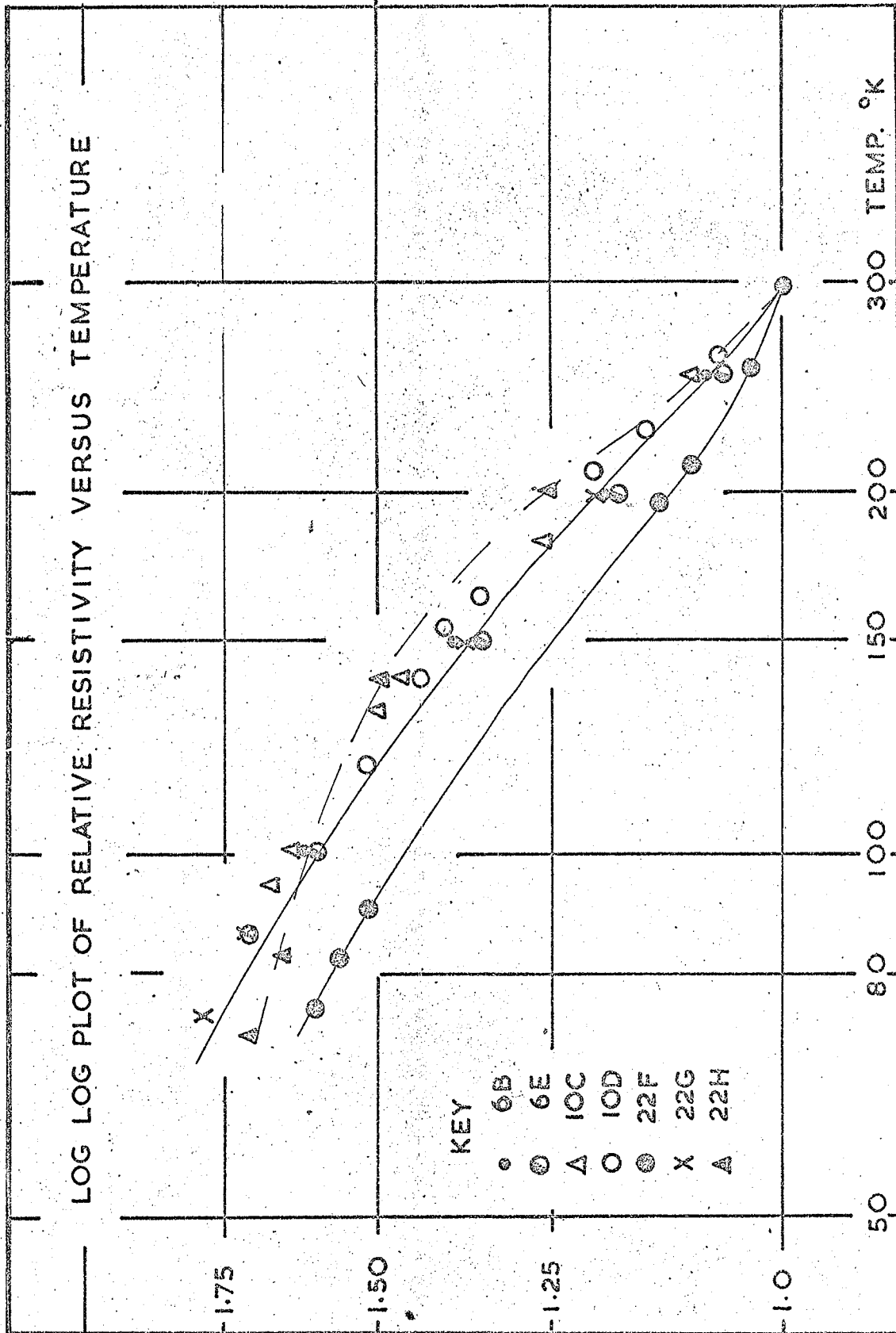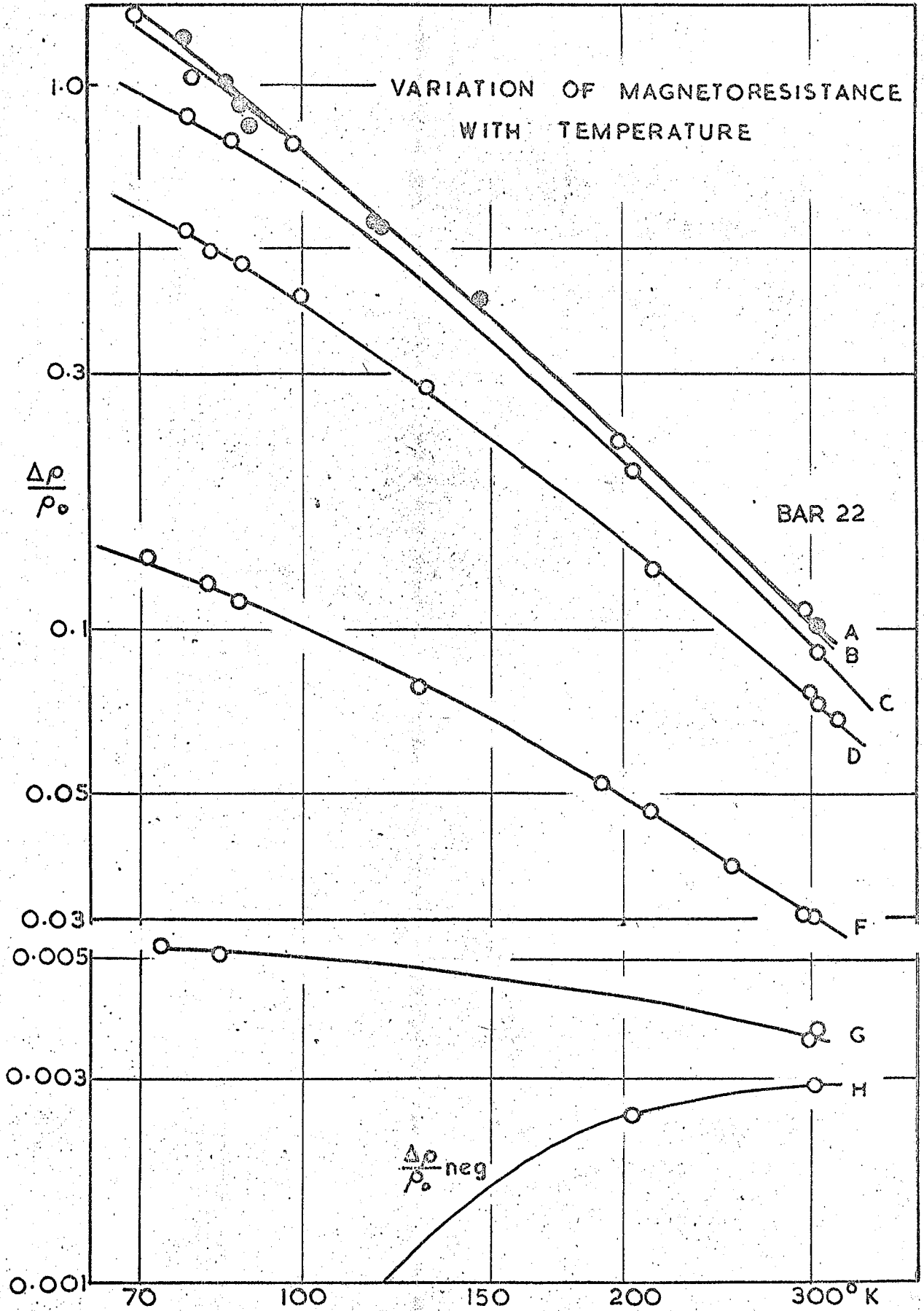
FIGURE 32

LOG LOG PLOT OF RELATIVE RESISTIVITY VERSUS TEMPERATURE

KEY
6B
6E
IOC
IOD
22F
22G
22H

FIGURE 33

VARIATION OF MAGNETORESISTANCE
WITH TEMPERATURE

BAR 22

The mobilities derived from these data are shown in figure 35 and 36. As discussed in section 1.3.2. these curves are not the values of the zero induction mobilities. In figure 37 is shown typical plots of μ_{av} against magnetic induction B, for various samples and temperatures. From these curves the zero induction mobilities were deduced to help to set up figure 10 of section 1.3.2. From figure 10 the values of the zero induction mobilities for other temperatures and samples are deduced and these are shown in figures 38 and 39. In addition the curves for Soule's sample EP11 are displayed for comparison.

Before discussing the effect of the mobilities on the resistivities it is necessary to know the densities of carriers. These are determined from the zero induction mobilities and the resistivities according to section 1.3.2.

The variation of n_{av} with temperature is shown in figure 40. The number of carriers only varies from 3.5 to $6 \times 10^{24}/m^3$ from sample to sample throughout the whole range of graphites considered. These values are in good agreement with the values for other pyrolytic graphites and for single crystal graphite. The slope of approximately 1.0 is thought to be purely fortuitious, being about half way between the exponential variation of a semiconductor and the temperature independent variation of a metal. The poorer samples have a smaller slope of 0.5, which derives from the slope of the

FIGURE 35

VARIATION OF AVERAGE MOBILITY WITH TEMPERATURE

FIGURE 36

VARIATION OF AVERAGE MOBILITY WITH TEMPERATURE

FIGURE 37

AVERAGE MOBILITY AGAINST MAGNETIC INDUCTION

FIGURE 38

VARIATION OF ZERO INDUCTION MOBILITY WITH TEMPERATURE

FIGURE 39

FIGURE 40

AVERAGE DENSITY OF
CARRIERS AGAINST
TEMPERATURE
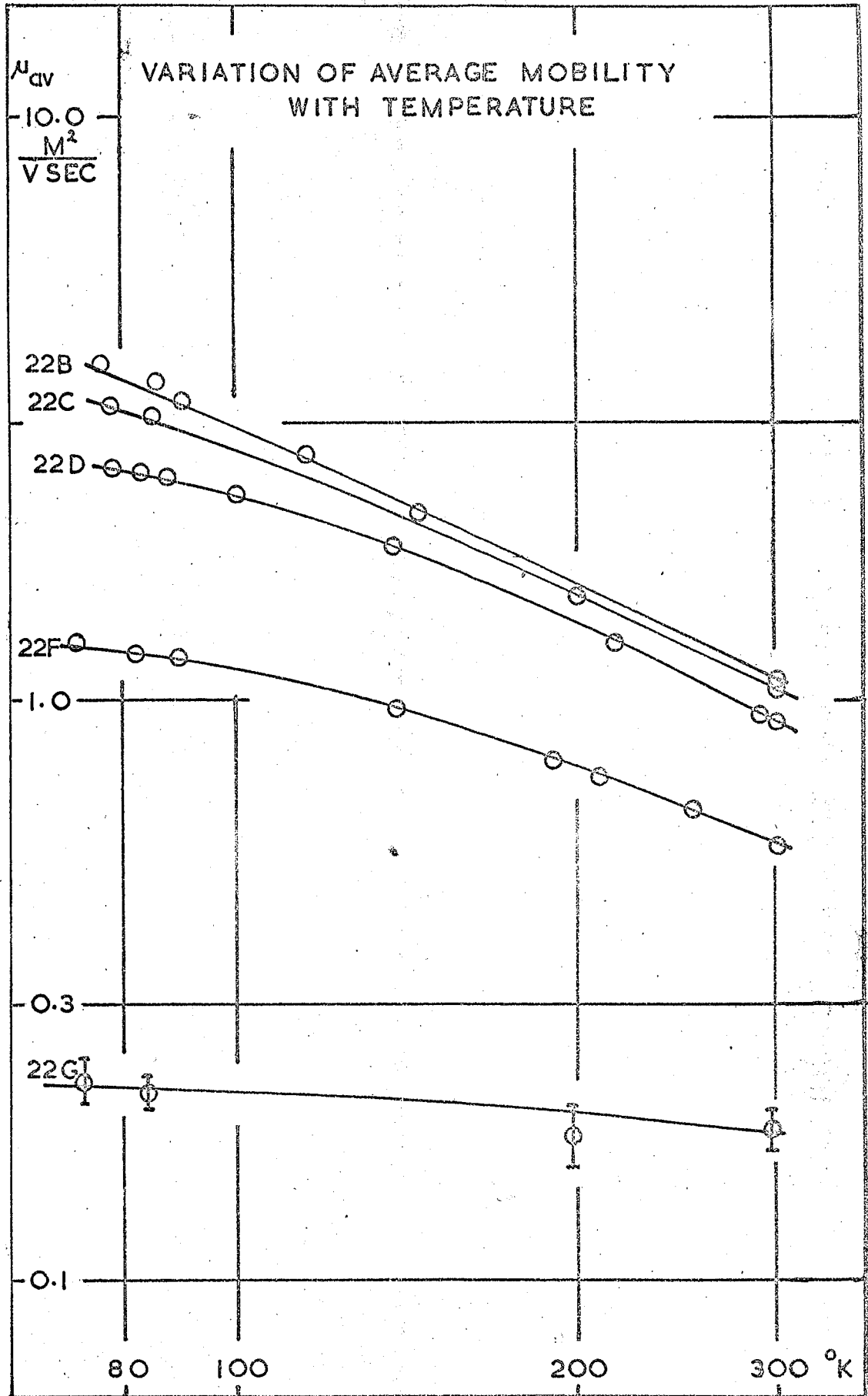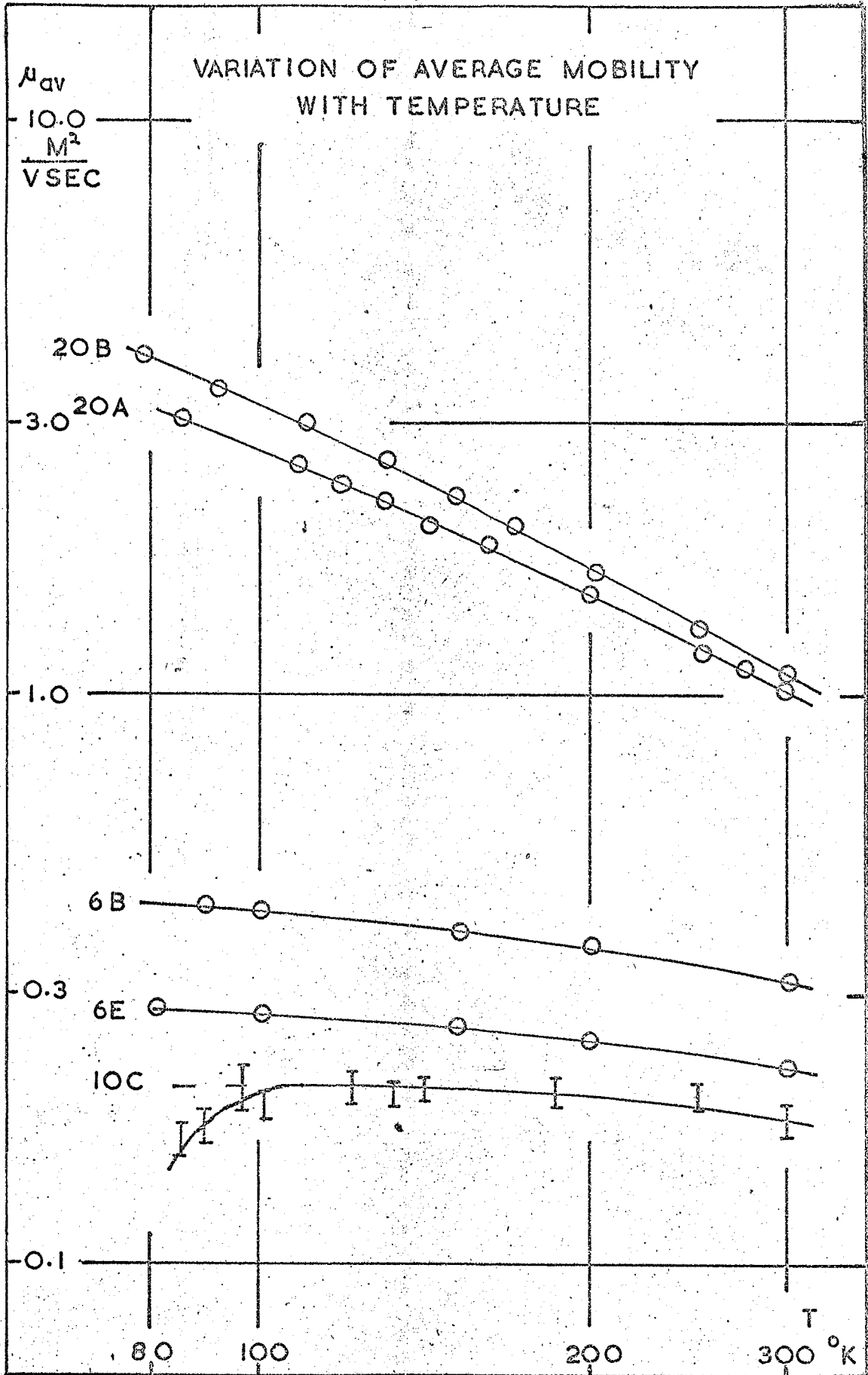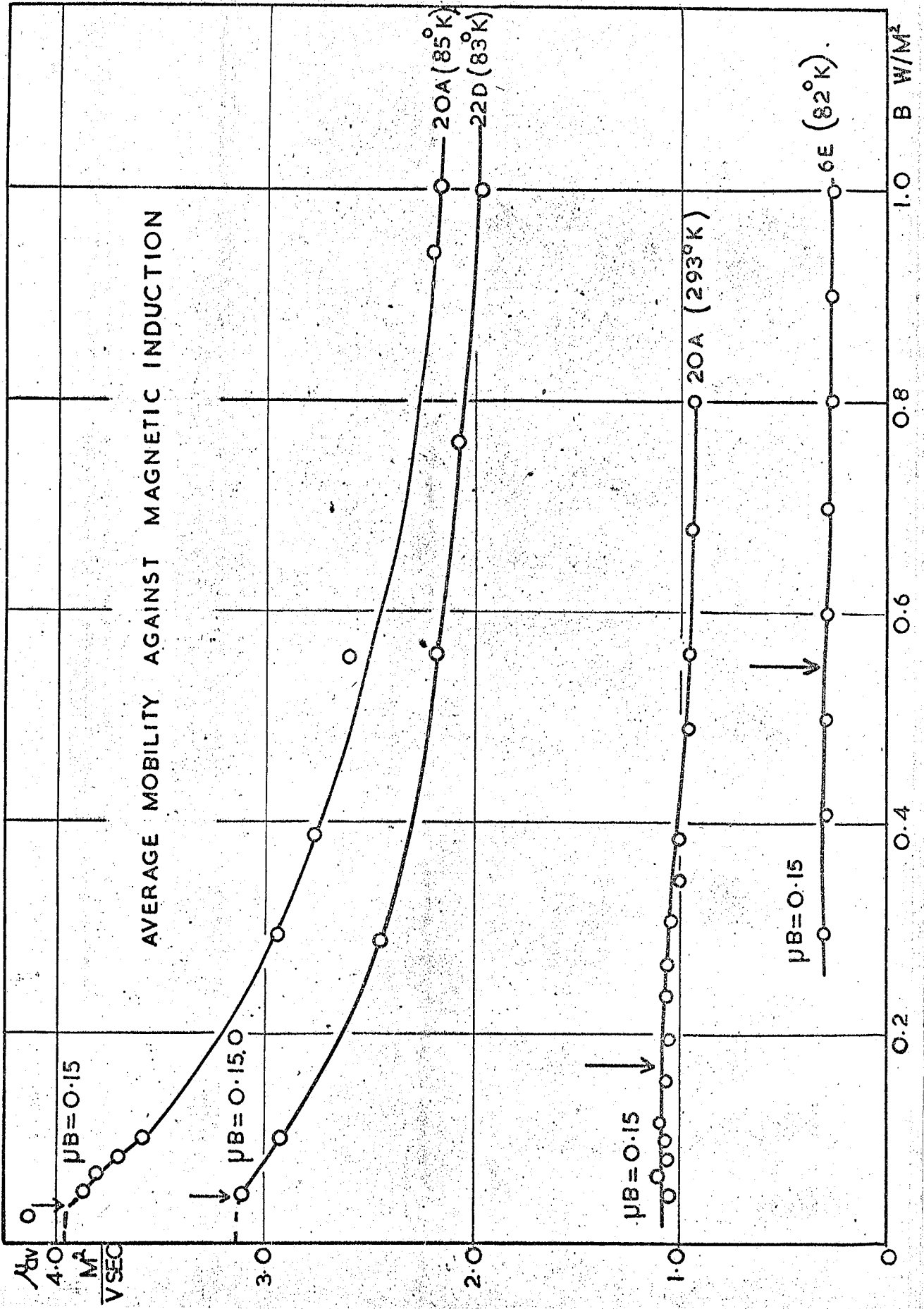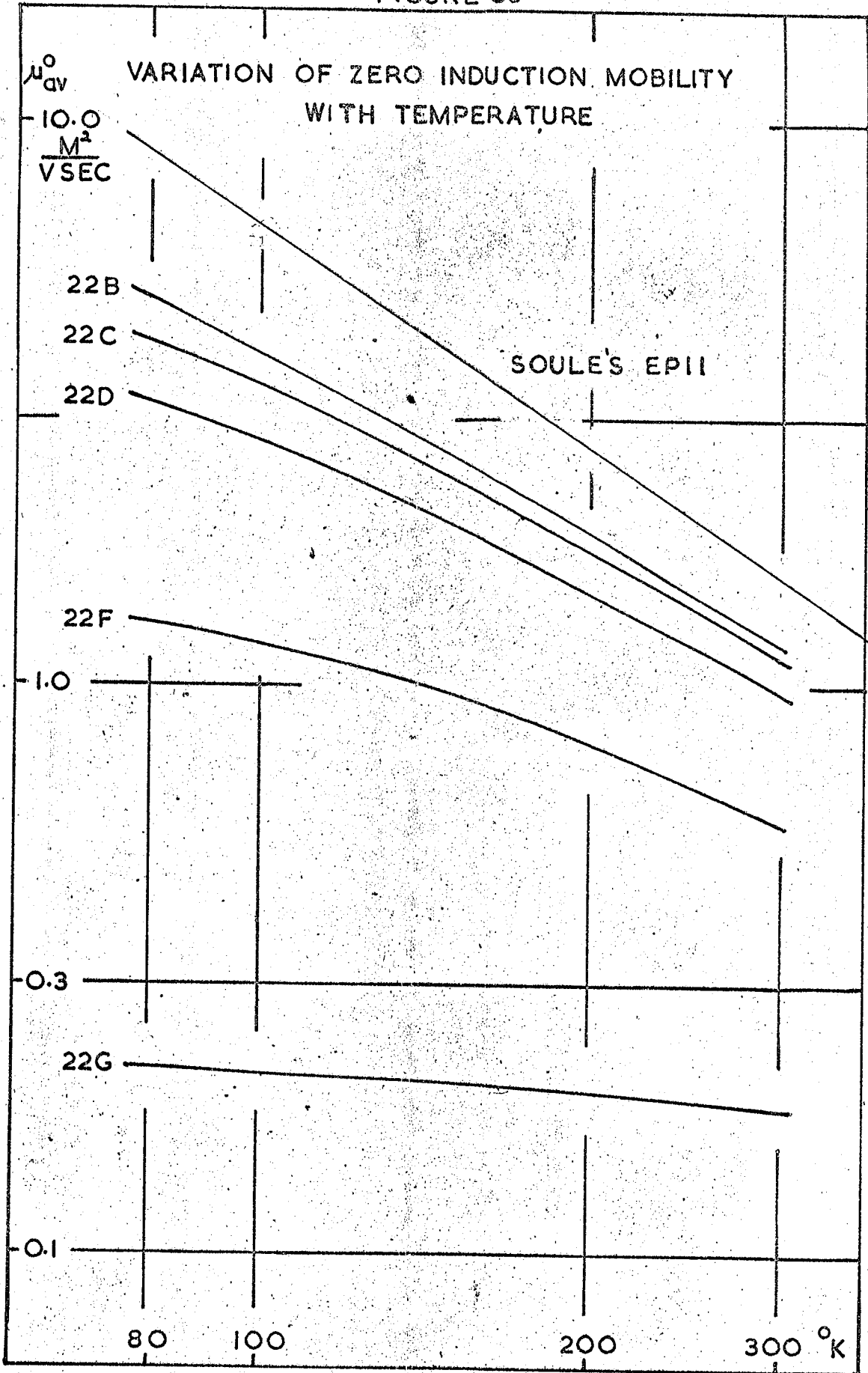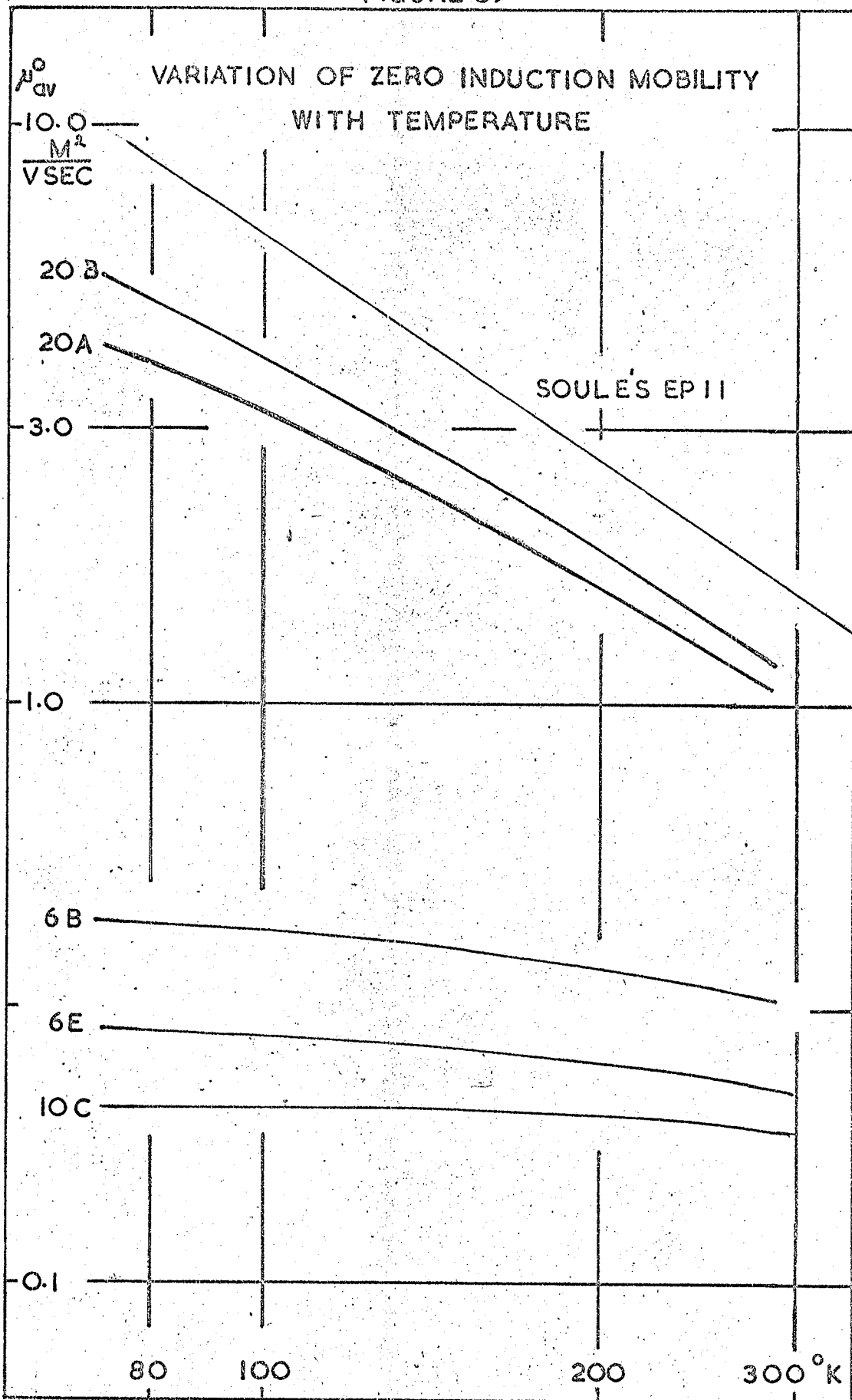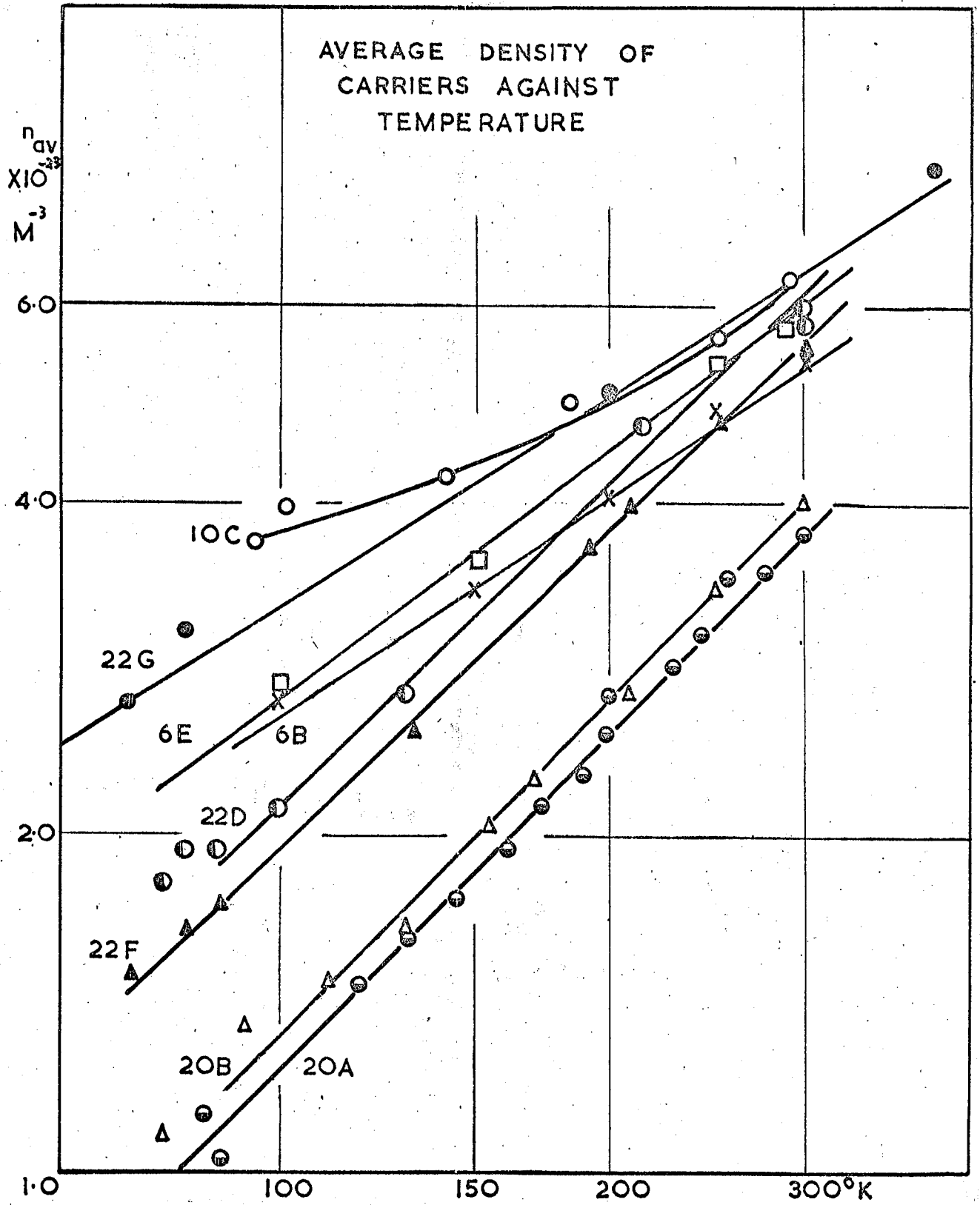
resistivity versus temperature curve for these samples. This suggests that for the samples with negative magnetoresistance at low temperatures the mobilities can be determined from the resistivity assuming the density of carriers is the same in these samples as in the better samples. The values for the mobilities so determined are given in table IV. These are temperature independent. All the values for the densities of carriers will be in error by as much as 15% because of the assumption b = 1.

In the better samples a tentative explanation for the break in the resistivity versus temperature curves can now be given. Since the mobilities are smooth functions of temperature over the region of the 'break' it must be due to the number of carriers starting to increase. This is then a measure of the band overlap, since the density of carriers starts to increase when kT becomes comparable with the value of the Fermi level. Since the Fermi level is, as a first approximation, at the centre of the overlap, the degeneracy temperature, as the temperature at which the break occurs has been called, corresponds to an energy half the value of the overlap. The values obtained for the good samples, that is those with positive temperature coefficient of resistivity are displayed in table V.

These values are in good agreement with the values determined by McClure (1958) by the same method, but are some 30 percent smaller than the value of 0.032 eV determined from

TABLE V

Estimation of Overlap

Sample	Overlap (eV)
20A	0.022
20B	0.025
22B	0.024
22C	0.022
single crystal	0.02

other experimental evidence.

The variation of the mobilities with temperature is in itself interesting. From the shapes of the curves in figures 38 and 39, the mobilities in the samples appear to approach a temperature independent value at low temperatures, and approach the single crystal line at high temperatures. On extrapolating to low temperatures and extracting the temperature independent mobility μ_{cb} by the formula for the addition of mobilities

$$\frac{1}{\mu_{av}^{o}} = \frac{1}{\mu_{th}} + \frac{1}{\mu_{cb}}$$

it is expected that the single crystal mobility μ_{th} will remain. The slopes and value of the lines at $300^{o}K$ determined in this way are given in table IV, along with the values of the temperature independent mobility with which it was obtained. Since only one value of μ_{cb} will give a straight

line, any other giving a deviation from the straight line
at low temperatures, the accuracy of the slope of the lines
and of μ_{cb} are of the order of the accuracy in the mobilities.
It is therefore obvious that the high temperature lines do
not approach the single crystal line but approach a line
whose slope depends on the sample perfection.

Samples 20B, 22B and 22C have the slopes nearest
to the single crystal value of - 1.35, the mean of the three
values being - 1.29. This is outside the experimental error.
In any case it is consistently low and the slopes of μ_{th}
for 20A, 22D, 22F, 6B and 6E respectively decrease to the
limit of - 1.0 in 6B and 6E. Since the order of these samples
is also the order of decreasing perfection as determined from
the temperature independent mobility, there must be some
correlation between the two. The gradual departure of the
slope from the single crystal value can be explained in terms
of the phonon-defect, phonon-electron interactions. However,
before discussing this it is necessary to know the percentage
of defects present.

Since pyrolytic graphite consists of many crystallites
aligned with their c_o axes parallel but otherwise randomly
oriented, it is expected that the boundaries of the crystallites
will present fixed scattering centres to the motion of the
carriers. This then explains the temperature independent
mobility μ_{cb} at low temperatures, for at these temperatures

the mean free path of the carriers is much larger than the
distance between the fixed scattering centres of the
boundaries, and the carriers will be scattered preferentially
on the boundaries instead of the phonons. Since graphite
at these temperatures behaves like a metal in that it has
a temperature independent drift velocity, the relaxation
time will be constant, since $\tau_d = L_d/v$ where L_d is the
distance between the fixed scattering centres, that is,
the crystallite boundaries, and v the thermal velocity of
the carriers.

This theory then gives a measure of the average
diameter of the crystallites, for the relaxation time can
be calculated from the value of the temperature independent
mobility from equation 3.4 of part I, and it can be assumed
that the average effective mass and thermal velocity will
not change very much from the single crystal values. The
values of crystallite diameters determined in this way are
given in table IV, employing the values for m^* and v of
0.05 gm and 7×10^5 m/sec. These values were obtained by
averaging the values for the two carriers of the single
crystal quoted by McClure (1958).

The values of the size of crystallites are in good
agreement with the estimation of the crystallite diameters
based on the position of the peak in the thermal conductivity
versus temperature curve (R. A. Morant 1964) in the same

samples. The magnitude of the diameters in the poorer

samples is also of the same order as the values reported

by Klein (1961) from x-ray measurements. It was not possible

to measure the crystallite diameter from the x-ray data

mentioned in sections 2.1.5. to 2.1.8.

Thus with crystallites of the order of a micron

down to 100 angstroms, the number of defects will be

correspondingly high and vary over the same number of orders

of magnitude. It has been suggested (Saunders 1964)* that

the large number of defects and boundaries will affect the

phonon-electron interaction. This is achieved by decreasing

the number of phonons available for this process by scattering

the phonons on the boundaries instead of the electrons.

Thus as the number of defects rises with decreasing perfection,

the high temperature line or lattice scattering term will have

a lower temperature dependence. This is of course a very

crude picture of what is happening in the material, but it

is thought to be a reasonable explanation of the mobilities

in this polycrystalline material.

So far only the 'average' mobilities $(\mu_1 \mu_2)^{1/2}$ have

been discussed. In order to determine the individual

mobilities it is necessary to know the ratio of the mobilities

which is determined from the Hall coefficient according to

equation 3.10. of part I.

* Private Communication

3.2.3. The Hall Coefficient and the Ratio of Mobilities

In extrinsic materials the Hall coefficient is one of the most important coefficients since it is a direct measure of the number of carriers and also gives the mobility of the carriers in conjunction with the resistivity. In an intrinsic material however, it is only a measure of the departure from the intrinsic condition if the mobilities are equal or, as in the case of graphite, a measure of the ratio of mobilities, since the number of electrons is, to all intents and purposes, equal to the number of holes.

The variation of the Hall coefficient with magnetic induction for several samples at different temperatures is shown in figure 41. On this information it was not necessary to plot the variation of Hall coefficient with magnetic induction at all temperatures, the values at 0.286 W/m^2 being the value at zero induction.

The variation with temperature of the Hall coefficient at this induction is shown in figure 42 for several specimens. Not all the samples are shown since they all have very similar values. The values at $300^O K$ are given in table VI for all the samples.

There appeared to be no correlation between the Hall coefficient and the perfection of the graphite.
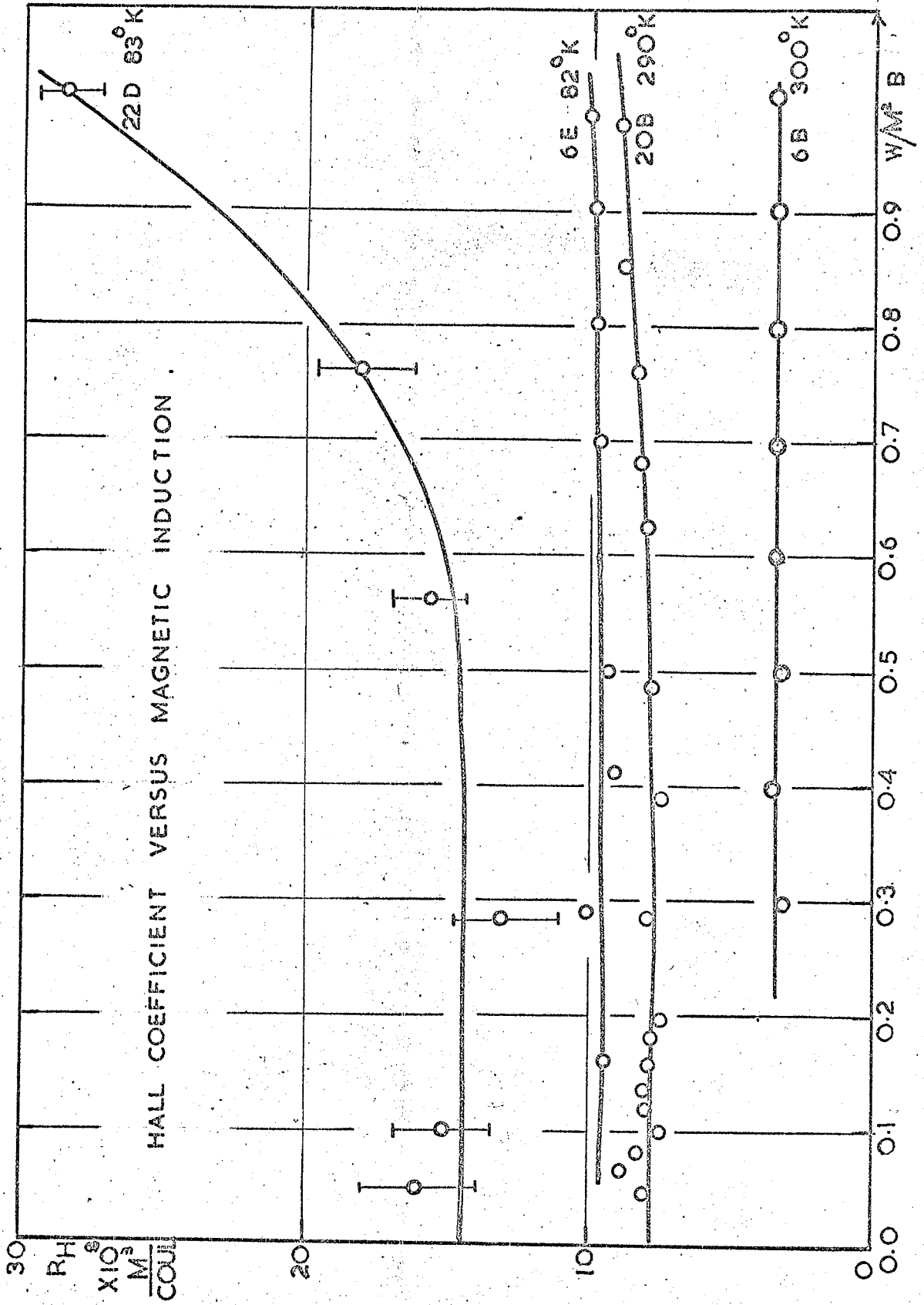
FIGURE 41

HALL COEFFICIENT VERSUS MAGNETIC INDUCTION.

FIGURE 42

HALL COEFFICIENT VERSUS TEMPERATURE

FOR VARIOUS SAMPLES
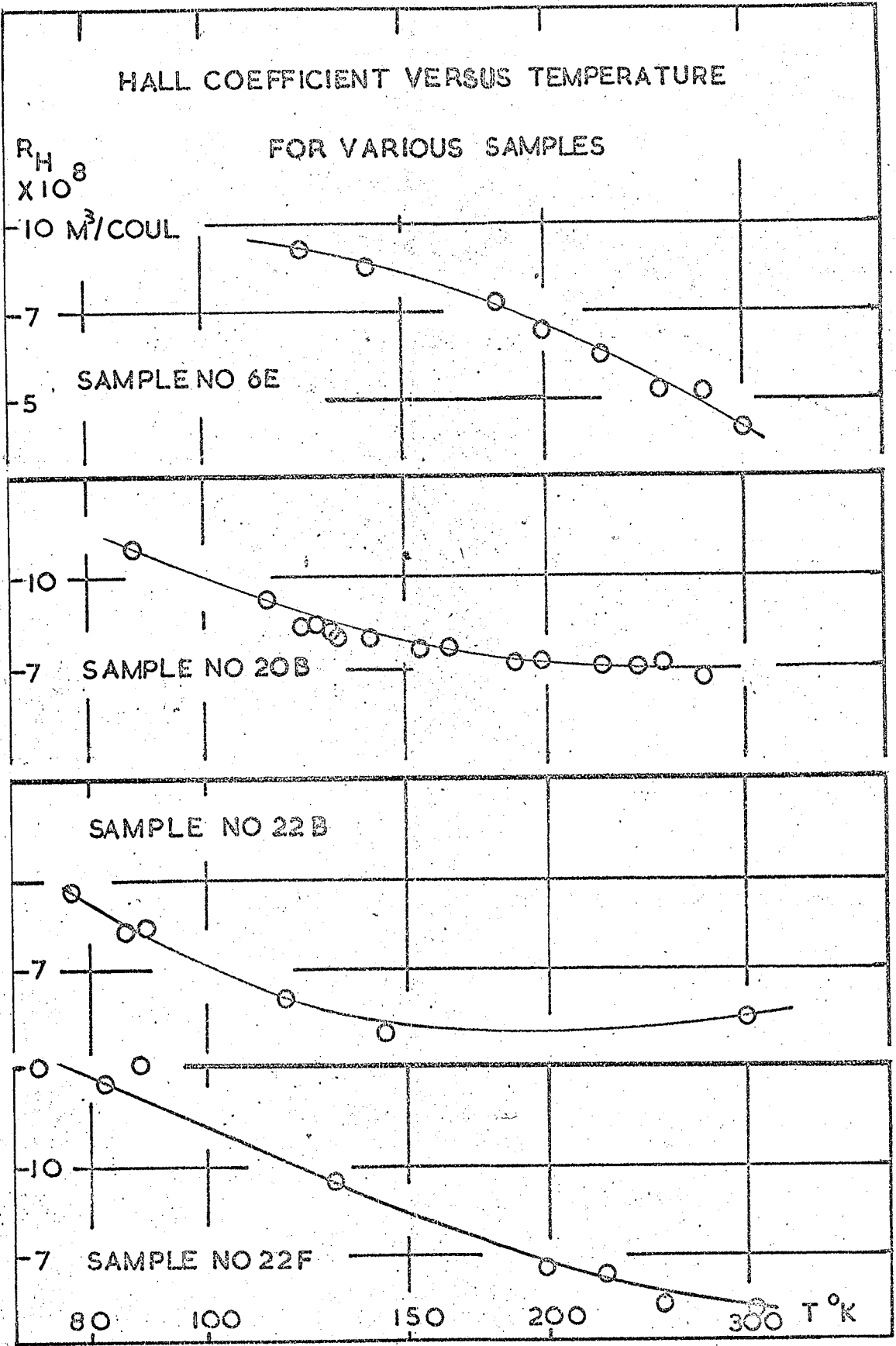
TABLE VI

Hall Coefficient for B = 0.286 W/m^2 300°K

Sample	22B	22C	22D	22F	22G	22H	20A	20B	10C	10D	6B	6E
R_H x 10^{-8} m^3/coul.	5.9	6.25	6.3	5.5	6.5	12.4	7.3	7.4	10.0	24	4.0	4.5

TABLE VII

Ratio of Mobilities

Sample No.	22B		22C		22D		22F		22G	
Temp.$^\circ$K	300	85	300	80	300	83	300	82	300	83
b	1.12	1.06	1.14	1.08	1.13	1.09	1.10	1.08	1.13	1.08

Sample No.	20A		20B		10C		6B		6E	
Temp.$^\circ$K	300	119	300	93	300	85	300	80	300	80
b	1.19	1.07	1.1	1.03	1.01	1.11	1.08	1.08	1.09	1.09

The values of the ratio of mobilities obtained from these data are shown in table VII. The spread of values of this parameter, being very insensitive to variation in the two factors R_H and n_{av}, is very small. Since no change in sign of the Hall coefficient was observed down to the lowest temperatures attained, the ratio of mobilities was never less than one. It was found to be practically temperature independent, varying from about 1.1 at room temperature to around 1.02 at liquid nitrogen temperatures.

With this parameter the individual mobilities can be

calculated from the equations

$$\mu_1 = \sqrt{b}\,\mu_{av} \qquad\qquad \mu_2 = \mu_{av}/\sqrt{b}$$

<div align="right">2.1.</div>

3.2.4. The Transverse Nernst-Ettingshausen Coefficient

In the previous section it was shown that the scattering coefficient in even the best pyrolytic graphite measured in this work, was likely to deviate from the single crystal value. Thus the computer programme may not predict the experimental results which follow. In this programme it was assumed that the value of the scattering coefficient was 0, the value for acoustic mode lattice scattering. Since at room temperatures the percentage of crystallite boundary scattering was expected to be small, it should have at least predicted these results. Only when the two scattering effects become comparable should it fail. However when the results of the galvanomagnetic coefficients were analysed, and the departure of the high temperature mobilities from the single crystal line found, it was too late to change the computer programme. Thus the programme will not predict the values in pyrolytic graphite but only in single crystal graphite and the theoretical curves shown on the figures are those which would be expected in single crystal graphite, assuming a band

overlap of 0.032 eV the Fermi level at 0.016 eV, a = 1,

b = 1.1, and the mobilities quoted by Soule.

The variation of Q^t with temperature is shown in

figures 43 and 44. In figure 43 are the values for samples

from bar 22 and figure 44 the values for the rest of the

specimens.

The theoretical variation of Q^t with temperature

is similar to that measured, but the magnitudes do not agree

as expected. In order to have a better comparison with theory,

the values of Q' calculated from figures 43, and 44 are shown

in figure 45 for all the samples in which Q' decreases with

temperature. From figure 17, if Q' increases with temperature

then the material must have an energy gap. The variation

of Q' with temperature for these samples is shown in figure 46.

For these samples the size of the crystallites is so small

that it is difficult to analyse the data with any confidence.

The value of Q^t for the intrinsic material theoretically

ought to increase with induction, and then saturate, but if

the material is not strictly intrinsic then Q^t ought to fall

away at very high magnetic fields, as shown in figure 18.

Figure 47 shows the variation of Q^t with induction for various

samples at different temperatures. The transverse Nernst-

Ettingshausen coefficient is practically independent of

induction, only falling off very slowly at high values of

induction. This evidence, combined with the magnitude of the

FIGURE 43.
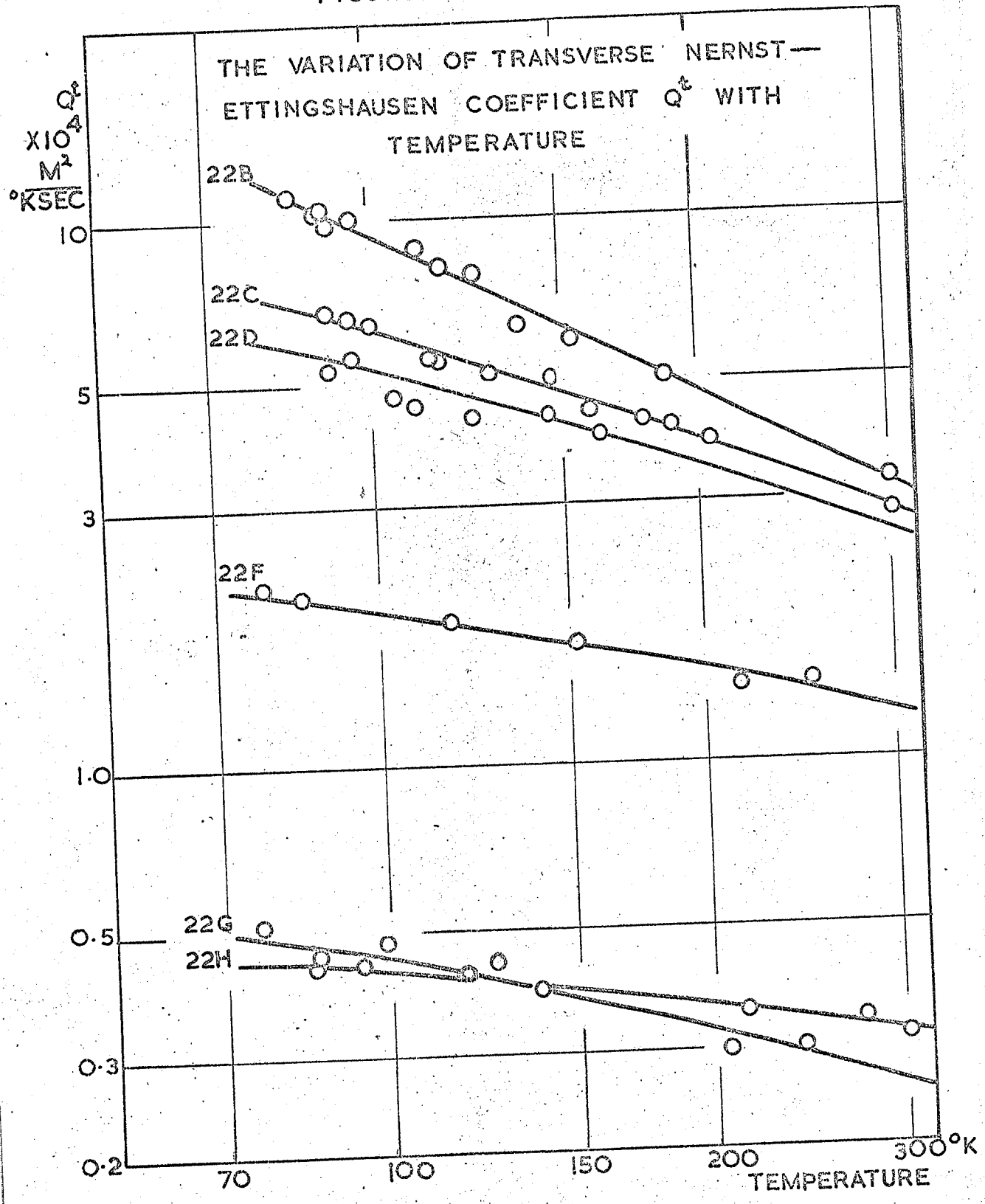
THE VARIATION OF TRANSVERSE NERNST—
ETTINGSHAUSEN COEFFICIENT Q^t WITH
TEMPERATURE

FIGURE 44

VARIATION OF TRANVERSE NERNST — ETTINGSHAUSEN COEFFICIENT Q^t WITH TEMPERATURE.
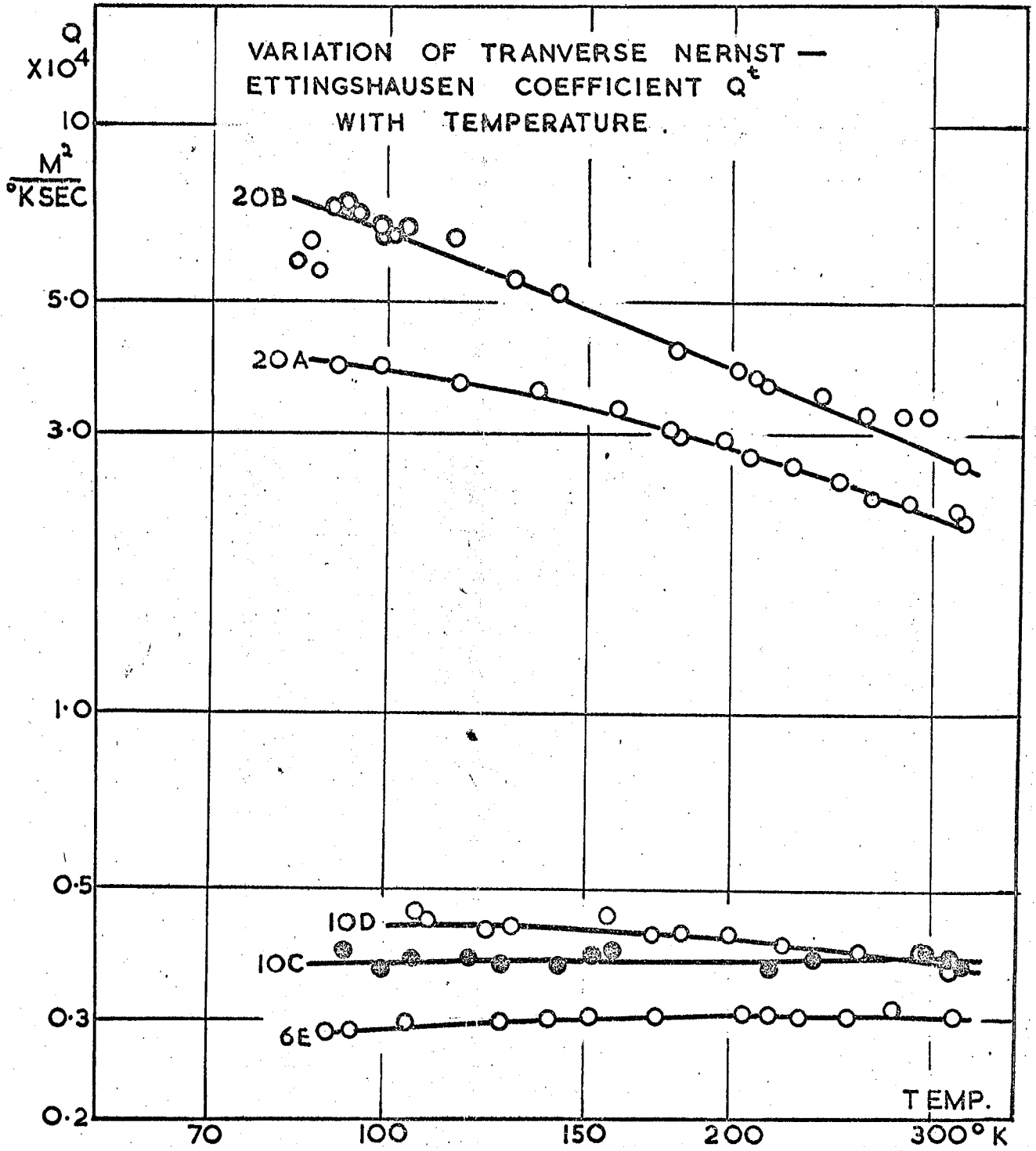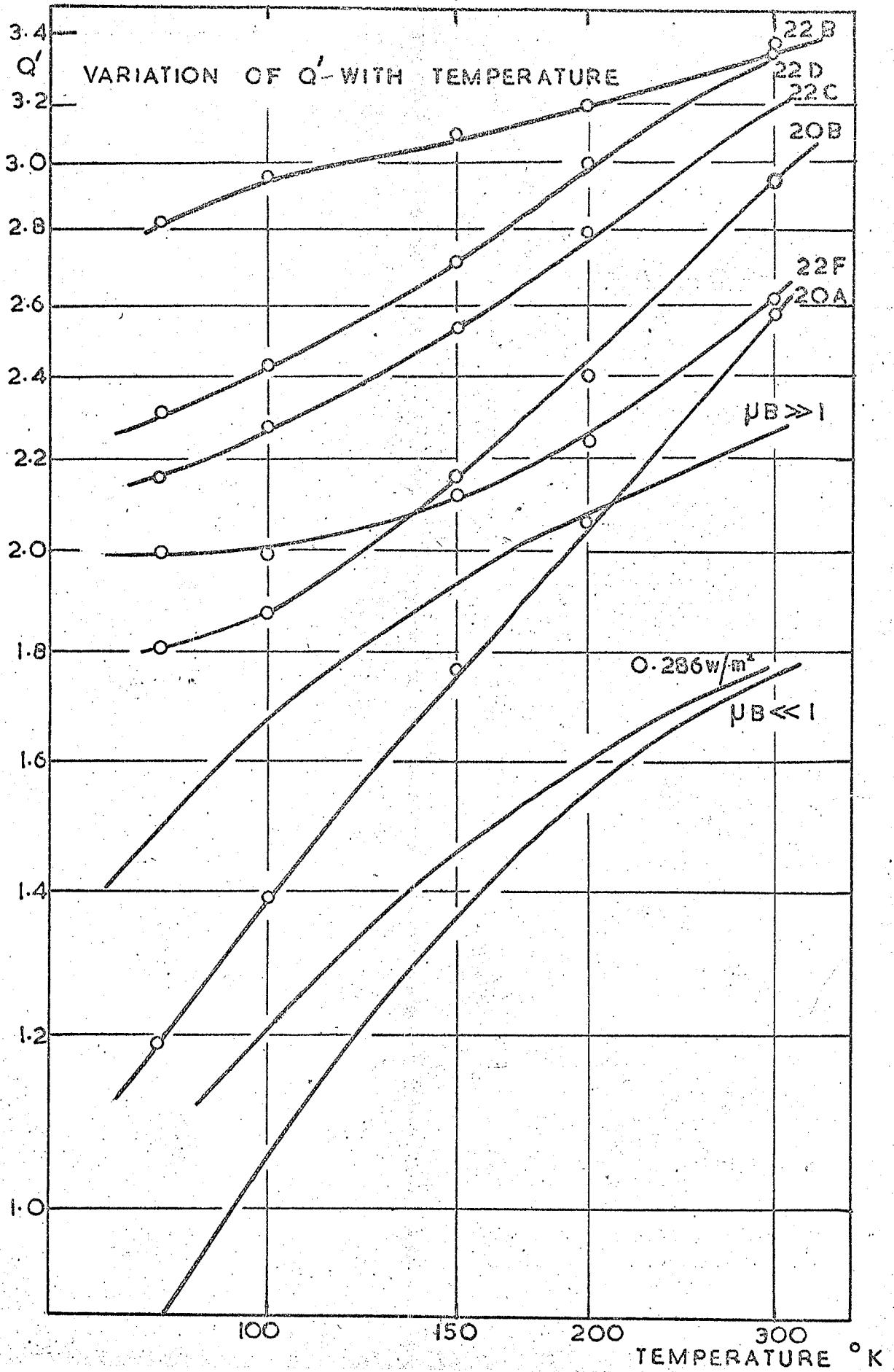
FIGURE 45

VARIATION OF Q'- WITH TEMPERATURE

coefficient appears to imply a band gap of about 3kT. This is in direct contradiction to all other evidence, and in view of the perfection of the better samples and the evidence in favour of an overlap in graphite the existence of a band gap in the present specimens is unlikely.

These discrepancies will be discussed later when the longitudinal Nernst-Ettingshausen coefficient has been discussed.

3.2.5. The Longitudinal Nernst-Ettingshausen Coefficient $\alpha(B)$ or $(Q^{\mathbf{l}})$.

The Seebeck coefficient has been measured in pyrolytic graphite before (Blackman, Ubbelohde and Saunders 1961) and it has been found to be small and negative. In the direction parallel to the c_o axis it is also small but positive. (Ubbelohde and Orr 1957). This difference in sign has been employed to make high temperature thermocouples.

The variation of the Seebeck coefficient with temperature is shown in figures 48 and 49. These curves are in very good agreement with those of other workers (Blackman, Ubbelohde and Saunders 1961). They are also in good agreement with measurements on the same samples made by R. A. Morant during the measurement of the thermal conductivity. However neither the present results or those of R. A. Morant have exhibited the peak at $80^{\circ}K$ which is shown in Blackman, Ubbelohde and Saunders
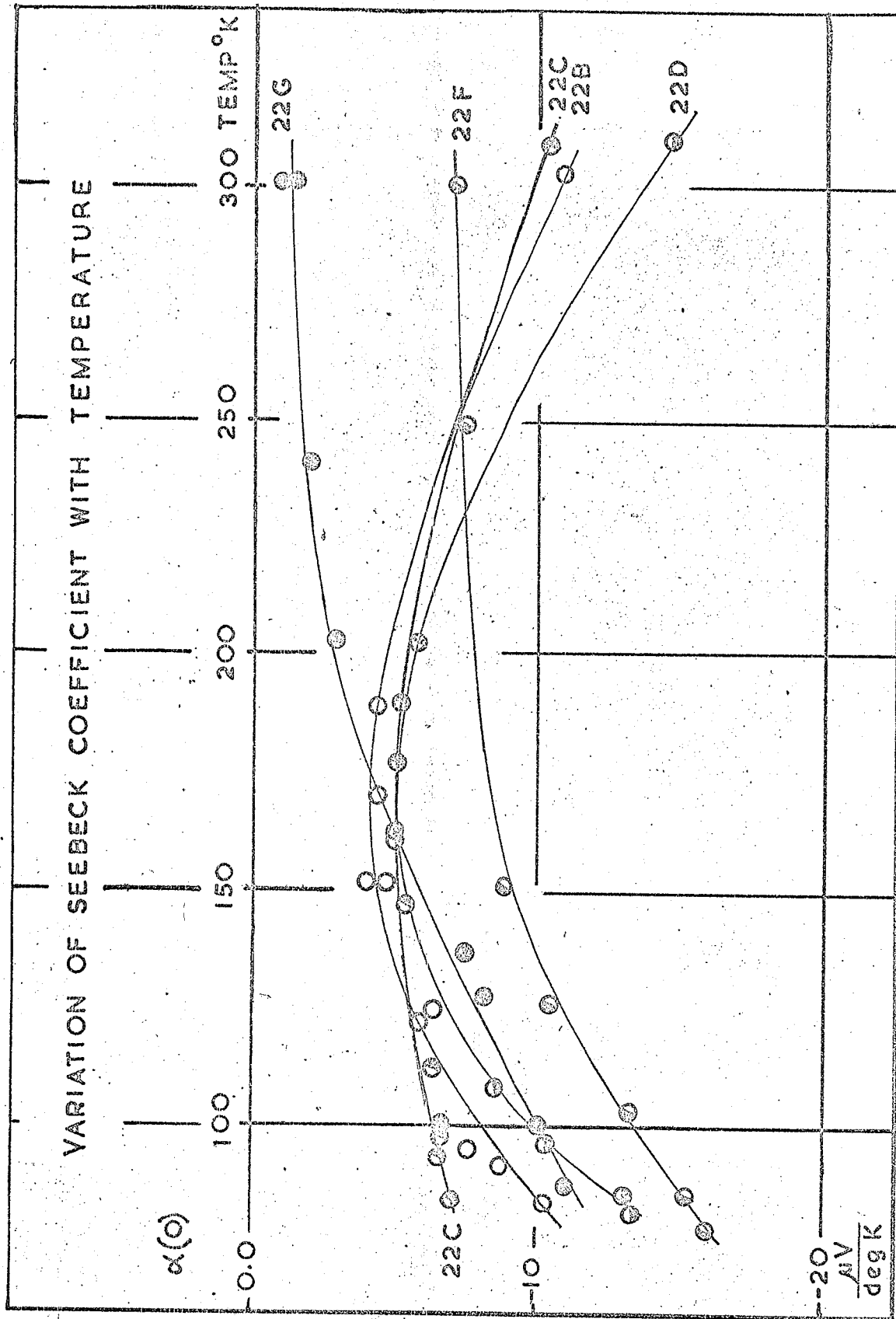
FIGURE 48

VARIATION OF SEEBECK COEFFICIENT WITH TEMPERATURE

FIGURE 49

VARIATION OF SEEBECK COEFFICIENT WITH TEMPERATURE
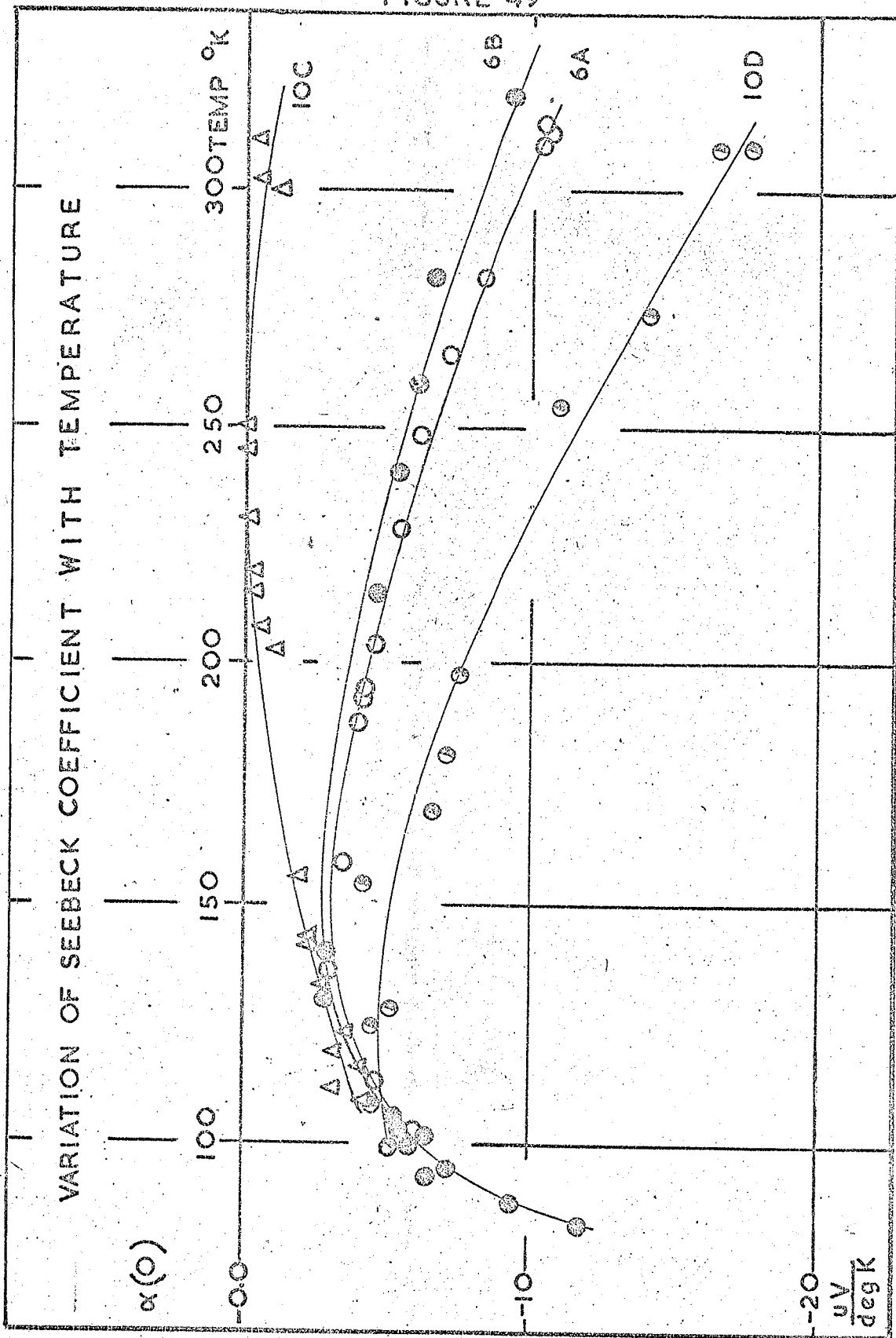
(1961). It is suggested that their peak which they ascribed
to the phonon drag phenomena could be due to an error in
the measurement of the temperature gradient or of the Seebeck
e.m.f., as discussed in section 2.3.2.

Klein has suggested that the variation of the Seebeck
coefficient with temperature can be explained by the variation
of the ratio of mobilities (Klein 1964). Since thermoelectric
power depends on the difference between the two carriers and
it has been shown that the ratio of the densities is very close
to one, the position of the Fermi level and the ratio of
mobilities are the only parameters which can affect it. The
position of the Fermi level should not change with temperature
while the change in the ratio of mobilities, although small,
is sufficient to cause the variation in the Seebeck coefficient
down to the maximum at $150^\circ K$. Below this temperature b
continues to decrease, while the Seebeck coefficient starts
to increase again. This could be due to a contribution from
the Phonon drag phenomena, but the peak must be at much lower
temperatures than indicated by Blackman, Ubbelohde and
Saunders (1961), and the same phenomena would be expected to
appear in the transverse Nernst-Ettingshausen coefficient.

The variation of the longitudinal Nernst-Ettingshausen
coefficient with magnetic induction exhibits some interesting
effects. Figures 50, 51 and 52 show the variation of $\alpha(B)$
with B for several samples at different temperatures.

FIGURE 50

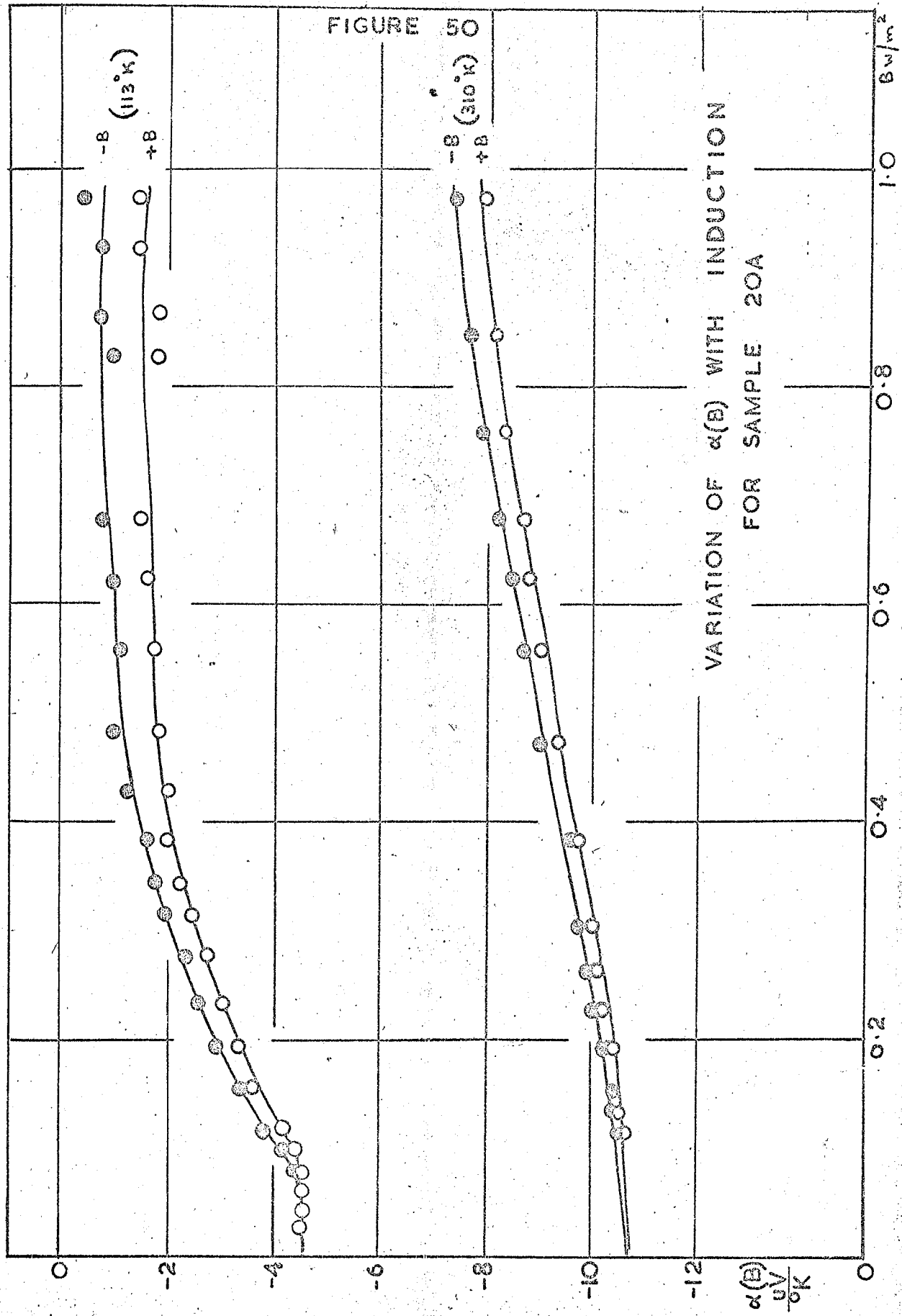VARIATION OF $\alpha(B)$ WITH INDUCTION FOR SAMPLE 20A

FIGURE 51

VARIATION OF α(B) WITH INDUCTION FOR SAMPLE 22C.

FIGURE 52

VARIATION OF LONGITUDINAL NERNST—ETTINGSHAUSEN COEFFICENT $\alpha(B)$ WITH MAGNETIC INDUCTION

Enlarged in Fig. 53

Sample 22B.
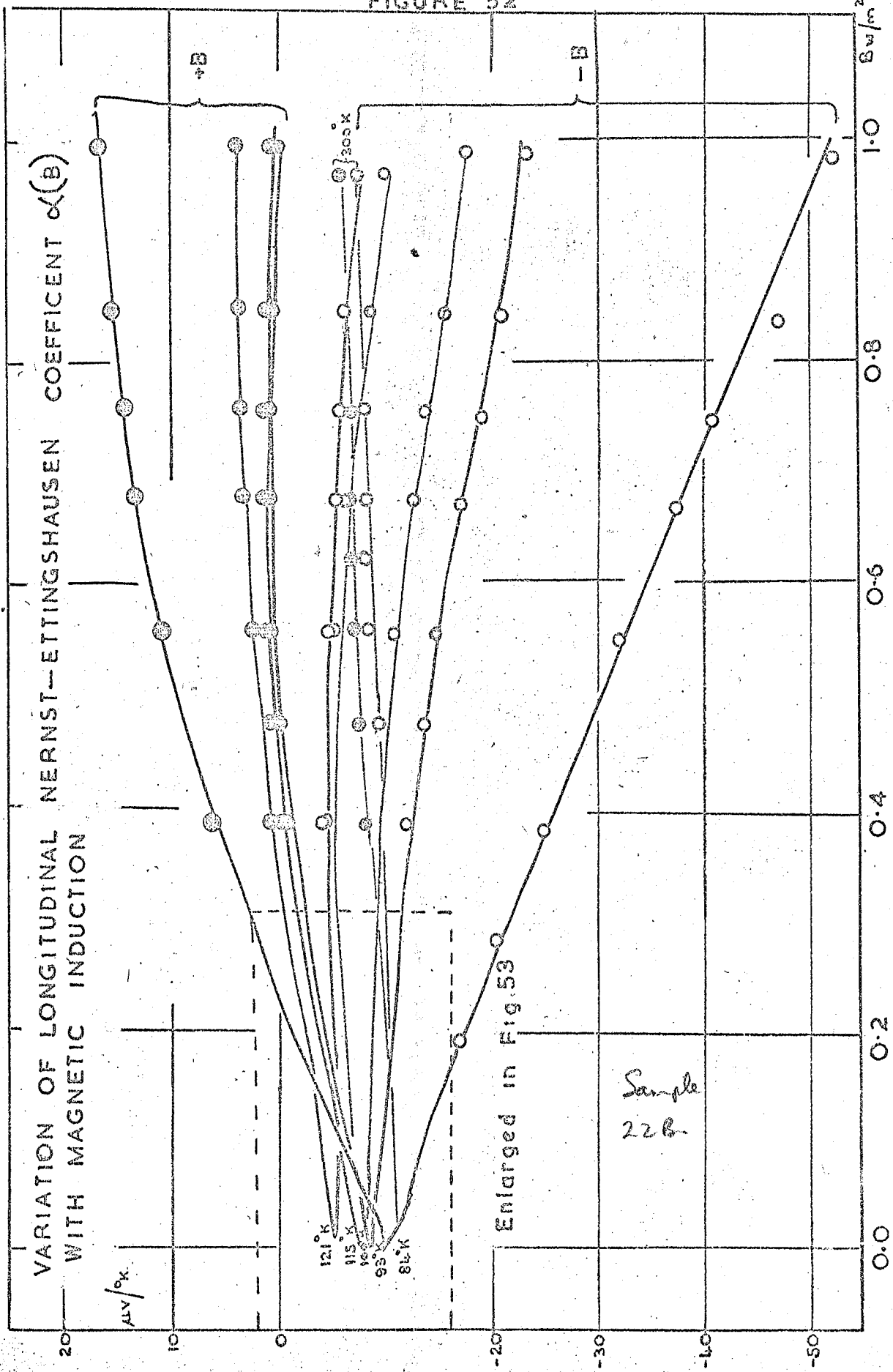
FIGURE 53

ENLARGEMENT OF INSET ON FIGURE 52
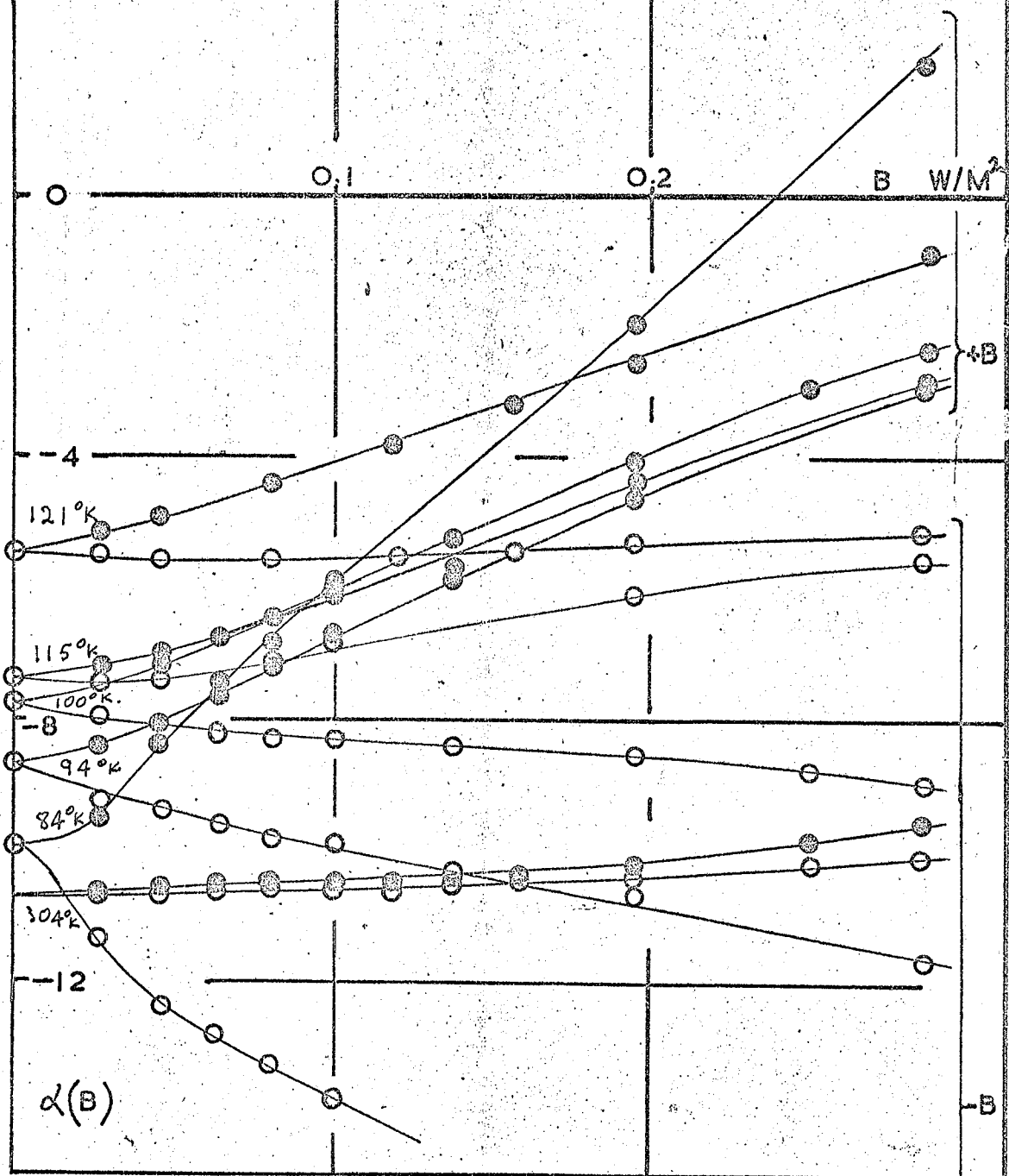
Figure 53 is an enlarged version of the area enclosed by the dotted lines in figure 52. It would appear from these figures that $\alpha(B)$ can be split up into two parts, one even in magnetic induction and the other odd. The even term (roughly quadratic) is approximately predicted by the theoretical results, but the odd or linear term shown in figure 54, for sample 22B is not predicted at all.

It has been suggested* that this linear term in $\alpha(B)$ can be produced by a misalignment of the probes, but it is difficult to see how this can happen in the arrangement employed in this work. The only possibility is that one probe contact is larger than the other. However it proved to be impossible to eliminate this 'oddness' by taking care during the attachment of the probes. Thus the existence of the 'Umkehr' effect, as this phenomena is called, in graphite must be regarded with suspicion until further evidence about it is obtained. If the 'oddness' is due to a misalignment of the probes, then it will be eliminated by taking the mean of the two readings. This has been carried out for sample 22B and the result is shown in figure 55.

Figure 56 shows the same curves for $\alpha'(B)$, against μB, for direct comparison with the theoretical. The inset is this curve reduced to the same scale as the theoretical results.

On comparing this curve with the curves in figures 25 to 30, the maximum at $\mu B = 1.5$ is hardly noticable on the

*Footnote:- Horst 1964, Private communication.

FIGURE 54

LINEAR PART OF α(B) AGAINST
MAGNETIC INDUCTION FOR SAMPLE 22B
AT VARIOUS TEMPERATURES

FIGURE 54

FIGURE 55

MEAN $\alpha_n(B)$ AGAINST MAGNETIC INDUCTION
FOR SAMPLE 22B AT VARIOUS TEMPERATURES

FIGURE 56

VARIATION OF $\alpha'_{b}(B)$ WITH μB FOR SAMPLE 22B AT VARIOUS TEMPERATURES

above curves to same scale as theoretical curves
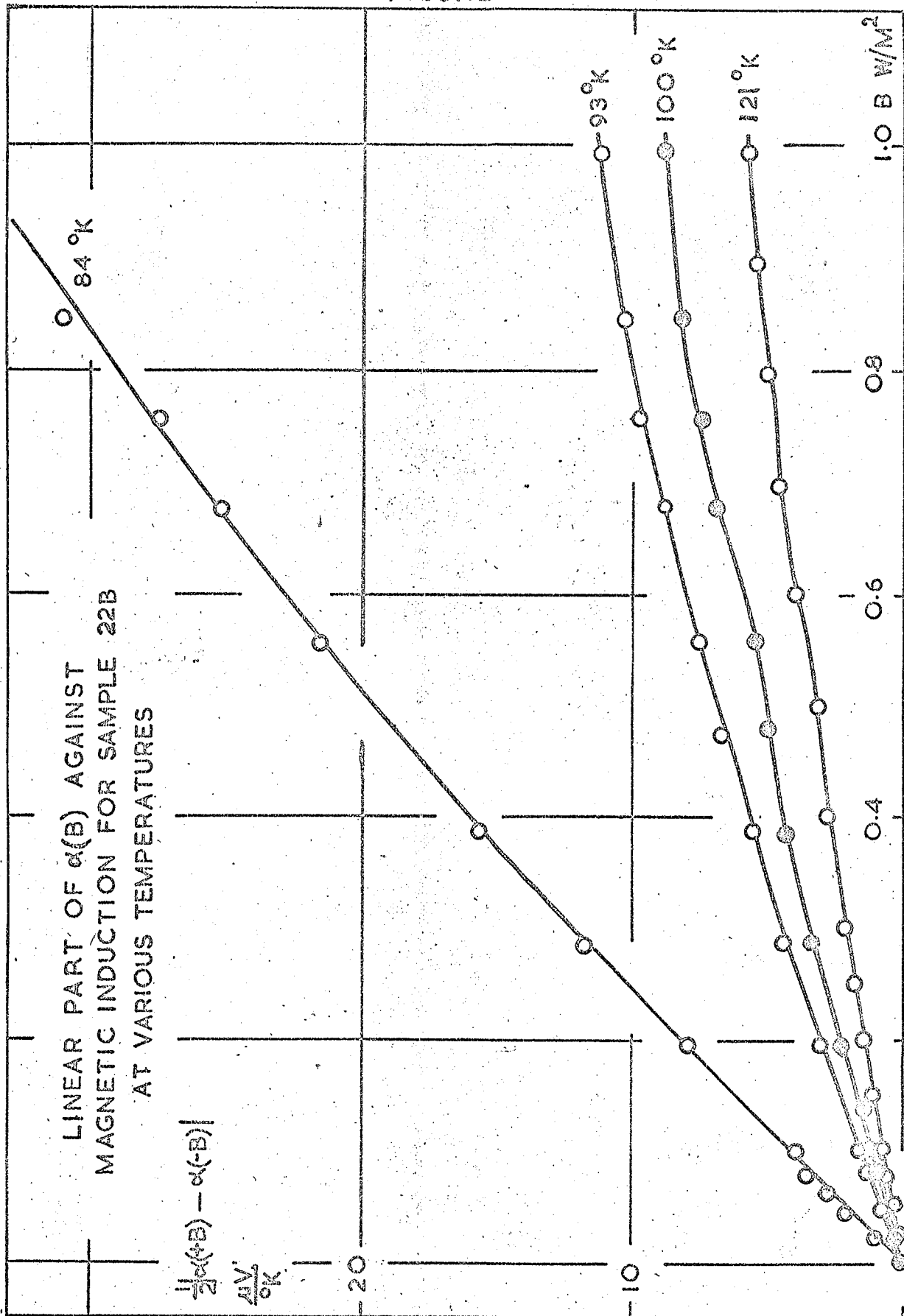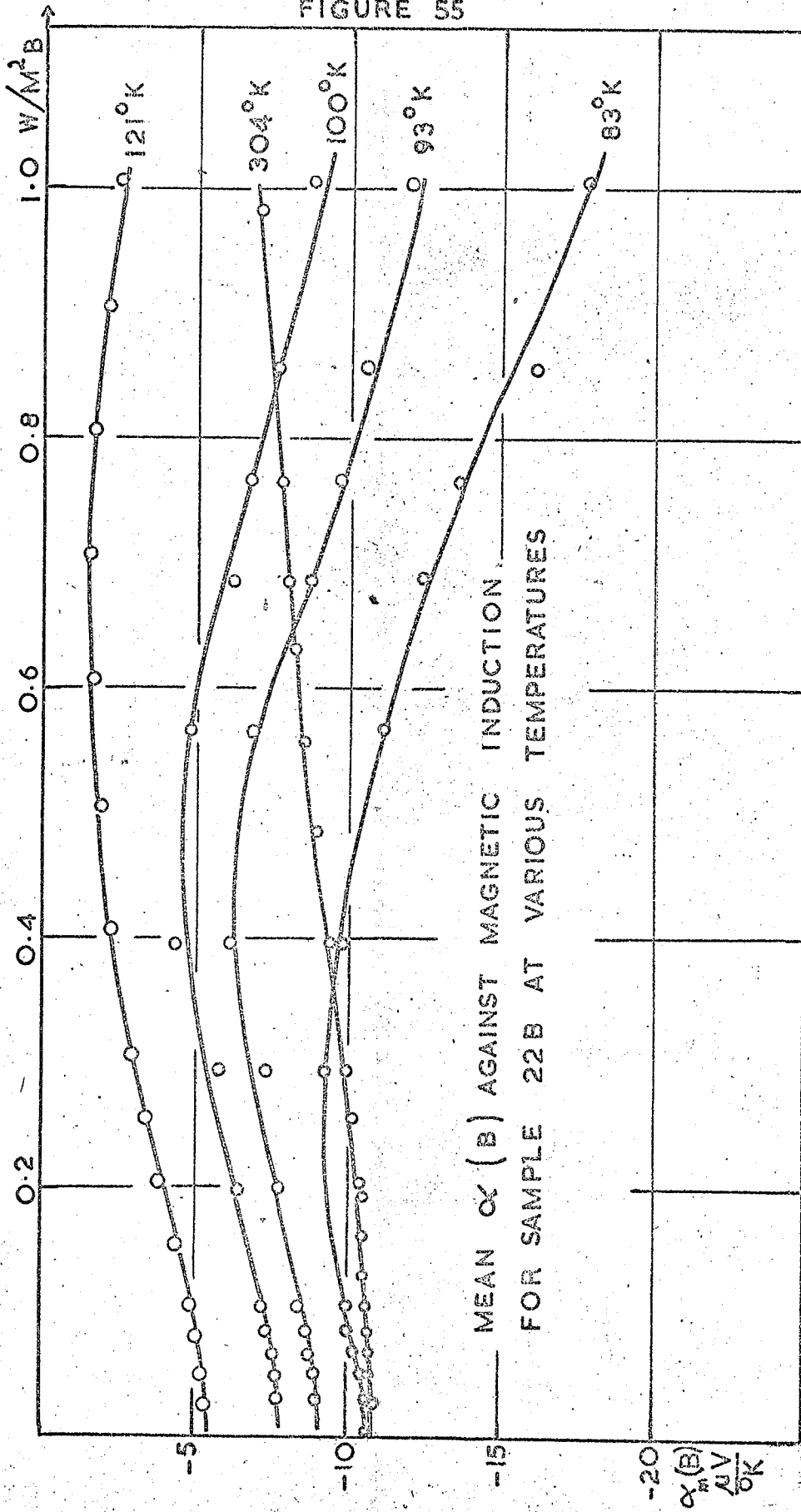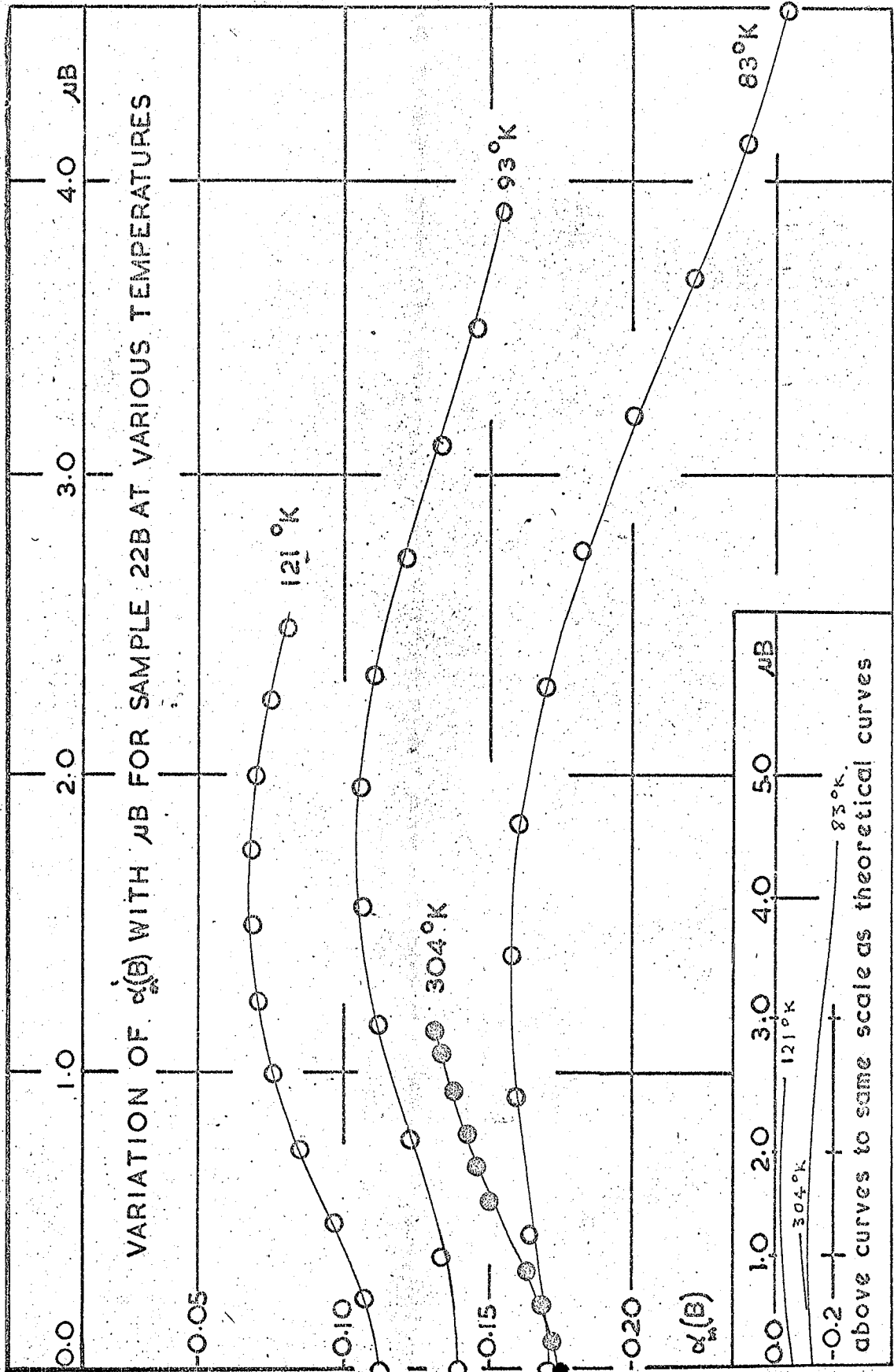
same scale as the theoretical graphs, and the overall smallness of the variation indicates that a is very close to one and that the Fermi level is in the centre of the overlap. The fact that $\alpha(B)$ appears to be tending to a constant value emphasizes this result. The results at room temperature cover too small a range of μB to be of much use.

Figure 57 shows the variation of $\alpha(B)_{mean}$ for the other two samples in which it was measured at low temperatures. In these two samples it is also apparent that a is close to one and that E_f is in the centre of the overlap.

The 'Umkehr' effect is not unknown in anisotropic materials. It occurs when the direction of the magnetic induction is not parallel to a mirror plane of symmetry. It arises from the off diagonal elements in the three dimensional tensors of the phenomenological coefficients S_{ij}^{k}. In bismuth it appears for certain orientations, and is quite large, the difference in the two readings at 1.0 W/m^2 being about 300 microvolts (Wolfe and Smith, 1963). These authors have also reported the preliminary results of some calculations taking into account the anisotropy of bismuth and have predicted the variation of this effect with the angle of the magnetic induction and with the magnitude of the magnetic induction. Their results agree well for the angular dependence but the predicted magnitude is in error.

Since the polycrystalline nature of the samples appears

to have altered the magnitude and variation of the transverse
Nernst-Ettingshausen coefficient with magnetic induction it
is also likely that the longitudinal Nernst-Ettingshausen
will be affected. This could also explain the 'Umkehr'
effect in pyrolytic graphite, due to the misalignment of the
a_o axis of the crystallites. However there are very many
crystallites and it is thought that any discrepancies due to
this effect would be averaged out.

These results will be discussed in chapter IV.

CHAPTER III

Variation of the Properties Throughout the Deposit

3.3.1. Introduction

In a paper by Blackmann, Ubbelohde and Saunders (1961) it was noted that there appeared to be a variation of the resistivity and the magnetoresistance through the thickness of the deposited graphite, the best material appearing near the interface of the substrate and the deposit. A lack of uniformity of these two effects for one bar was also noted in some of the early results in this work (see section 2.1.7.). Since there appeared to be no other report on this phenomena and since few other workers appeared to have taken this variation into account in their measurements it was thought that it should be investigated. To allow as large a variation as possible, bar 22 was grown as thick as possible. The final thickness of the deposit was 0.25 cms on a former of cross-sectional area of 0.2 x 1.0 cms^2. From this, a specimen 0.3 cms wide was cut and cleaved into 8 samples each about 0.03 cms thick. These were labelled from A to H with A the sample nearest the substrate. Both sample A and E were broken during the cleaving and although a few measurements were made on A, no measurements could be made on E.

It is thought that the lack of uniformity is due to the poor thermal conductivity of graphite parallel to the

c_o axis allowing a temperature gradient to be established. Morant (1964) has estimated that the temperature of the substrate at the end of the run was approximately 3000^oC, with a non-linear temperature profile as shown in figure 58. It will be shown later that this agrees with other results.

3.3.2. Measurements

The variation of the resistivity and the mobility at 300^oK is shown in figure 59. The shaded region next to the interface is where the layer of soot was removed. The dotted lines at sample A indicate that these are the results on the remains of this sample after it had been broken. These two curves indicate that the resistivity is relatively in-sensitive to the perfection of the deposit once a certain stage of graphitisation has been reached. The mobility is more sensitive in this respect, but perhaps the most sensitive of all the parameters is the average crystallite diameter, L_d as determined from the low temperature mobility. This parameter is shown as a function of the distance from the substrate in figure 60, together with the Transverse Nernst-Ettingshausen coefficient which is also more sensitive to perfection than the mobility.

If the temperature variation of the mobility of samples 22B and C is compared with the results of Klein (1963) as in figure 61, it is seen that these samples have properties

FIGURE 5 8

TEMPERATURE PROFILE ACROSS THICKNESS OF DEPOSIT
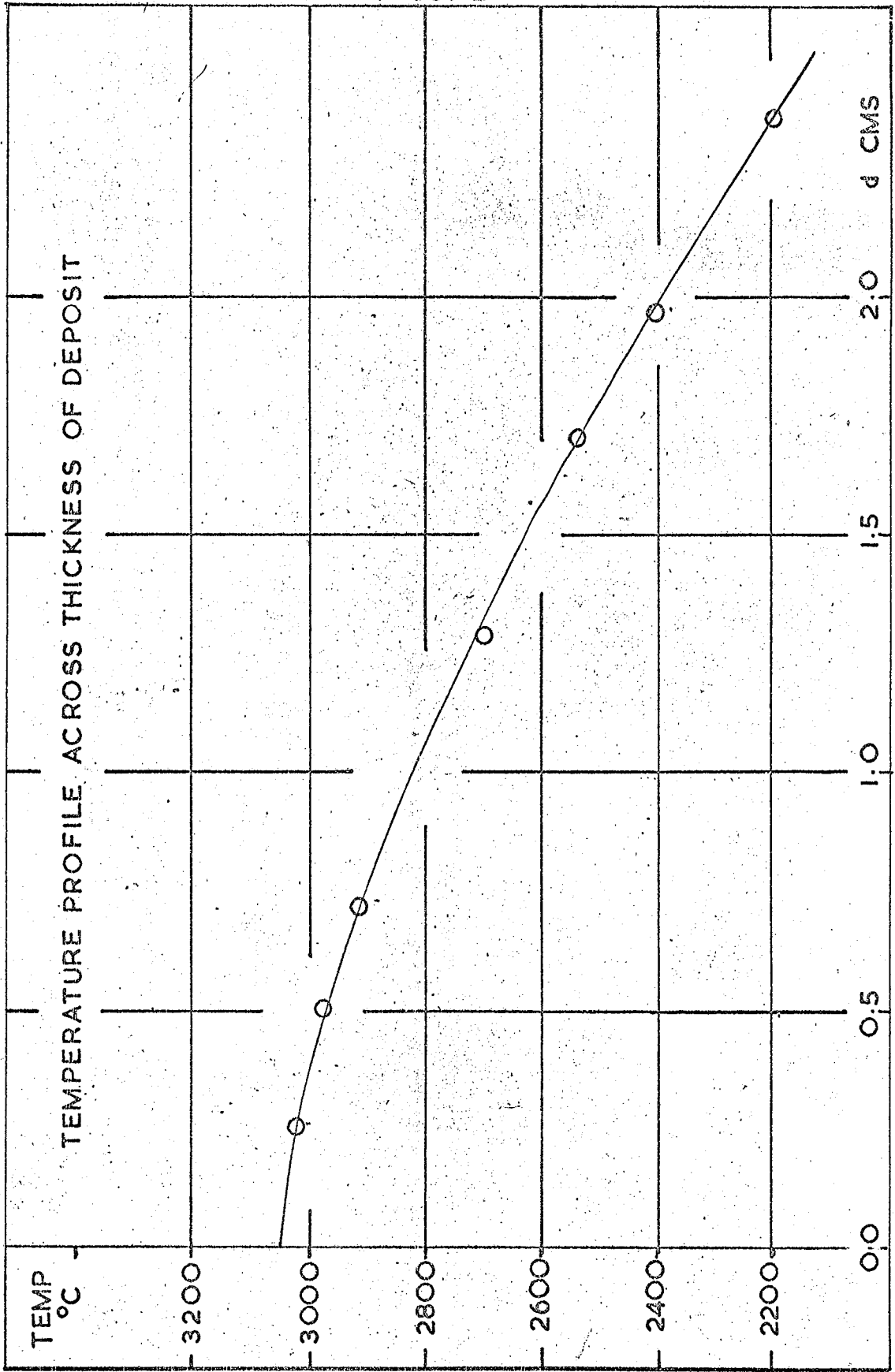
which compare very well with those specimens of Klein's which were annealed at $3000^{\circ}C$. This agreement with the estimated temperature of 22B at the end of the run is good in view of the fact that the samples here were annealed at a gradually increasing temperature under the constraint of the outer layers while Klein's specimens were annealed in a tube furnace free from any constraint.

Thus from figure 58 a temperature may be assigned to each cleaved surface and an average annealing temperature to each sample.

3.3.3. Comparison with other Results

Now that it is possible to assign an annealing temperature to each sample the variation of the effects with annealing temperature can be plotted. This is shown in figure 62 and 63 in which the present results on resistivity and mobility are confronted by the results of Meer (1963) and Klein (1963). Meer's samples were deposited at $2200^{\circ}C$ while Klein's were deposited at $2250^{\circ}C$. Thus the difference in the curves must be due solely to the different growing conditions, pressure, rate of flow of gas and the configuration all probably playing a part. Meer did not report any magnetoresistance measurements.

The fact that the resistivity decreases sharply at an annealing temperature of approximately $2400^{\circ}C$ at which the

ρ_8 X 10

ROOM TEMPERATURE RESISTIVITY AGAINST ANNEALING TEMPERATURE

FIGURE 62

ROOM TEMPERATURE RESISTIVITY AGAINST ANNEALING TEMPERATURE

O KLEIN
● MEER
X PRESENT WORK

ρ_8
$\times 10$
OHM M

FIGURE 63

ROOM TEMPERATURE MOBILITY AGAINST ANNEALING TEMPERATURE
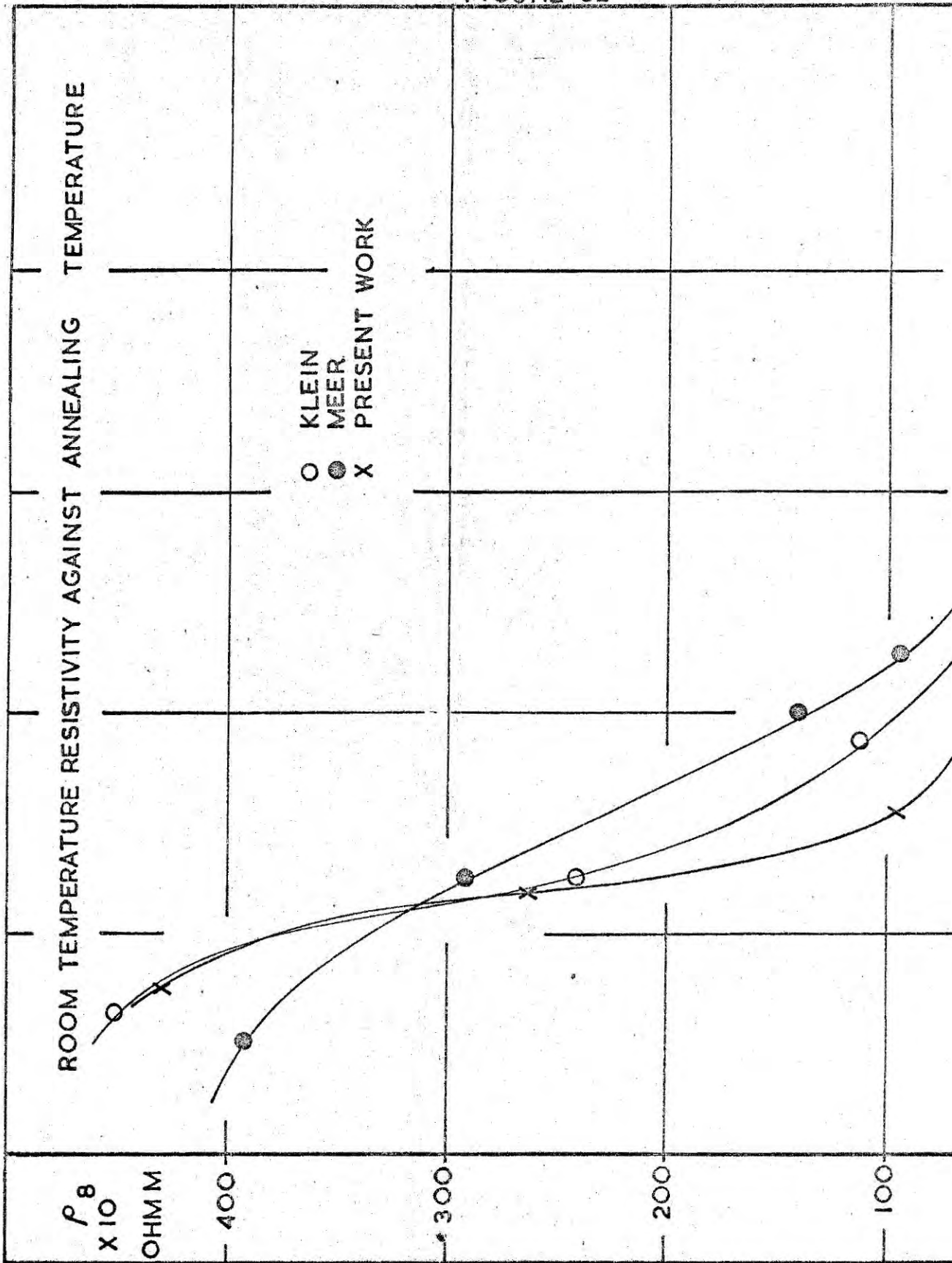
FIGURE 63
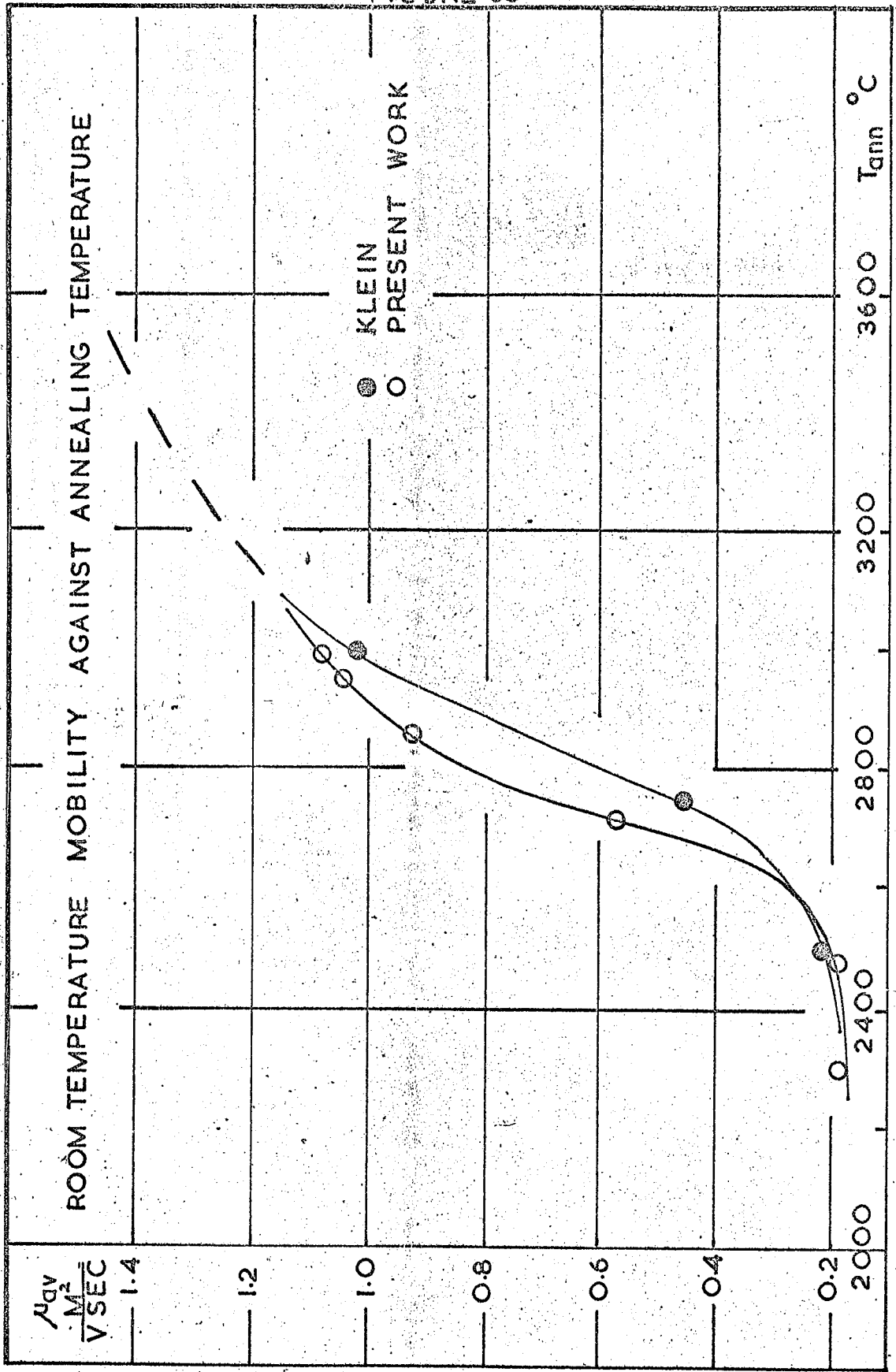
mobility is starting to increase, indicates that this is a critical temperature in the annealing process.

It will be seen that despite the inconstancy of the annealing temperature during the growth process the present results agree fairly well with the results of other workers. Thus it would seem that there is an alternative method of obtaining near single crystals of graphite without the need of a high temperature ($3600^{\circ}C$) tube furnace. If sufficient power is available (here it must be noted that at the end of the deposition, bar 22 was consuming 9.25 kilowatts of power), pyrolytic graphite deposits greater than 3 mms thick can be grown. At the end of the run the temperature of the innermost layers will be around $3200^{\circ}C$ with the temperature of the outer layer still at $2200^{\circ}C$. With this comparatively low outer temperature the bar may be held at this temperature without evaporating the material while the inner layers are being annealed.

A further point to arise from this work is the need to specify exactly where each sample comes from in the deposited bar, and the necessity of employing thin samples, since figures 59 and 60 show that the electronic properties of a sample 1 millimetre thick can vary by as much as half an order of magnitude. This throws some doubt on the results of Klein (1963) for unannealed samples.

CHAPTER IV

Correlation and Conclusions

3.4.1. Introduction

In previous chapters the theory of the transport coefficients in a material such as graphite was discussed. This theory was then simplified to give the coefficients for a specific orientation of graphite and two of the coefficients were calculated over a range of various parameters, on a computer.

The results of measurements of these and other coefficients in a specially designed cryostat were then compared with the theoretical results with the intention of deriving information about the band overlap and the position of the Fermi level. This however proved to be unsuccessful because of the large discrepancy between the two, indicating that the basic assumptions of the theory can not hold in these particular circumstances.

The two main assumptions were that the relaxation time was proportional to $E^{-1/2}$, where E is the energy of the carriers, that is, the scattering was by acoustic mode lattice vibrations, and that the energy surface is quadratic in k, the wave vector.

The failure of the latter of these assumptions was unlikely to cause the discrepancy found in the transverse

Nernst-Ettingshausen coefficient, but would undoubtedly explain the occurrence of the odd, linear, term in magnetic induction, found in the longitudinal Nernst-Ettingshausen coefficient. The difference between magnitudes of the theory and experiment in the latter coefficient was not considered to be significant.

For the former assumption, however, it was known that at temperatures below $80^{\circ}K$ a different type of scattering predominated, but it had been shown from the mobility that at temperatures above $200^{\circ}K$, the type of scattering assumed was predominant. However to give an indication of the behaviour of one of the thermomagnetic coefficients for an arbitrary scattering process an analysis was carried out on the transverse Nernst-Ettingshausen coefficient in the fully degenerate and non-degenerate regions of energy. This is given in appendix C with the results in appendix **D.** The correlation of this analysis with the experimental results is discussed in a later section of this chapter.

First of all, however, the design of the apparatus and the galvanomagnetic results will be discussed.

3.4.2. Design of Cryostat and Sample Holder

This cryostat and sample holder was designed to enable as many of the galvano- and thermo-magnetic coefficients as possible to be measured over as large a range of temperature

and magnetic induction as possible. This was achieved,
in that measurements were made at temperatures from 70°K
to 350°K over a range of magnetic induction of 0 to 1.0 W/m^2.
With the mobilities found in the samples this meant that the
maximum value of μB at 300° was 1.1, and at 80°K it was 4.5.
Thus at room temperature the range of μB covered was too
small to be in the high field limit, while at low temperatures
it was just large enough to indicate the high field tendencies
of the coefficients, without being actually in the high
induction limit. Since the magnetic induction was limited
only by the power available, the gap in the pole pieces being
as small as possible, and the temperature was limited by the
refrigerants available, it is concluded that the overall
design of the cryostat was successful. However the experi-
mental arrangement failed to make the measurements at
sufficient accuracy at low fields and at temperatures below
100°K, and did not cover a wide enough range of μB to give
conclusive results.

This can only be improved by improving the power
supply to the magnet which could also increase the range of
induction available, and by making the reference point for
the thermocouples the refrigerant liquid, in which case the
temperature differences would be of the same order as the
output from the thermocouples and the stray thermal e.m.f.'s.
due to the straining of the constantan wire in a severe

temperature gradient would be eliminated.

3.4.3. The Galvanomagnetic Coefficients

Two of these coefficients were employed as a measure of the degree of perfection of the samples and to determine the mobilities and densities of the carriers, according to an analysis developed by Soule (1958a). In this it was assumed that the density of electrons is exactly equal to the density of holes in order to simplify the calculations. This assumption has been shown to be true in single crystals of graphite by McClure (1958) by a more complex analysis than Soule's, but the results for the mobilities are up to 40 percent smaller than the results of Soule.

The analysis of both workers is given in sections 1.3.1. to 1.3.2., but only that of Soule is relevant to this work. The discrepancy between the two analyses is as yet unresolved, but it is obvious from section 3.2.4. that if the present results are scaled down to the same magnitude as McClure's there is extreme disagreement in the thermomagnetic measurements between the theory and experiment. The discrepancy mentioned is probably due to the fact that the fully degenerate approximation is only correct for $Eg < - 10kT$ as is shown in appendix D.

In addition to this discrepancy Soule's claim that the mobility was independent of the value of magnetic

induction was found not to hold for the present samples.

It was found that when μ_{av}, the average mobility, was plotted against $\mu_{av}^o B$ (μ_{av}^o, the average mobility in zero induction, being determined from a plot of μ_{av} against B) on a log-log scale a series of similar parallel curves were obtained (figure 10). Soule's results were also on parallel curves. In all of these curves μ_{av} became μ_{av}^o below $\mu B = 0.15$. This value of μB also turned out to be the theoretical value of the low field limit for the thermomagnetic effects. Figure 10 allows the low field mobilities to be determined without taking measurements at low fields. At low temperatures such measurements were difficult because the large values of mobilities made the condition $\mu B < 0.15$ difficult to fulful.

From the mobilities themselves an estimate of the average diameter of the crystallites was made, since it was known that at temperatures below about $20^o K$ the mobilities in pyrolytic graphite became independent of temperature. This effect was due to the crystallite boundaries acting as fixed scattering centres separated by a much smaller distance than the mean free path. (The boundaries can be regarded as rows of neutral impurities). To obtain these results it was necessary to extrapolate to low temperatures. Using the usual formula for the addition of mobilities the temperature independent term was removed, leaving a straight line if the extrapolation was correct. Since the results obtained

are in good agreement with preliminary measurements of the
same parameter employing the thermal conductivity, and are
of the same order of magnitude as the results obtained by
Klein (1961) from x-ray data on different samples, it is
concluded that the extrapolation was accurate, and that the
results give values for the average diameters of the
crystallites.

If there were only two contributions to the scattering
processes then the straight line remaining after the temperature
independent term had been removed should have been the single
crystal line. However it was found that the slopes of the
line depended on the perfection of the sample. This suggested
that the electron-phonon interaction was affected by the
large number of defects (crystallite boundaries) scattering
some of the phonons as well as the electrons, with the result
that the number of phonons available to scatter electrons
was decreased. This departure from the single crystal line
of mobility against temperature meant that the dependence of
the relaxation time on energy could have been affected.
However on a simple model the energy dependence comes from
the density of electron states, so that a variation in
the density of phonon states does not affect it. (Smith 1961,
page 146).

Comparison of the measured mobility with this line
indicates that the assumption that lattice scattering pre-

dominates in the theoretical work ought to be true for that region of temperature in which the scattering on crystallite boundaries is negligible, that is above 200°K.

The Hall coefficient in all samples except the very worst was found to be small and negative, in agreement with the results of other workers. The sign of the Hall coefficient remained negative at all inductions at which it was measured and down to the lowest temperatures attained indicating that the mobility of the electrons was always greater than that of the holes. The magnitude and temperature dependence of the densities of carriers was in good agreement with the results of other workers.

It can be concluded from these results that single crystal behaviour is expected above 200°K in samples 22B, 22C, 20A, 20B. Below this temperature scattering on the crystallite boundaries becomes important and at temperatures below about 80°K this type of scattering will predominate. This, however, is not confirmed by the thermomagnetic effect as will be shown in the next section.

Of the other two coefficients the Nernst effect was not measured and the Ettingshausen effect was not detected at any temperature up to the highest inductions obtained. It is concluded, therefore, that its coefficient is less than

10^{-4} $^{\circ}$K m^3/Joule.

3.4.4. The Thermomagnetic Coefficients

Of the four effects in the thermomagnetic category,
the thermal conductivity was not measured and the Righi-Leduc
effect was not detected at any temperature even with the
largest induction available. Its coefficient, therefore,
is less than 10 m^2/V sec.

The transverse and longitudinal Nernst-Ettingshausen
effects were measured over the range of temperatures and
magnetic induction mentioned in section 3.4.2. At room
temperatures the range of μB covered was too small to be in
the high induction limit for either effect, but the transverse
Nernst-Ettingshausen coefficient, Q, appeared to independent
of the magnetic induction. The longitudinal Nernst-Ettings-
hausen coefficient α(B) showed a linear term as well as the
expected quadratic term in B, the magnetic induction.

The magnitude of Q in the low induction limit was
found to be larger than predicted by the theory by a factor of
nearly two. On lowering the temperature, the predicted
temperature dependence was found, but the magnitude still
remained too large. At low temperatures the dependence of
Q on magnetic induction disagreed with the theory in that Q
was found to be almost independent of induction, up to values
of μB of 3.5, which is large enough to show any high induction

tendencies. Thus the experimental results do not agree

with the theory for purely acoustic mode lattice scattering.

Since the mobility indicated the presence of crystallite

boundary scattering an analysis was carried out for the case

of energy independent relaxation time. An energy independent

time was chosen since it was assumed that the crystallite

boundaries could be replaced by walls of neutral impurity

atoms which gave this type of energy dependence. This seems

a reasonable approximation since both the neutral impurities

and the crystallite boundaries are fixed in space. In

addition, the temperature independence of the mobility at

low temperatures agrees with the theory for neutral impurities.

In this analysis existing expressions for the non-

degenerate region were utilised. For the degenerate region,

the fully degenerate approximation of df_o/dE being a delta

function was employed. The two regions of induction $\mu B \ll 1$

and $\mu B \gg 1$ were considered by expanding the integrals I_{ikm}

of section 1.2.2. in terms of $(\mu B)^2$ and $(\mu B)^{-2}$ respectively.

It was found that the expressions for Q', the reduced

coefficient, in the high and low induction limits, were the

same in the non-degenerate region. This is also the case in

the fully degenerate region, but the factor $(5 + E_g^*)$ in the

former becomes $2\pi^2/E_g^*$ in the latter, there being a common

factor of $b/(1+b)$ to all expressions. Thus it is reasonable

to assume that at intermediate values of induction the

dependence of Q' on B will not change violently and Q' will be independent of induction.

In the partially degenerate region the results from the computer show a smooth transition from the fully degenerate to the non-degenerate region.   In addition to this, to a first approximation, the expression for the high induction value of Q' is independent of the scattering parameter. Thus it is reasonable to assume that a smooth curve can be drawn between the two curves as in appendix D.   If Q' does vary with B in this region there cannot be a large change since it is highly unlikely that there would be a violent fluctuation in the transition region.   Thus the temperature dependence of Q' will not be affected (within the accuracy of the experimental results, that is) but the magnitude of Q' has been increased by a factor which is roughly two bringing the theoretical value of this coefficient to within 10 percent of the experimental value.

The experimental variation with temperature of the longitudinal Nernst-Ettingshausen coefficient in zero magnetic induction (the Seebeck coefficient) was found to be similar to that found by Klein and to be explained down to $120^{\circ}K$ by the variation of the ratio of the mobilities.   Below this temperature some other effect must predominate.   Phonon drag effects are the most likely explanation of the increase in

the Seebeck coefficients below this temperature, but it is difficult to see how they arise in this effect and not in the Transverse Nernst-Ettingshausen effect. It may be that they arise in the latter at lower temperatures, for instance below $100^{o}K$ where the inaccuracy in the measurements masks any unusual variation with temperature. However the increase in the Seebeck effect could be caused by any one of several parameters since the theoretical results indicate that the Seebeck coefficient is very sensitive to a, b, and E_f, where these letters have their usual meanings. Further work is necessary before this problem can be resolved.

The variation of the longitudinal Nernst-Ettingshausen coefficient with magnetic induction $\alpha(B)$ was found to exhibit an 'Umkehr effect'. Although allowed by the symmetry of the crystal its presence has not been proved conclusively since a similar effect can arise due to misalignment of the probes. The theory used in the computer would not predict such an effect due to the oversimplification of the band structure. Comparison of the mean of the readings for the two directions of induction (the even part of the coefficient) indicated that the ratio of the densities of the carriers was one and that the Fermi level was near the centre of the band overlap.

No analysis for an energy independent relaxation time was carried out for this coefficient because of the complexity

of the equations.

3.4.5. Conclusions

In view of the analysis given in appendix C, the experimental evidence agrees fairly well with the theory, except that it is necessary to postulate that an energy independent relaxation time predominates at all temperatures. This can be explained by the scattering on the crystallite boundaries. However from the variation of the mobility with temperature it would appear that the scattering on crystallite boundaries only begins to predominate at temperatures below $100^{O}K$. At temperatures above this the range of μB covered by the present measurements is too small to give conclusive results, but the magnitude of the low field coefficient $Q^{'}$ indicates that the energy independent relaxation time appears to predominate. Thus the thermomagnetic coefficients do not agree with the galvanomagnetic coefficients in this respect.

Therefore it is concluded that although the agreement between the theory and experiment in the present work is good, even better agreement could be expected by following one of several courses.

The first, and most straightforward would be to extend the range of the present measurements down to liquid helium temperatures. At $4.2^{O}K$ crystallite boundary scattering

would predominate, the maximum value of μB expected (for sample 22B) would be of the order of 20, and the analysis of appendix C would hold, since E_g^* at $4.2^{\circ}K$ is 90 for the theoretical value of E_g.

The second and more difficult to attain, would be to make measurements on samples which have even nearer single crystal properties than the present. However in order to attain values of μB of 8 at room temperatures in even single crystal graphite, magnetic inductions of 5.0 W/m^2 are necessary. This makes experimental measurements more difficult, but the present theoretical results from the computer could be employed as the crystallite boundary scattering would be negligible.

The third and most complex course would be to write a computer programme which would utilize the exact energy equation (McClure 1964) which has recently been confirmed by magneto absorption measurements (Dresselhaus and Mavroides 1964) and to incorporate a term to take account of the mixed scattering parameters. This latter factor would involve assuming that the method of adding relaxation times by their reciprocals is valid for times which have different energy dependences. This fails when the two processes begin to interact. Such a programme would also predict the existence of the 'Umkehr effect' in the longitudinal Nernst-Ettingshausen coefficient, and could be used to calculate the

coefficients for all orientations.

APPENDIX A

Typical Results from the Computer

RATIO OF MOBILITIES =   1.00

ENERGY GAP =   .00000000

UB =   .00000000   .00000000

FERMI LEVEL = - 2.0000000

.900	-2.499	.7612	.5263	.0063
1.00	-2.503	.6199	.5000	-.0236
1.10	-2.493	.4921	.4762	-.0479

FERMI LEVEL = - 1.0000000

.900	-2.241	.4237	.5263	.0175
1.00	-2.247	.2944	.5000	-.0132
1.10	-2.239	.1774	.4762	-.0382

FERMI LEVEL = - .50000000

.900	-2.171	.2709	.5263	.0243
1.00	-2.177	.1449	.5000	-.0068
1.10	-2.170	.0309	.4762	-.0322

FERMI LEVEL = .00000000

.900	-2.146	.1249	.5263	.0315
1.00	-.2153	-.0000	.5000	-.0000
1.10	-2.147	-.1130	.4762	-.0258

FERMI LEVEL = .50000000

.900	-2.169	-.0.189	.5263	.0386
1.00	-2.177	-.1449	.5000	.0068
1.10	-2.172	-.2589	.4762	-.0193

FERMI LEVEL = 1.0000000

.900	-2.237	-.1651	.5263	.0452
1.00	-2.247	-.2944	.5000	.0132
1.10	-2.242	-.4113	.4762	-.0131

APPENDIX B

Computer Programme

THERMOMAGNETIC EFFECTS   J MILLS'

```
BEGIN    REAL ARRAY 1(1:3,0:2,1:2),  IT(1:3,0:2)'
         INTEGER L,J,K,N'
         REAL W,EF,EG,R,B,A'    SWITCH  SS:=L3'
         REAL PROCEDURE F(Y,P,Q,EF,W)'        REAL   T,P,Q,EF,W'
         BEGIN REAL TEMP'
                 TEMP:=EXP(Y-EF)'
                 F:=Y**P/(1+W**2*(Y**Q))/(1+TEMP)**2*TEMP'
         END'
         REAL PROCEDURE QUAD(P,Q,EF,W)'    REAL  P,Q,EF,W'
         BEGIN   INTEGER A'       REAL 11,12'
                 QUAD:=0'            12:=0'
                 FOR  A:=5,15 DO
                 BEGIN
     11:=5*(.249147*(F(A+.626665,P,Q.EF,W)+F(A-.626665,P,Q,EF,W))
        +.233492*(F(A+1.839160,P,Q,EF,W)+F(A-1.839160,P,Q,EF,W))
        +.203167*(F(A+2.936590,P,Q,EF,W)+F(A-2.936590,P,Q,EF,W))
        +.160078*(F(A+3.849515,P,Q,EF,W)+F(A-3.849515,P,Q,EF,W))
        +.106939*(F(A+4.520585,P,Q,EF,W)+F(A-4.520585,P,Q,EF,W))
        +.047175*(F(A+4.907805,P,Q,EF,W)+F(A-4.907805,P,Q,EF,W))'
     12:=11+12'
          END'
        QUAD:=12'
        END'

   L3R:= 0'
   READ EG,B'

BEGIN PRINT ££L2?? £ RATIO OF MOBILITIES = ?, SAMELINE, FREEPOINT
                                                          (3),B'

      PRINT ££L2? ENERGY GAP = ?, SAMELINE, EG'
FOR W:= 0,0.2,0.5,1.0,2.0  STEP 2 UNTIL 10.0 1 DO
     BEGIN
     PRINT ££L2?UB =?, SAMELINE, W,W/3*4/SQRT(3.1414)'
     FOR EF:= -.5*EF STEP -0.2*EG UNTIL -EG DO
     BEGIN
     PRINT ££L2?FERMI LEVEL =?, SAMELINE, EF'
     BEGIN REAL U, N'    SWITCH SS:=L1'
           K:=1'
           L1: N:= QUAD(1.5,0.EF,0)'
               U:= QUAD(1.0+R,0,EF,0)/N'
           FOR L:= 1,2 DO
           FOR J:= 0,1 DO
```

```
        1(L,J,K):= QUAD(1.5+L*(R-O.5)+J,2*(R-O.5)EF,W)/N/U**L'
        1F K=1 THEN BEGIN K:=2'
                          EF:=-EF-EG'
                          W:=W/B'
                          GOTO L1'
                    END'
          EF:=-EF-EG'
      W:=W*B'
      END'


            FOR A:=0.9 STEP 0.1 UNTIL 1.105 DO
BEGIN PRINT FREEPOINT (3),A'

      1T(1,0):=1(1,0,2)+A*B*1(1,0,1)'
      1T(2,0):=1(2,0,2)-A*B**2*1(2,0,1)'
      1T(1,1):=1(1,1,2)-A*B*1(1,1,1)+EG*1(1,0,2)'
      1T(2,1):=1(2,1,2)+A*B**2*1(2,1,1)+EG*(2,0,2)'

BEGIN REAL NUMER,TN,LTN'
      NUMER:=1T(1,0)**2+(W*1T(2,0))**2*9*3,1414/16'
        TN:=(1T(1,1)*1T(2,0)-1T(1,0)*1T(2,1))/NUMER'
       LTN:=(1T(1,1)*1T(1,0)+1T(2,1)*1T(2,0)*W**2*9*3.1414/16)/
                                                        NUMER

        PRINT ££S2??, SAMELINE  FREEPOINT(4),TN,££S2??,LTN,££S2??,
1T(1,0)/NUMER? ££S2??, 1T(2,0)/NUMER'
      END
      END OF B LOOP
      END OF A LOOP
END OF FERMI LOOP
END OF W LOOP'
READ N'    1F N GR O THEN GOTO L3'
END'
```

APPENDIX   C

Analysis of the transverse Nernst-Ettingshausen coefficient, Q^t, in (I) the non-degenerate, (II) the fully degenerate regions of energy in both the high induction and low induction limits for an arbitrary scattering coefficient.

In the following, various assumptions are made:-

a) $\tau = \tau_o \, x^{r-1/2}$ $\qquad\qquad\qquad\qquad$ $x = E/kT$

b) $n_1 = n_2 = n$, $\quad r_1 = r_2 = r$, and $E_{f1} = E_{f2} = -E_g/2$

The general expression for Q^t was derived in sections 1.2.2. to 1.4.5. and is

$$Q^t B = \frac{1}{Te} \left[\frac{I_{11}I_{20} - I_{10}I_{21}}{I_{10}^2 + I_{20}^2} \right] \qquad (i)$$

where the I_{ij} are as given in section 1.2.3.

$$I_{10} = I_{102} + I_{101} \qquad\qquad I_{20} = I_{202} - I_{201}$$

$$\qquad\qquad\qquad\qquad\qquad\qquad\qquad\qquad\qquad (ii)$$

$$I_{11} = I_{112} - I_{111} + E_g I_{102} \qquad I_{21} = I_{212} + I_{211} + E_g I_{202}$$

and

$$I_{ijm} = \frac{1}{3\pi^2} \, (eB)^{i-1} \int_o^\infty k^3 \left(\frac{\tau}{m}\right)^i E^j (1 + \omega^2\tau^2)^{-1} \frac{d_f}{dk} \, dk \quad \text{for the m th}$$
$$\text{carrier}$$

In the two induction limits either

$$\text{a)} \quad \mu B \ll 1$$

or

$$\text{b)} \quad \mu B \gg 1$$

In (a):-

$$I_{ij}^{o} = \frac{(\mu B)^{i-1} \; \frac{n\mu}{e} \; (kT)^{j} \int_{o}^{\infty} x^{(3/2+i(r-1/2)+j)} \frac{df_o}{dx} \, dx}{\int_{o}^{\infty} x^{3/2} \frac{df_o}{dx} \, dx} \left[\frac{\int_{o}^{\infty} x^{3/2} \frac{df_o}{dx} \, dx}{\int_{o}^{\infty} x^{r+1} \frac{df_o}{dx} \, dx} \right]^{i}$$

(iii)

in (b):-

$$I_{ij}^{\infty} = \frac{(\mu B)^{i-3} \; \frac{n\mu}{e} \; (kT)^{j} \int_{o}^{\infty} x^{(3/2+i(r-1/2)+j)} \frac{df_o}{dx} \, dx}{\int_{o}^{\infty} x^{3/2} \frac{df_o}{dx} \, dx} \left[\frac{\int_{o}^{\infty} x^{3/2} \frac{df_o}{dx} \, dx}{\int_{o}^{\infty} x^{r+1} \frac{df_o}{dx} \, dx} \right]^{i-2}$$

(iv)

for the m th carrier.

There are now two more approximations that can be made concerning the Fermi function $f_o = (1 + \exp(E^* - E_f^*))^{-1}$

$$\text{(I)} \quad E_f \ll 0 \qquad\qquad \text{(II)} \quad E_f \gg 0$$

In I, the non-degenerate region, expressions have been derived for both the high and the low induction limit.

E.g. Tsidil'kovski 1963

(a) $\quad Q'_o = \dfrac{3\sqrt{\pi}}{8} \dfrac{\Gamma(3/2+2r)}{\Gamma^2(2+r)} \dfrac{(1-2r)(b^3+1)-b(1+b)(7+6r+2Eg^*)}{(1+b)^2}$ $\qquad$ (v)

(b) $\quad Q'_\infty = -\dfrac{9\pi}{16} \dfrac{1}{\Gamma(3-r)\Gamma(2+r)} \left(\dfrac{b}{1+b}\right)(5+E_g^*)$ $\qquad$ (vi)

where $\quad \Gamma(m) = \displaystyle\int_0^\infty x^{m-1} e^{-x}\, dx$

for r = 0 these are the expressions employed to plot the non-degenerate lines which act as a check on the computer results in figure 17. The expressions can also be obtained by substituting equations (iii) and (iv) in (i) and (ii)

for r = 1/2 that is an energy independent relaxation time

$$Q'_o = -\dfrac{b}{1+b}\ (5+E_g^*) \qquad\qquad\qquad\text{(vii)}$$

$$Q'_\infty = -\dfrac{b}{1+b}\ (5+E_g^*) \qquad\qquad\qquad\text{(viii)}$$

Since these two expressions are identical it seems a reasonable assumption that at intermediate values of induction (i.e. μB of the order of 1) the same expression holds. Thus Q' is independent of magnetic induction.

In II, the fully degenerate region, the factor $\dfrac{df}{dE}$ in equations (iii) and (iv) is a delta function and the integrals can be replaced by an expression of the type

$$\int_0^\infty \emptyset\ (x)\ \frac{df}{dx}\ dx\ =\ \emptyset\ (\frac{E_f}{kT})\ +\ \frac{\pi^2}{6}\ \emptyset''(\frac{E_f}{kT})\ +\ \dots\dots$$

If only the first order terms in this expansion are included the Q' for all values of induction is zero. That is, in a metal there can be no effect, or at absolute zero there is no effect.

Thus the second order terms must be included.

For (a) $\mu B \ll 1$:-

$$I_{ijm}\ =\ \frac{n\mu}{e}\ (\mu B)^{i-1}\ (E_f)^j\ (1 + Aw(w-1))\ \text{for the m th carrier}$$

where $\quad A\ =\ \frac{\pi^2}{6}\ (\frac{E_f}{kT})^2\quad$ and $\quad w\ =\ \frac{3}{2} + i(r-\frac{1}{2}) + j$

and $\quad n\ =\ \frac{1}{3\pi^2}\ k^3(E_f)\quad$ and $\quad \mu\ =\ e\ (\frac{\tau}{m})\ (E_f)$

On substituting into equations (ii) and (i) and neglecting terms of the order of A^2

$$Q_o'\ =\ \frac{\pi^2}{3}\ \frac{1}{E_g^*}\ \left\{\frac{2r - 1 + 4b(r + 1) + b^2(2r - 1)}{(1 + b)}\right\} \qquad\text{(ix)}$$

For (b) $\mu B \gg 1$:-

$$I_{ijm} = \frac{n\mu}{e} (\mu B)^{i-3} (E_f)^j (1 + Aw(w-1) + (\mu B)^{-2} + \ldots$$

where A, w, n and μ are as before.

The term $(\mu B)^{-2}$ is included because the first order terms in μB in I_{20} is zero for $n_1 = n_2$.

From this expression it is found that

$$I_{11}I_{20} \ll I_{10}I_{21} \qquad I_{20}^2 \ll I_{10}^2$$

Therefore $Q_\infty^t B = - \frac{1}{Te} \frac{I_{21}}{I_{10}}$

and $$Q_\infty' = + 2\pi^2 \frac{1}{E_g^*} \frac{b}{1 + b} (1 - A(2-r)(1-r)) \qquad (x)$$

and to a first approximation Q_∞' is independent of the scattering parameter

for r = 0

$$Q_o' = - \frac{\pi^2}{3} \frac{1}{E_g^*} \frac{1-4b+b^2}{1+b} \left.\begin{array}{c} \\ \\ \\ \\ \\ \end{array}\right\} \qquad (xi)$$

$$Q_\infty' = + \frac{2\pi^2}{E_g^*} \frac{b}{(1+b)} \left[1 - \frac{4\pi^2}{3} \left(\frac{1}{E_g^*}\right)^2 \right] \quad E_g < 0 \qquad (xii)$$

for $E_g^* \rangle - 20$ the correction factor starts to depart from one

e.g. for $E_g^* = - 10$, $(1 - \frac{4\pi^2}{3} (\frac{1}{E_g^*})^2) = 0.87$

for $r = \frac{1}{2}$

$$Q_O^? = 2\pi^2 \frac{1}{E_g^*} \frac{b}{1+b} \qquad \text{(xiii)}$$

and

$$Q_\infty^? = 2\pi^2 \frac{1}{E_g^*} \frac{b}{1+b} \qquad \text{(xiv)}$$

Therefore to a first approximation $Q^?$ is independent of induction if the previous argument holds.

Note:- the correction factor for this value of the scattering parameter, the correction factor is smaller, being for $E_g^* = - 10$, 0.95.

It has now been shown that for an energy independent relaxation time, $Q^?$ and therefore Q is independent of induction in both the non-degenerate and fully degenerate regions of energy. It is thus reasonable to assume that Q will not depend on magnetic induction in the partially degenerate region, in particular the region $- 4 \langle E_g^* \langle 0$, which is the range of E_g^* for graphite down to 100^OK.

If figure 17 is now reproduced here, as in appendix D, these results may be plotted with an approximate curve joining the two regions.

Also shown in appendix D is the average value

of Q^2 in the samples 22B, 22C, 22D, 20B.

APPENDIX D
RESULTS OF APPENDIX C

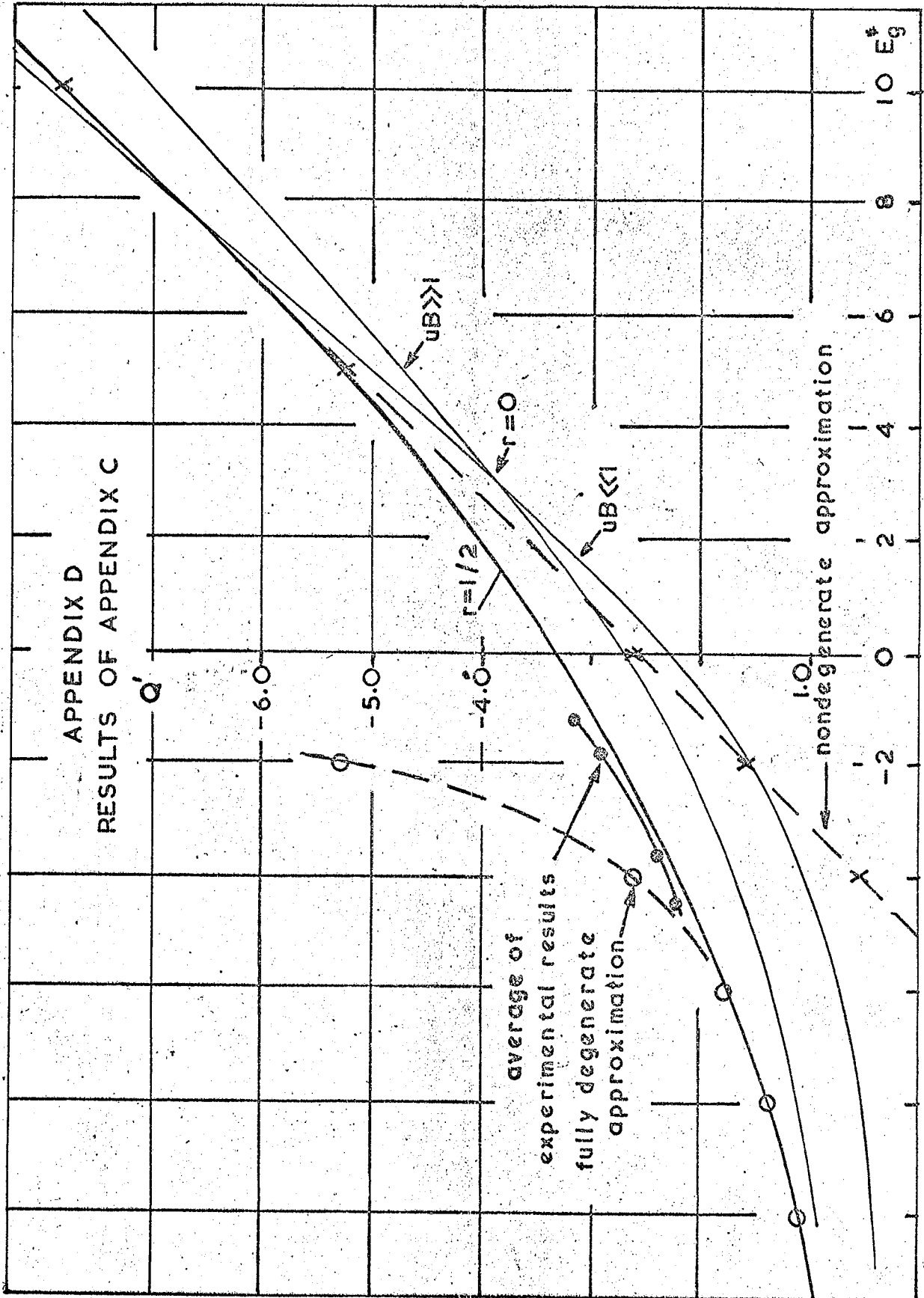## REFERENCES

Bernal, J.D., 1924. Proc. Roy. Soc. Vol. A106, p.749.

Blackman, L.C., Saunders, G.A., and Ubbelohde, A.R., 1961.
        Proc. Roy. Soc. Vol. A264, p.19.

Blackman, L.C. and Ubbelohde, A.R., 1962. Proc. Roy. Soc.
        Vol. A266, p.20.

Blatt, F.J., 1957, Solid State Physics. Vol. 4, p.199.

Bridgeman, P.W. 1924. Phys. Rev. Vol. 24, p.644.

Brown, A.R.G., and Watt, W., 1958. Industrial Carbon and
        Graphite, p.86.

Campbell, L.C., 1923, Galvano- and Thermo-magnetic Effects.
        Longmans Green, London.

Carter, J.L., 1953. Thesis. Cornell University.

Carter, J.L. and Krumhansl, J.A., 1953. J. Chem. Phys. Vol. 21,
        p.2238.

Corbato, F.J., 1956, Thesis M.I.T., and Proc. of Third Conf.
        on Carbon, 1959, p.173.

Coulson, C.A. 1947. Nature (London) Vol. 159, p.265.

Coulson C.A. and Taylor, R., 1952. Proc. Phys. Soc. (London)
        Vol. A65. p.815.

Debye P., and Scherrer, P. 1917. Phys. Z. Vol. 18, p.291.

Dresselhaus, M.A. and Mavroides, J.G. 1964. I.B.M. Res. Journal.
        Vol. 3, p.262.

Dutta, A.K. 1953. Phys. Rev. Vol. 90, p.187.

El Saden, M.R., 1962. J.A.P. Vol. 33, p.1800.

Ewald, P.P. 1914. Sitz. Munich Akad. Vol. 4, p.7.

Galt. J.K., Yager, W.A. and Dail H.W. 1956. Phys. Rev. Vol. 103
        p.1586.

Gottstein, G. 1914. Ann. d. Phys. Vol. 43. p.1079.

Haering, R.R., and Mrozowski, S. 1960. Progress in Semiconductors.
        Vol. 5. p.273.

Haering, R.R. and Wallace, P.R. 1957. J. Phys. Chem. Solids.
        Vol. 3. p.253.

Harman, T.C. and Honig, J.M. 1962-4.

	I	J.A.P. Vol. 33, p.3178
	II	J.A.P. Vol. 33, p.3188
	III	J.A.P. Vol. 34, p.189
	IV	J.A.P. Vol. 34, p.2215
with Tarmy, B.M.	V	J.A.P. Vol. 34, p.2225

Harvey, J., Clark, D. and Eastabrook, J.N., Royal Aircraft
        Establishment Technical Note. No. Met. Phys. 361,
        October 1962.

Hassel, O and Mark H., 1924. Z. Phys. Vol. 25, p.317.

Heurlinger, T. 1915. Ann. Phys. Vol. 84. p.48.
            1916. Phys. Z. Vol. 17. p.221.

Hull, A.W. 1917. Phys. Rev. Vol. 10. p.661.

Hurd, C.M., 1961. J. of Sci. Instr. Vol. 38. p.161.

Jan, J.P. 1957. Solid State Physics. Vol. 5., p.1.

Johnston, D.F., 1955. Proc. Roy. Soc. Vol. A227. p.349.
            1956. Roy. Soc. Vol. 237. p.48.

Kinchin, G.H., 1953. Proc. Roy. Soc. Vol. A217, p.9.

Klein, C.A. 1961. Raytheon Technical Report R58, February.
            1962. J.A.P. Vol. 33, p.3338.
            1963. Proc. 5th Conf. on Carbon. Vol. 2.
            1964. Raytheon Tech. Mem. T552, February.

Kohler, M. 1941. Ann. Phys. Vol. 40. p.601.

Lax, B. and Zeiger, H.J. 1957. Phys. Rev. Vol. 105, p.1466.

Lomer, W.M. 1955. Proc. Roy. Soc. Vol. A227, p.330.

McClure, J.W. 1956. Phys. Rev. 104, p.666.
            1957. Phys. Rev. Vol.108, p.612
            1958. Phys. Rev. Vol.112, p.115
            1959. Proc. 3rd Conf. on Carbon. p.179.
            1960. Phys. Rev. Vol. 119, p.606
with Yafet, Y. 1962. Proc. 5th Conf. on Carbon. Vol. 1. p.22.
            1963. See Smith, L.B., 1963.
            1964. See Soule, McClure and Smith, 1964.

Mazur, P. and Prigogine, I. 1951. J. Phys. and Rad. Vol. 12, p.616.

Mauguin, C. 1926. Bull. Soc. Franc. Min. Vol. 49. p.32.

Meer, J.T. 1963. Proc. 5th Conf. on Carbon. Vol.2. p.461.

Meixner, J. 1941. Ann. Phys. Vol. 40. p.165.

Moore, A.W., Ubbelohde, A.R. and Young, D.A. 1962. B.J.A.P. Vol. 13. p.393.

Morant, R.A. 1964. Private Communication.

Nozieres, P. 1958. Phys. Rev. Vol. 109. p.1510.

Primak, W. and Fuchs, L.H. 1954. Phys. Rev. Vol. 95. p.22.

Putley, E.H. 1960. The Hall Effect and Related Phenomena. Butterworth.

Saunders, G.A. 1964. App. Phys. Letters. Vol. 4. p.138.

Shoenberg, D. 1952. Phil. Trans. Roy. Soc. (London) Vol. 245. p.1.

Slonczewski, J.C. 1955. Thesis, Rutgers University Mic. 56-2314 University Microfilms, Ann. Arbor, Michigan.

Slonczewski, J.C. and Weiss, P.R. 1958. Phys. Rev. Vol. 109. p.272.

Smirnov, I.A., 1964. Private Communication

Smith R.A. 1961. Semiconductors. Cambridge University Press.

Smith, L.B. and McClure, J.W. 1963. Proc. 5th Conf. on Carbon. Vol. 2. p.3.

Smith, A.W. and Rasor, N.S. 1956. Phys. Rev. Vol. 104, p.885.

Soule, D.E. 1958a. Phys. Rev. Vol. 112, p.698.
             b. Phys. Rev. Vol. 112, p.708.

Soule, D.E. and McClure, J.W. 1959. J. of Phys. Chem. Solids, Vol. 8, p.29.

Soule, D.E. McClure, J.W., and Smith, L.B., 1964. Phys. Rev. Vol. 134,A, p.453.

Taft, E. and Apker, L. 1955. Phys. Rev. Vol. 99, p.1831.

Trezbiatowski, W. 1936. Chem Abstract. Vol. 31. p.4177.

Tsidil'kovski, I.M. 1963. Thermomagnetic Effects. Infosearch.

Ubbelohde, A.R. 1962. See Blackman and Ubbelohde. 1962.

Ubbelohde, A.R., and Orr, J., 1957. Nature (London) Vol. 179, p.193.

Ure, R.W., 1963. Proc. I.E.E.E. Vol. 51, p.699.

Wagoner, G. 1960. Phys. Rev. Vol. 118, p.647.

Wallace, P.R. 1947. Phys. Rev. Vol. 71. p.622.

Wilson A.H., 1936, 1953, The Theory of Metals, 1st and 2nd Editions. Cambridge University Press.

Wolfe, G.E. and Smith, R. 1963. Bull. Am. Phys. Soc. Vol. 8, p.210.

Wright, D.A. 1962. B.J.A.P. Vol. 13, p.583.

Ziman, J., 1960. Electrons and Phonons. Cambridge University Press.